Experimental research on hydrodynamic failure of river bridges on spread footings

MASTER THESIS

Civil Engineering
Hydraulic Engineering / Structural Engineering

June 2018

Kevin Oudenbroek
Studentnumber 4158385

TU Delft

LIST OF SYMBOLS

Symbol	Description	Unit
A	Flow area obstructed by the deck	[m^2]
A_{deb}	Flow area obstructed by debris	[m^2]
W	Width of the bridge deck	[m]
B	Width of the flume	[m]
B_a	Average width of the base of the pier	[m]
C_D	Drag coefficient	[-]
C_F	Force coefficient	[-]
C_L	Lift coefficient	[-]
C_M	Moment coefficient	[-]
d_{ss}	Defined as max{d_{wgs};s_f}	[m]
d_{wgs}	Defined as $h_u - h_b$	[m]
F_B	Buoyancy force	[N]
F_D	Drag force	[N]
F_H	Horizontal force measured by load cell	[N]
F_L	Lift force	[N]
Fr	Froude number of a flow, defined as $U / \sqrt{(gh_u)}$	[-]
Fr_S	'Deck' Froude number	[-]
F_V	Vertical force measured by load cell	[N]
F_Z	Gravitational force	[N]
g	Gravitational acceleration (9.81 m/s^2)	[m/s^2]
H	Height of bridge deck, equal to s_f or s_m, depending on the presence of railings	[m]
h^*	Inundation ratio, defined as $(h_u - h_b) / s$	[-]
h_b	Distance from the riverbed to the bottom of the bridge superstructure	[m]
h_u	Flow depth	[m]
L	Length of the bridge deck	[m]
M	Moment measured by load cell	[Nm]
M_{cg}	Moment acting on a component around its center of gravity	[Nm]
μ	Friction factor	[-]
h_{cg}	Vertical distance from point of rotation to center of gravity	[m]
L_{cg}	Horizontal distance from point of rotation to center of gravity	[m]
P_r	Proximity ratio, defined as $y_{gs} / \max\{d_{wgs};s_m\}$	[-]
R_{hor}	Horizontal restoring force	[N]
R_{over}	Restoring moment	[Nm]
R_{vert}	Vertical restoring force	[N]
s	Bridge deck height	[m]
s_f	Height of the bridge deck, including any railings	[m]
S_{hor}	Soliciting horizontal force	[N]
s_m	Height of the bride deck, excluding railings	[m]
S_{over}	Overturning moment	[Nm]
S_R	Relative submergence (identical to h*)	[-]

S_{vert}	Soliciting vertical force	[N]
U	Flow velocity	[m/s]
U_u	Flow velocity at an upstream reference point	[m/s]
$W_{<object>}$	Weight of <object> (by gravity)	[N]
y_{gs}	Equal to h_b	[m]
Z_{hor}	Resistance against horizontal movement, expressed in N	[N]
Z_{over}	Resistance against rotational movement, expressed in Nm	[Nm]
Z_{vert}	Resistance against vertical movement, expressed in N	[N]
ρ	Fresh water density (1000 kg/m^3)	[kg/m^3]
$\rho_{<material>}$	Density of <material>	[kg/m^3]

Indices used:

Symbol	Description
over	Refers to rotational movement / moments
hor	Refers to horizontal movement / forces
vert	Refers to vertical movements / forces
+	Refers to 'with debris'
-	Refers to 'without debris'
D	Refers to drag (force)
L	Refers to lift (force)
B	Refers to buoyancy (force)
Z	Refers to gravitational (force)
p	Refers to pier
d	Refers to deck
t	Refers to pier-deck system ('total')

LIST OF FIGURES

ACKNOWLEDGEMENTS

The author wishes to thank first and foremost dr. ir. Jeremy Bricker, who in his role as daily supervisor and part of the thesis assessment committee, provided guidance throughout the entire process of the research. Also the other members of the assessment committee, dr. ir. Cor van der Veen and prof. dr. ir. Bas Jonkman, are thanked for their input and feedback during and outside of committee meetings.

Furthermore, the author greatly appreciates the efforts of prof. Shuji Moriguchi of Tohoku University and the International Research Institute of Disaster Science in providing data and properties of the bridge.

Also mr. David Hoogewerff and his coworkers of the Quartel Modelbouw hobby shop were invaluable for their help in fabrication of an accurate scale model of the bridge.

Lastly, many thanks are also owed to the TU Delft Fluid Mechanics laboratory and its staff for being able to use one of their flumes as well as all the other necessary equipment to perform experiments.

ABSTRACT

Collapse of partially or fully submerged river bridges as a result of river floods is investigated. To this end, post-failure analysis of a bridge in Japan's Iwate Prefecture that collapsed in 2013 is conducted. Failure of this particular bridge is atypical because piers have also toppled over, which can be attributed to the spread footing foundation not anchored to the bedrock.

Two hypotheses are formed regarding the failure mode of this bridge. One assumes that initially the deck was dislodged and the piers subsequently toppled over, while the other follows the scenario of simultaneous failure of deck and pier. In order to predict which failure mode is governing, estimates of hydrodynamic forces based on design standards and previous research are formulated in conjunction with an analysis of the capacity of a potential bearing type.

Experiments in a flume are performed at a 1:37 scale to simulate steady-state hydrodynamic forces on the bridge. The flow depth and Froude number of the flow are varied across a wide range. Simulated debris is also lodged against the bridge model during some experiments. Observations on under which conditions a free-standing bridge model will or will not fail are carried out. These conditions are then replicated while the bridge model is connected to a load cell to determine the forces associated with failure.

Results show that the resistance against horizontal movement of a bridge deck actually increases as Froude number increases, as negative lift forces dominate over drag forces. Standalone piers always have sufficient resistance against overturning as long as no debris is present. Addition of simulated debris against the pier breaks down its streamlined shape and can cause toppling over of a pier.

Failure of the bridge as a whole (intact deck-pier connection) is not observed under any conditions during the experiments and this hypothesis is discarded. Subsequent failure of deck and pier only happens when simulated debris accumulations are introduced into the experiment. Deck displacement occurs at inundation ratios greater than 2.0 at moderate Froude numbers ($0.14 \leq Fr \leq 0.32$). Pier failure occurs at $Fr \geq 0.34$ when the flow depth exceeds the height of the pier.

Possible countermeasures and improvements that may be incorporated into the design of bridges so that they may be more resilient to collapse during a flood in the future are suggested.

Keywords: bridge deck, pier, drag, lift, moment, river, flood, spread footing, experiments, flume.

1 INTRODUCTION

1.1 MOTIVE FOR THIS RESEARCH

The effects of damage to infrastructure caused by extreme weather events can be severe. Besides the obvious economic losses, it becomes much harder to aid struck regions when the routes leading towards the area can no longer be used. For bridges crossing rivers, floods can be particularly problematic. Especially flash floods, induced by heavy and localized rainfall and often carrying man-made and natural debris, are a threat to river bridges. It is not uncommon for bridges to partially or completely collapse, after the bridge deck is completely submerged by the fast-flowing river, unable to withstand the forces associated with a flood.

In the past many researchers have taken interest in the topic of bridge failure by river floods [Denson (1982), Jempson (2000), Malavasi and Guadagnini (2003), Kerenyi et al. (2009)]. Most of the carried out research has been focused on determining the forces on the superstructure (i.e. the deck) of a bridge when it is attacked by a flow. Scour around bridge piers founded in/on soft soils has also been a widely researched topic [(Melville (1992, 1996), Jones (1984, 1992)], as well as the formation of debris mats piling up against bridges [Parola (2000)], along with its consequences. Knowledge is lacking for bridges in mountainous regions, where the foundations of bridges are typically shallow and directly on top of the easily accessible bedrock.

An example of such a river bridge in a mountainous region that was destroyed by a flood is shown in Figure 1. This is the 30 meter long Yabitsu Bridge and was part of prefectural road 162 in the Iwate Prefecture in Japan, crossing the Yabechi River. It suffered collapse during the floods that occurred as a result of torrential rainfall on the 9th and 10th of August, 2013.

Figure 1: Photo of destroyed bridge crossing Yabechi River (taken by J.D. Bricker, 2013)

This bridge consisted of two piers and three deck segments, all of which were found more or less in one piece some distance downstream of the location, as can be seen from Figure 2 to Figure 5. The piers each had a spread footing foundation, which was resting on the bedrock inside a shallow recess made into the riverbed.

Figure 2: Panoramic photo of the destroyed bridge (taken by J.D. Bricker, 2013)

Figure 3: Photo of one of the dislodged deck segments and debris (taken by J.D. Bricker, 2013)

Figure 4: Photo of the collapsed southern pier (taken by J.D. Bricker, 2013)

Figure 5: Photo of the collapsed northern pier (taken by J.D. Bricker, 2013)

In most known cases of bridge collapse due to hydrodynamic forces (this includes for example collapse due to a tsunami), only the deck has been destroyed or dislodged, see for example Figure 6. And in cases where failure of the pier also occurred, this could be attributed to scour around the base of the pier, causing instability of the foundation. The collapse of this bridge is therefore atypical because the piers also appear to have toppled over, while the ground in the area consists of bedrock, which is assumed to have very low erodibility and thus mostly insusceptible to scour.

Figure 6: collapse of Fisher Road Bridge over Blanco River at Wimberley, Texas, USA in May 2015 (taken by C. Bailey)

1.2 PROBLEM STATEMENT

During river floods the construction of a river bridge should not fail, for obvious economic reasons as well as for continued accessibility of a disaster-struck region. At worst, the bridge is only temporarily unusable due to the current conditions, but remains structurally intact to be available for use once water levels in the river drop. Designers should take hydrodynamic loads of a flood with a certain average return interval (ARI) on the bridge into account, depending on the expected lifetime of the bridge and the desired reliability. Unfortunately, the hydraulic conditions such as flow velocity, flow depth and debris load are hard to predict accurately. Their associated loads are difficult to quantify due to vastly different geometries of bridge superstructures and piers.

1.3 RESEARCH GOAL

Much like other post-failure research done on civil engineering structures, the goal of this research was to understand the failure mechanism that occurred, and ultimately propose measures to prevent similar failures from happening in the future. The main question of this research is therefore stated as:

What could cause river bridges on spread footings to fail during river floods and which prevention measures can be undertaken?

1.4 RESEARCH METHOD

Before anything can be said about prevention, it is necessary to know what caused failure in the first place. This entails determining the failure mechanism(s) that contributed to the destruction of the bridge and the forces associated with this/these failure mechanism(s). The following sub-questions are formulated:

- What are the forces acting on the scale model, and how do these change as a function of
  - flow velocity
  - water depth
  - amount and orientation of debris?
- Which failure mechanism(s) play a role in the failure of the bridge under investigation?
- What kind of adaptations can be applied to similar bridges that can serve as a countermeasure to failure by river floods?

Scaled experiments in a steady-current flume were carried out in an attempt to answer these questions.

2 LITERATURE REVIEW

2.1 HYDRODYNAMIC FORCES ON BRIDGE STRUCTURES

This section explores research carried out in the last 20 years.

2.1.1 MALAVASI & GUADAGNINI (2003) (1)

Malavasi and Guadagnini (2003) studied the hydrodynamic loading on river bridges that are either completely or partially submerged by a flow. Due to the presence of a free surface and a bottom boundary, drag and lift forces on superstructures are different from what would be expected from an identical geometry in unbounded flow. After performing a dimensional analysis of the problem, they found that, under the assumption of a time-averaged steady-state mean flow, similar geometries and some other simplifications, the force coefficient can be expressed as a function of the inundation ratio and the 'deck'-Froude number only:

$$C_F = f\left(\frac{h_u - h_b}{s}, Fr_S\right) = f(h^*, Fr_S) \qquad \text{Equation 2-1}$$

where

C_F	Force coefficient, can indicate both a drag coefficient C_D as well as a lift coefficient C_L	[-]
h_u	Height of the water column	[m]
h_b	Distance from ground surface to bottom of the bridge	[m]
s	Height of the bridge deck	[m]
Fr_S	'Deck'-Froude number, defined as: $Fr_S = U_u/\sqrt{gs}$	[-]
U_u	Flow velocity at an upstream reference point	[m/s]

The experiments were carried out using two pairs of dynamometers attached to the scale model of the bridge deck, one pair to measure horizontal forces and the other pair to measure vertical forces. The scale model was a simple rectangular box with a length over thickness ratio of 3. The data was recorded over a longer period and then time-averaged. The measurements of the dynamometers were used to find the coefficients according to:

$$F_D = C_D * \rho s \frac{U_u^2}{2} \quad ; \quad F_L = C_L * \rho s \frac{U_u^2}{2} \qquad \text{Equation 2-2}$$

where

F_D; F_L	Total measured horizontal force; total measured vertical force (per unit width)	[N/m]
C_D; C_L	Drag coefficient; lift coefficient	[-]
ρ	Density of water	[kg/m^3]

The experiments were carried out at different 'deck'-Froude numbers. The results for the drag coefficient show a peak value of C_D = 3.4 located around h^* = 1.2, shifting to higher values of the inundation ratio for higher values of Fr_S. For the highest values of the inundation ratio the drag coefficient tends to its value for unbounded flow.

The lift coefficient C_L was found to be negative in all experiments (resultant force directed downward). The maximum lift coefficient (according to Equation 2-2) was found to be approximately -10.0 at $h^* > 1.0$, independent of Fr.

2.1.2 JEMPSON (2000) (2)

Jempson (2000) investigated the effect of the Froude number (*Fr*), degree of submergence (S_R, similar to the inundation ratio) and proximity of the superstructure to the bed (P_r), on the forces and moments acting on the bridge piers and superstructures. This was done using different superstructures and pier types. Scale models of a prestressed concrete bridge with 4 AASHTO Type IV I-beams, a bridge with steel plate girders, a spread box beam bridge and adjacent box beam bridge, a steel truss bridge and a box girder bridge, as well as scale models of a pier with two columns, a single elongated column and a truss-type column were used for this purpose. The forces were measured with two different methods, one directly using dynamometers and the other indirectly using pressure sensors. The effects of debris on the forces were also subject of investigation. Scale models of a flat plate debris mat, a rough triangular wedge debris mat and a semi-cone debris mat were used.

The extensive and elaborate research, consisting of about 500 different tests, resulted in recommendations for a revised design methodology. Many different design charts such as the one shown in Figure 7, were developed for the coefficients C_D, C_L and C_M, showing their dependencies on *Fr*, S_R and P_r. This was done for the different types of superstructures and piers, making a distinction between situations with or without debris. The superelevation (inclination) of a standardized deck type was also considered and implemented in the design charts.

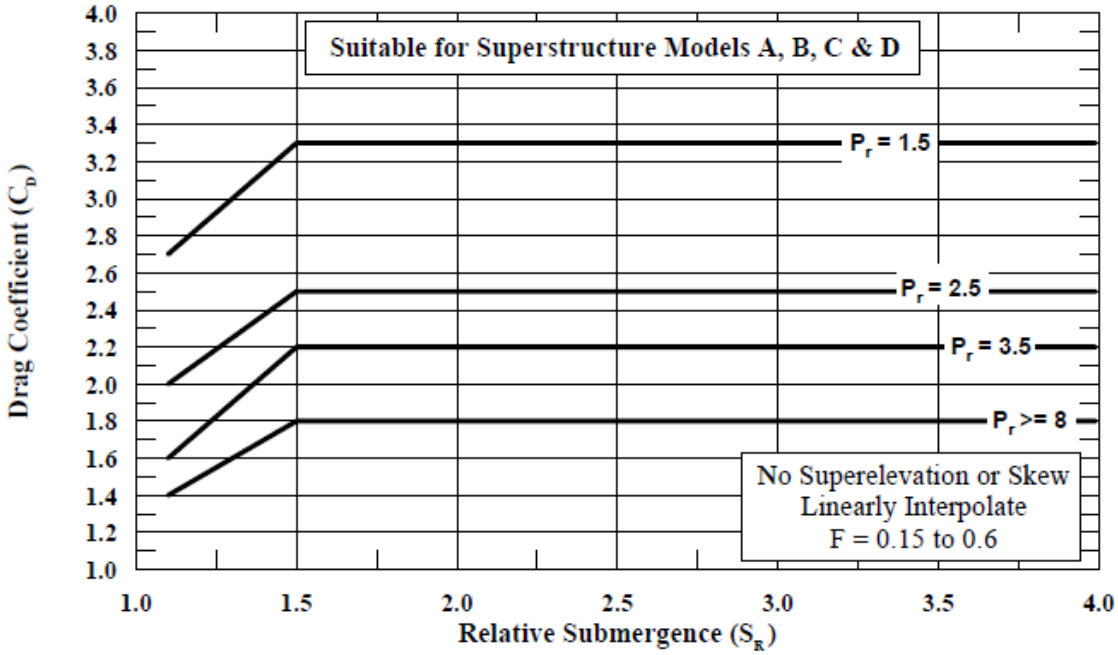

Figure 7: design chart for drag coefficient of a bridge deck (Jempson, 2000). Superstructure C (spread box beam bridge) resembles the geometry of the Yabitsu Bridge the most.

2.1.3 BRICKER ET AL. (2012) (3)

Bricker et al. (2012) found, using numerical modelling, that vortex-shedding phenomena can cause the lift force and overturning moment on bridge decks exposed to a steady flow to exhibit a periodic pattern. At some point these lift forces and overturning moments will peak for a short period of time, possibly causing incipient rotation of the bridge deck, this is shown in Figure 8.

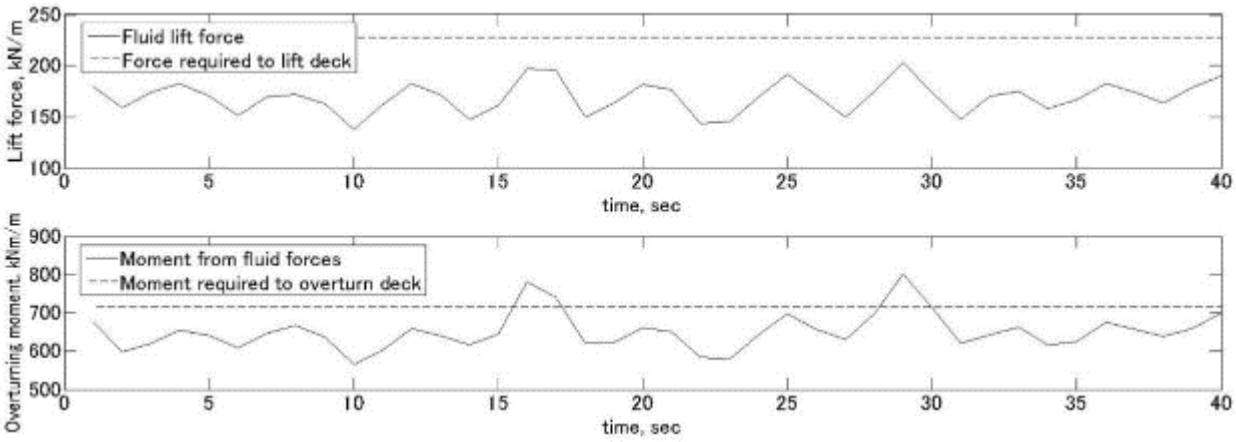

Figure 8: numerical simulation of overturning moment and lift force on a bridge deck, showing a periodic pattern caused by vortex shedding (Bricker, 2012)

It was also found that the behavior of the free surface downstream of the bridge deck, such as the presence of a hydraulic jump, can have a significant effect on the lift force and overturning moment. It was also concluded that deck superelevation (inclination of the bridge deck surface) had a profound effect on the mean value of the overturning moments and lift forces.

2.1.4 BRICKER ET AL. (2014) (4)

Bricker et al. (2014) investigated failure of a bridge deck due to tsunami. Since the bridge deck was completely submerged at the time of failure and the flow over the bridge deck was relatively steady, it is possible to apply the results of this case study to bridge deck failure by river flow.

Using a numerical model validated by comparison with experiments performed by Kerenyi et al. (2009), several different scenarios were analyzed to investigate the effect of deck inclination (superelevation), presence of nearby structures and sediment entrapped in the flow.

It was found that drag experienced by the bridge deck approached a constant value as the bridge deck became fully submerged, corresponding to $C_D = 1.7$ at $h^* \geq 2.0$. The net vertical force was a combination of negative lift force due to flow acceleration under the deck and upward force due to buoyancy and air trapped between bridge girders. As the deck became more submerged ($h^* > 1.0$), the negative lift decreased since the difference between flow accelerations below and above the deck became smaller, while the buoyancy force remained constant. This resulted in a net increase of upward force. However, this vertical force would not be sufficient to overcome gravity and lift the deck off of its piers. Instead, the deck rotated off of its piers because the overturning moment, caused by the combination of high drag and (lack of) negative lift, would exceed the critical value at some times during maximum recorded submergence.

According to the performed simulations, this critical value wouldn't have been (as easily) exceeded if the deck would have been level instead of inclined. The close proximity of a seawall at the downstream side of the bridge

deck also aided in the bridge's collapse, because this structure acted as a constriction in the flow, causing smaller flow accelerations under the bridge deck compared to the case where a seawall wouldn't be present, leading to less negative lift force on the bridge deck.

2.1.5 KOSA (2014) (5)

Kosa (2014) investigated the relationship between the damage sustained by 37 different bridges after the Great East Japan Earthquake and the following tsunami, and their resistance to lateral force. The latter was quantified using a beta ratio defined as follows:

$$\beta = \frac{R_{1,2}}{F_D} \quad \text{with} \quad F_D = \frac{1}{2}\rho C_D A U^2 \; ; \; R_1 = \mu W_{deck} \; ; \; R_2 = \mu(W_{deck} - F_B) \qquad \text{Equation 2-3}$$

where

β	Ratio of girder lateral resistance to tsunami lateral force		[-]
R_1	Frictional resistance in case a bridge girder isn't completely submerged		[N]
R_2	Frictional resistance in case a bridge girder is completely submerged		[N]
ρ	Fresh water density (1000 kg/m^3)		[kg/m^3]
C_D	Drag coefficient defined is this research as:		[-]
	2.1 – 0.1(s/B)	1 < s/B < 8	
	1.3	8 < s/B	
s	Height of the bridge deck		[m]
B	Width of the bridge deck		[m]
A	Flow area obstructed by the deck		[m^2]
μ	Friction coefficient between deck and pier (0.6 in Kosa's research)		[-]
W_{deck}	Weight of the bridge deck		[N]
F_B	Buoyancy force on the bridge deck		[N]

In general, bridges with a high β-ratio have a slender cross-section, with the height much smaller than the width. Bridges with a low β-ratio can be described as bulky and the height of the girders is relatively large. The analysis showed that bridge decks with a value of $\beta > 1.5$ only suffered minor damage while bridge decks with $\beta < 0.6$ were separated from their piers and completely swept away by the flow. In an attempt to explain why some bridge decks with a β-value larger than 1.0 were swept away, Kosa noted that this was only the case for bridges whose girders where T-shaped. The simple formula for C_D was deemed inappropriate for these type of girders, since vortices that can occur around the web of a T-shaped girder exposed to a lateral flow can increase the Cd-value. This would subsequently lead to a lower β-value. An explanation was also provided for the fact that some bridge decks with $\beta < 1.0$ suffered only minor damage: a constant value of the flow velocity ($U = 6.0$ m/s) was applied in the analysis, but real values might have been different in different areas.

Two bridges (Hachiman Bridge which survived the tsunami and Utatsu Bridge which collapsed during the tsunami) were investigated further. Using video evidence and numerical modelling, forces acting on both bridge decks in two possible scenarios were estimated. The first scenario was impact of a tsunami wave against one side of the bridge deck, while the other side was not submerged. The second scenario involved a completely submerged bridge deck exposed to a steady flow. Kosa concluded that the Hachiman Bridge did indeed have sufficient resistance against the impact forces of both scenarios, as indicated by its β-values of 2.76 (scenario 1) and 5.51 (scenario 2). The Utatsu Bridge however, was found to have a β-value of 0.88 for scenario 2 according to video analysis and 1.12 according to numerical simulation, backing up the fact that this bridge failed during the tsunami.

2.1.6 Federal Highway Administration (2009) (6)

In 2009, the U.S. Department of Transportation's Federal Highway Administration (FHWA) issued a report titled "Hydrodynamic Forces on Inundated Bridge Decks". The effects of varying flows on different bridge deck cross-sections were studied with physical experiments and numerical modelling using Computational Fluid Dynamics (CFD) software. The results of the physical experiments and numerical modelling were then compared to each other. The results of this research came in the form of graphs depicting the drag coefficient C_D, lift coefficient C_L and moment coefficient C_M as a function of the inundation ratio h^*. The inundation ratio h^* was defined as follows:

$$h^* = \frac{h_u - h_b}{s} \qquad \text{Equation 2-4}$$

where

h_u	Height of the water column	[m]
h_b	Distance from ground surface to bottom of the bridge	[m]
s	Height of the bridge deck	[m]

The research used the expression given in Equation 2-5 for calculation of drag coefficients from measured drag forces. Equation 2-6 was used for calculation of lift forces and Equation 2-7 for moments.

$$F_D = \frac{1}{2} C_D \rho U^2 s \quad \text{if} \quad h^* \geq 1$$
$$F_D = \frac{1}{2} C_D \rho U^2 h^* s \quad \text{if} \quad h^* < 1 \qquad \text{Equation 2-5}$$

where

F_D	Drag force (positive downstream) per unit length	[N/m]
C_D	Drag coefficient	[-]

$$F_L = \frac{1}{2} C_L \rho U^2 W \qquad \text{Equation 2-6}$$

where

F_L	Lift force (positive upwards) per unit length	[N/m]
C_L	Lift coefficient	[-]
W	Width of the bridge deck	[m]

$$M_{cg} = \frac{1}{2} C_M \rho U^2 W^2 \qquad \text{Equation 2-7}$$

where

M_{cg}	Moment around the center of gravity per unit length (positive counterclockwise)	[Nm/m]
C_M	Moment coefficient	[-]

Three different cross-sections of bridges were used in the research; a six-girder bridge deck representing a typical U.S. highway bridge deck shape, a three-girder bridge deck with the same width but a larger frontal area and a streamlined bridge deck. The physical experiments were also carried out at different values of the Froude number Fr.

The physical experiments for the six-girder bridge deck showed a minimum of the drag coefficient C_D at values of h^* ranging from 0.5 to 0.8, with a maximum of about 2.0 as $h^* \geq 1.5$. As the Froude number increased, so did the drag coefficient. Only one of the three numerical models used (the Fluent k-ε model) was able to reproduce these results fairly well.

The lift coefficient C_L remained negative for all inundation ratios, with a minimum between $h^* = 0.8$ to 1.2, according to the experimental results. This indicates a net force pulling down on the structure at all times. None of the numerical models used corresponded well to the results of the physical experiments.

The moment coefficient C_M showed a peak around a value of h^* equal to 0.8, indicating a tendency of the upstream part of the deck to move upwards and the downstream part downwards. As the values of h^* increased, the value of C_M approached a constant value, which was smaller as the Froude number increased, transitioning from positive to negative values of C_M around $Fr = 0.3$. The CFD results did not seem to be able to reproduce the peak value of C_M.

2.1.7 AUSTRALIAN BRIDGE DESIGN STANDARDS AS5100 (2004) (7)

The Australian bridge design codes provide design values for hydrodynamic loading on bridge superstructures. According to the codes, forces are a function not only of the relative submergence (synonymous to inundation ratio) but also of the so-called proximity ratio, which expresses how high the deck is above the riverbed. The drag force should be calculated according to Equation 2-8

$$F_{ds} = \frac{1}{2}\rho C_D U_u^2 A_s \qquad \text{Equation 2-8}$$

where

F_{ds}	Drag force on the bridge deck	
C_D	Is obtained from Figure 9:	[-]

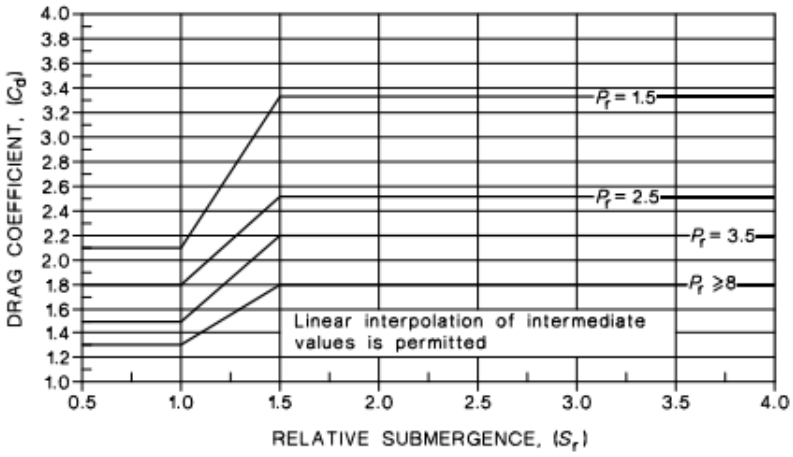

Figure 9: Drag coefficient on bridge superstructure (7)

U_u	Mean flow velocity at the level of debris	[m/s]
A_s	wetted area of the superstructure, including any railings or parapets, projected on a plane normal to the water flow	[m^2]
S_r	Relative submergence = d_{wgs} / d_{sp}, see Figure 10	[-]

P_r Proximity ratio = y_{gs} / d_{ss}, see Figure 10 [-]

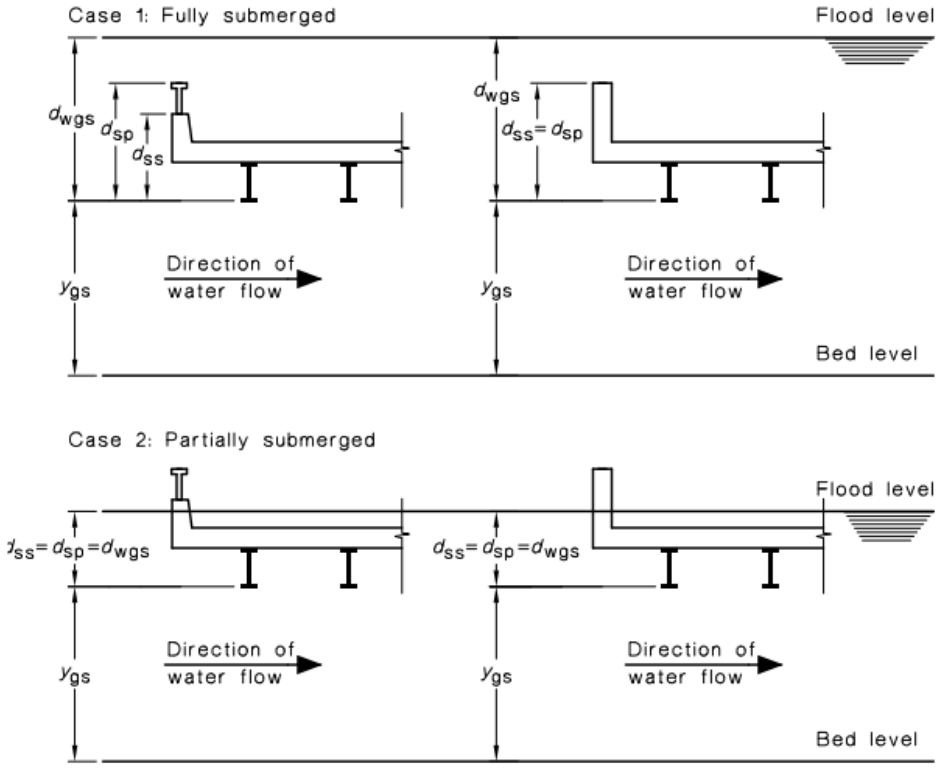

Figure 10: calculation of relative submergence S_R and proximity ratio P_r (7)

To calculate the lift force according to Equation 2-9, both an upper and lower value of C_L should be determined. The upper value is used for determination of the resistance against overturning and uplift, while the lower value is used when designing for example the girders and foundations.

$$F_{Ls} = \frac{1}{2}\rho C_L U_u^2 A_L \qquad \text{Equation 2-9}$$

where

F_{Ls} Lift force on bridge deck [N[

C_L	Is obtained from Figure 11	[-]

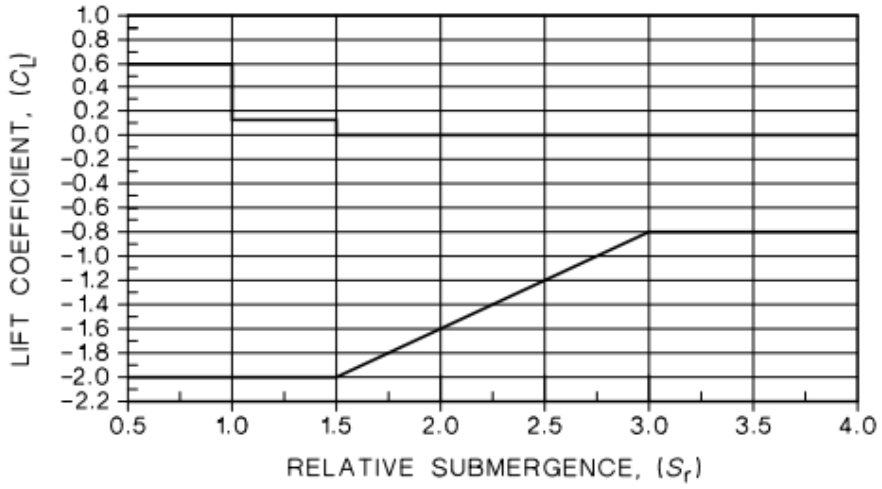

Figure 11: lift coefficient on bridge superstructure (7)

U_u	Mean flow velocity at the level of debris	[m/s]
A_L	Area of the bridge deck from plan view (length × width)	[m^2]
S_R	Relative submergence = d_{wgs} / d_{sp}, see Figure 10	[-]

2.2 Formation and effects of debris

2.2.1 Australian Bridge Design Standards AS5100 (2004) (7)

AS5100 also provides design formulas for loads on bridge when debris accumulations have formed against them. Equation 2-10 is to be used for calculation of drag forces on piers with debris. An important aspect to notice is that drag coefficient actually depends on velocity; drag coefficient is higher when the flow velocity is lower.

$$F_{dpd} = \frac{1}{2}\rho C_{d,1} U_u^2 A_{deb} \qquad \text{Equation 2-10}$$

where

F_{dpd}	Drag force on the pier with debris	[N]

$C_{d,1}$	Is obtained from Figure 12	[-]

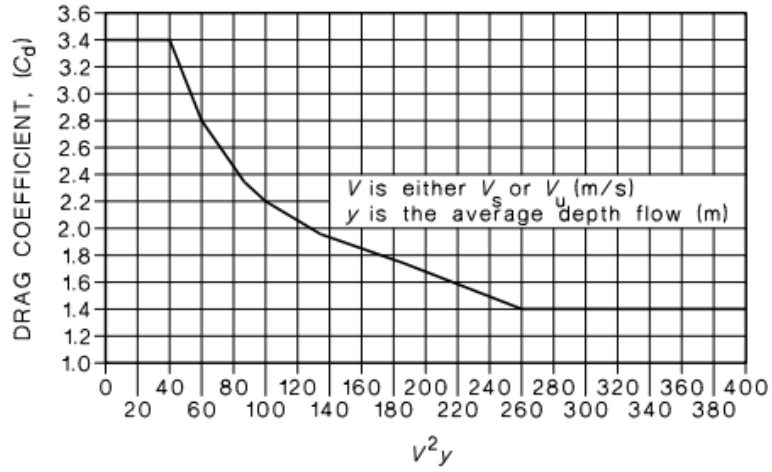

Figure 12: Calculation of drag coefficient for a pier with debris (7)

U_u	Mean flow velocity at the level of debris	[m/s]
A_{deb}	Projected area of the debris	[m^2]

Equation 2-11 needs to be used to find the design value of drag forces on superstructures with debris. Here, too, the drag coefficient is dependent on the flow velocity, in such a way that higher flow velocities correspond to lower drag coefficients.

$$F_{dsd} = \frac{1}{2}\rho C_{d,2} U_u^2 A_{deb} \qquad \text{Equation 2-11}$$

where

F_{dsd}	Drag force on the superstructure as a result of debris	[N]
$C_{d,2}$	Is obtained from Figure 13	[-]

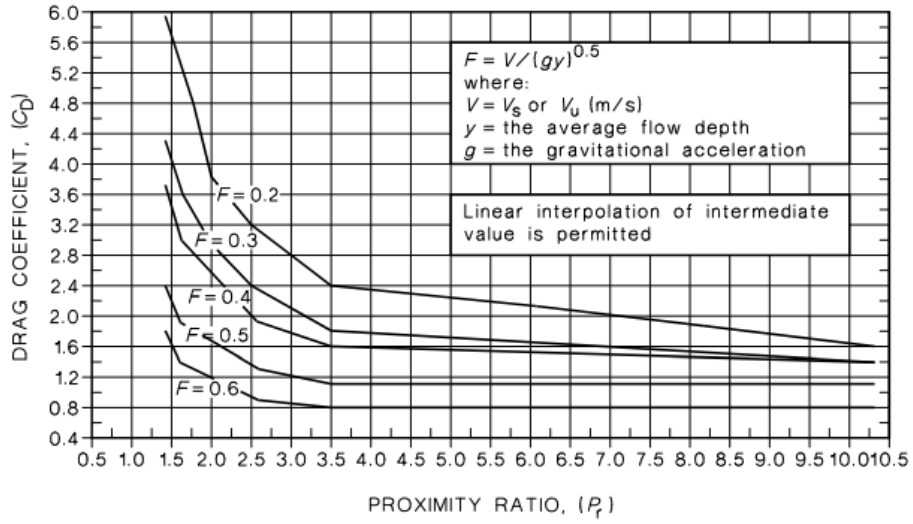

Figure 13: calculation of drag coefficient for a superstructure with debris (7)

U_u	Mean flow velocity at the level of debris	[m/s]
A_{deb}	Projected area of the debris	[m^2]

Lastly, the design code also provides a basic expression, Equation 2-12, for impact forces of logs, based on full dissipation of the kinetic energy of the logs.

$$F_{log} = 0.5 * \frac{mU_u^2}{\Delta s}$$ Equation 2-12

where

F_{log}	Impact force of a log	[N]
m	Mass of the log. It is assumed that the minimum mass is 2000 kg.	[kg]
U_u	Mean flow velocity at the level of debris	[m/s]
Δs	Stopping distance of the log. 150 mm for hollow concrete piers, 75 mm for solid concrete piers.	[m]

2.2.2 NCHRP Report 445 – Debris Forces on Highway Bridges (8)

This study focused on the development of a practical method for determining maximum loads caused by debris on bridge piers and superstructures, and subsequently development of appropriate design criteria.

Debris accumulation has an effect on the entire flow pattern, in particular it causes flow contractions leading to locally increased flow velocities.

The report points out that the drag coefficients for debris forces on piers and superstructures is heavily dependent on the blockage ratio B of the channel, defined as:

$$B = \frac{A_b}{A_b + A_c}$$ Equation 2-13

where

B	Blockage ratio of the flow	[-]
A_b	Flow area blocked by debris	[m^2]
A_c	Unobstructed cross-sectional flow area	[m^2]

Predictions of loading by debris are best achieved by dividing the total streamwise force into a drag component and a hydrostatic component. In general, the drag coefficient decreases as the blockage ratio increases, while the hydrostatic component of the total force increases. The velocity of the contracted flow should be used as reference velocity in the expressions for drag force. For small blockage ratios, the drag coefficients depend on the Froude number of the flow, in the way that higher Froude numbers gave rise to lower C_D's.

A conservative estimate of the drag coefficient for piers and superstructure was given in the form of an envelope curve, see the following figure.

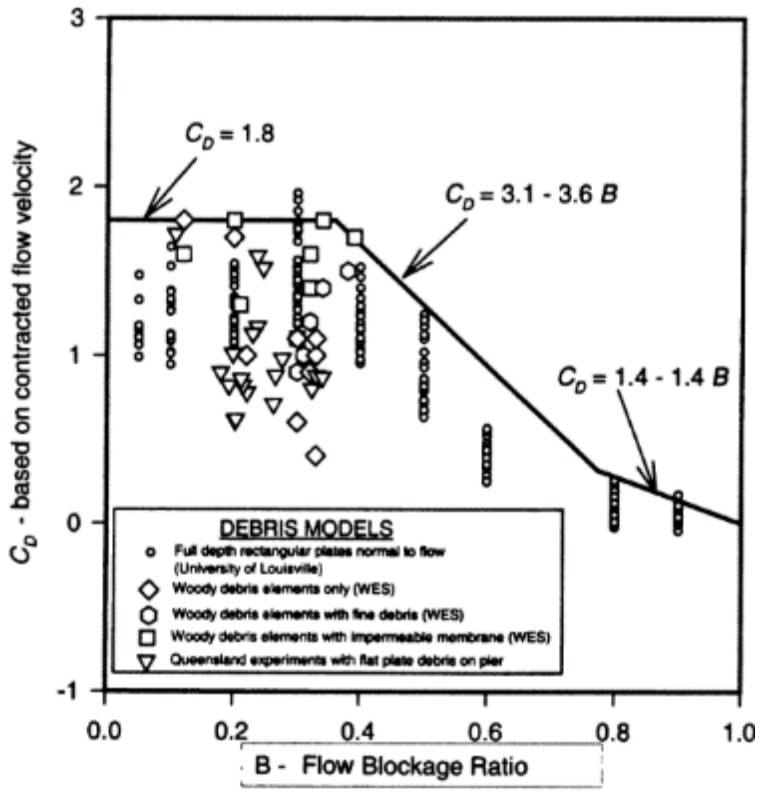

Pier

B - Range	Fr - Range	C_D
B < 0.36	Fr < 0.4	C_D = 1.8
B < 0.36	0.4 < Fr < 0.8	C_D = 2.6 - 2.0 Fr
0.36 < B < 0.77	Fr < 1	C_D = 3.1 - 3.6 B
B > 0.77	Fr < 1	C_D = 1.4 - 1.4 B

Figure 14: Debris drag coefficient for bridge piers

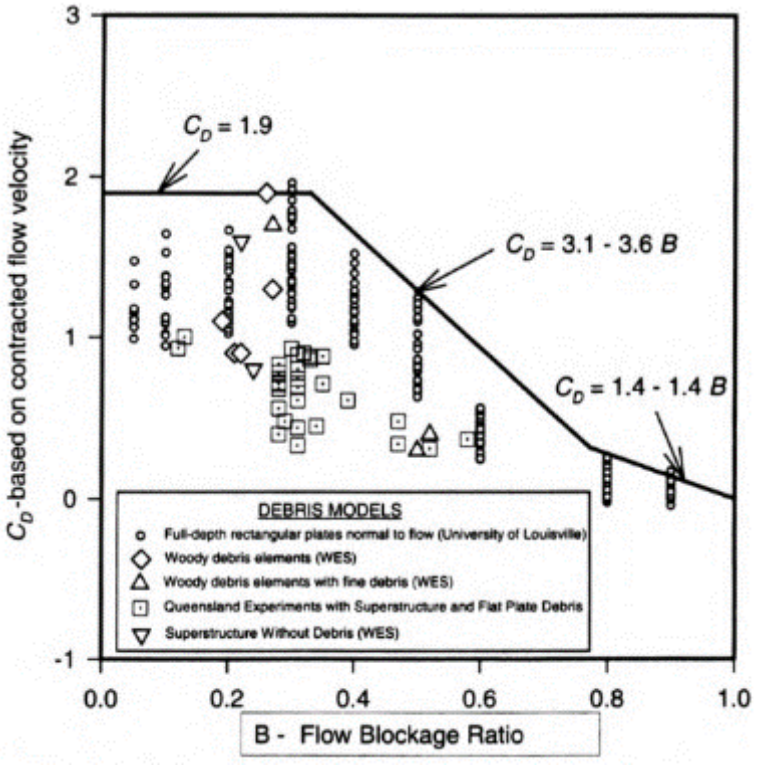

Superstructure

B - Range	Fr - Range	C_D
B < 0.33	Fr < 0.4	C_D = 1.9
B < 0.33	0.4 < Fr < 0.8	C_D = 2.8 - 2.25 Fr
0.33 < B < 0.77	Fr < 1	C_D = 3.1 - 3.6 B
B > 0.77	Fr < 1	C_D = 1.4 - 1.4 B

Figure 15: Debris drag coefficient for bridge superstructures

2.3 SUMMARY

Hydrodynamic forces on bridge superstructures and bridge piers are difficult to predict accurately. Force coefficients valid in unbounded flow do not hold in a situation with a free surface. Theoretical, numerical and experimental research has been performed to find relationships between the forces and many different parameters such as geometry of the structure, flow characteristics (velocity, depth etc.), position in the river with respect to the bed and presence of debris. Post-failure investigations of river bridges actually exposed to these hydrodynamic forces very limited. It has not yet been tested whether the (mostly experimental) work done by previous researchers can be used to explain the collapse of an actual bridge in the field.

This research will build further upon the investigations carried out by Kerenyi et al. which were reported on in (6). Also, the design guidelines in the Australian design codes (7) will be used extensively.

3 HYPOTHESES AND PREDICTIONS

When examining post-failure photographs of river bridges that have failed as a result of overtopping due to flooding rivers, it can be seen that usually the piers of the bridge survive the flooding event. In the case of the Japan-bridge, the piers have also toppled over. Two hypotheses are stated which can explain the complete destruction of the bridge.

The first hypothesis suggests that the connection between the bridge deck and the bridge pier failed before the pier toppled over. In other words, the hydrodynamic forces of the flooding river pushed and/or rotated off the bridge deck first at a certain combination of flow depth and flow velocity. This is turn caused the acting downward force (weight) on the bridge pier to decrease significantly, which translates into less resistance against rotation. The hydrodynamic forces acting upon the bridge pier then were enough to rotate and/or push it of off its foundation. The process is shown schematically in Figure 16.

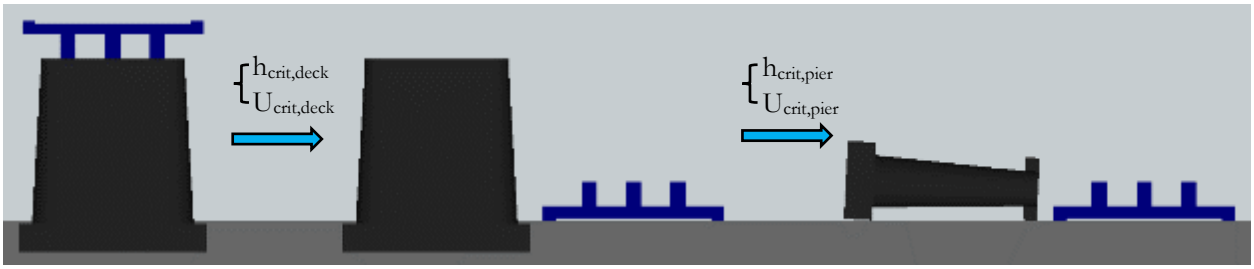

Figure 16: subsequent failure of the deck and the pier (hypothesis 1)

According to the second hypothesis, the connection between the bridge deck and the bridge pier was still intact when collapse happened. The bridge collapsed as a whole, and separation of the pier and deck only occurred because of the impact forces associated with the structure toppling over and impacting on the riverbed, as shown in Figure 17. Because the connection between the deck and the pier is located at the end of a girder, two deck segments must have failed together with the bridge pier according to this hypothesis.

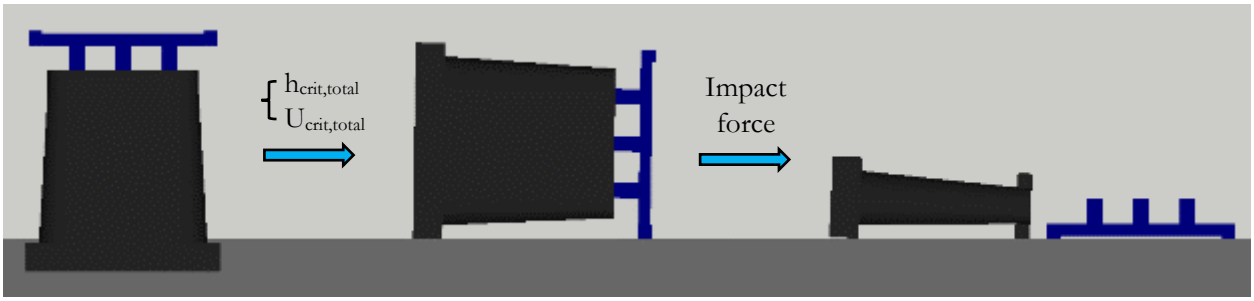

Figure 17: simultaneous failure of the bridge deck and pier (hypothesis 2)

For both hypotheses the effect of debris accumulation will also be investigated.

The flowchart in Figure 18 serves as a guide for chapter. Figure 19 shows positive directions for drag force (F_D), lift force (F_L), buoyancy force (F_B) and moment (M) on an object that will be used throughout this thesis.

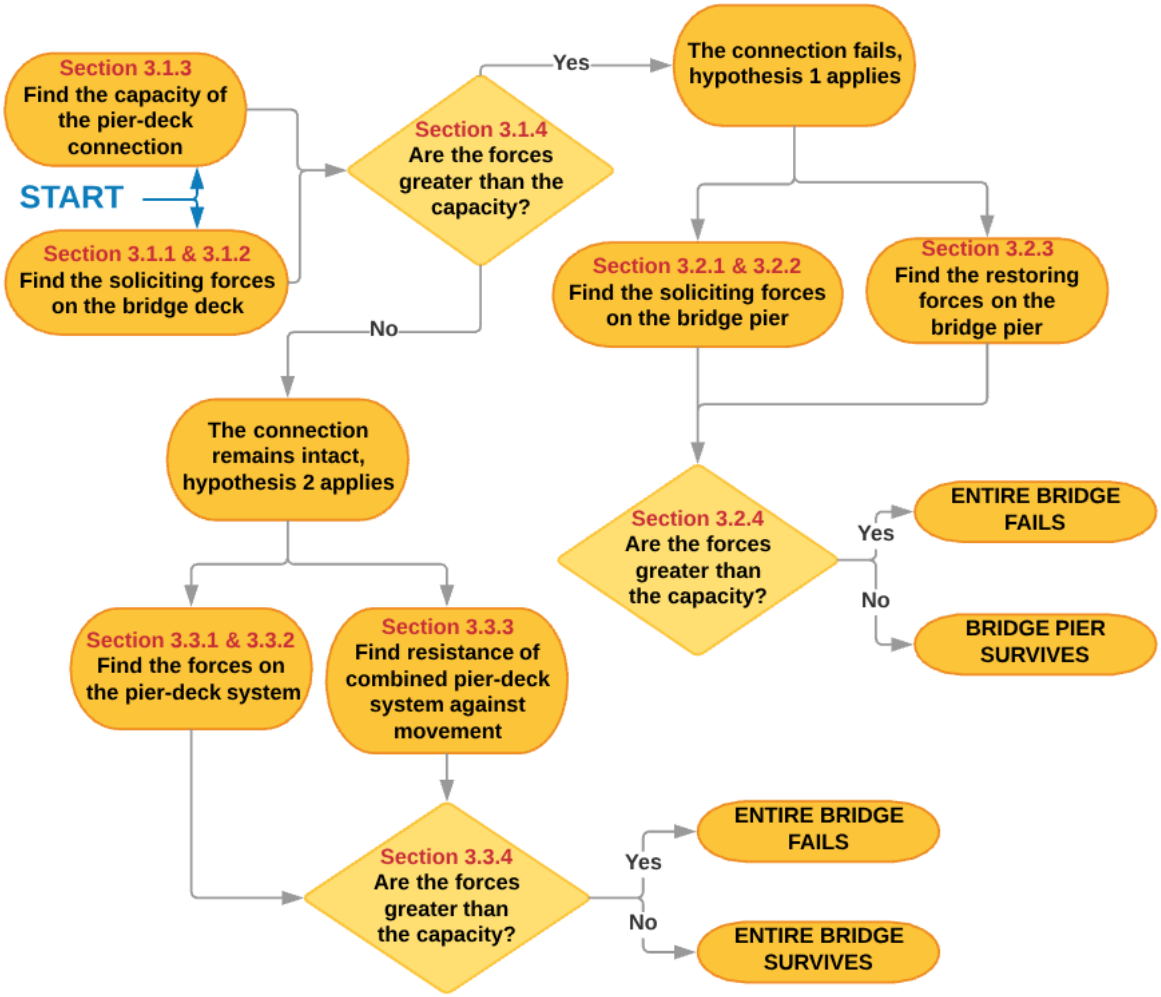

Figure 18: flowchart of chapter 3

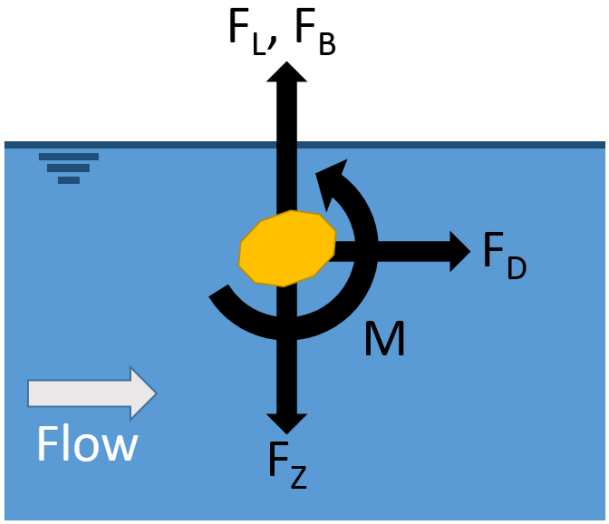

Figure 19: positive directions of frequently used forces

It is useful to define several dimensions of the bridge and give them a unique name, as has been done in Table 1. The origin of these dimensions is detailed in Appendix A. Figure 20 shows these constants in a schematic drawing of a cross-section of the bridge.

Constant	Value (field)
h_b	4641 mm
h_{base}	4362 mm
$h_{base,atk}$	4251 mm
$h_{base,udg}$	111 mm
h_{cap}	390 mm
h_{embed}	913 mm
h_{fnd}	802 mm
h_{girder}	695 mm
h_p	5554 mm
h_{rail}	700 mm
h_{road}	405 mm
h_u (water depth)	variable
s_f	1800 mm
s_m	1100 mm

Table 1: most important dimensions of the pier and deck

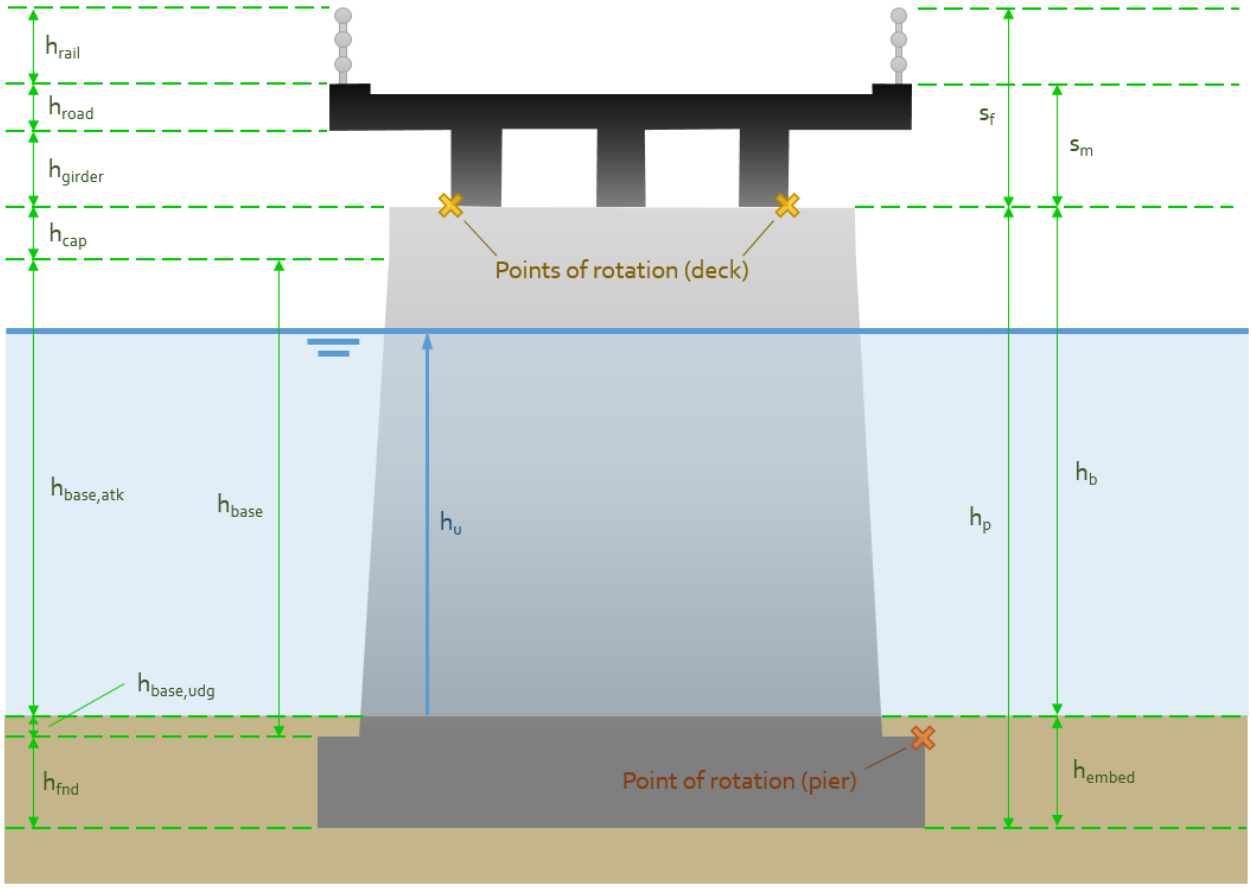

Figure 20: vertical distances of the pier and deck

3.1 HYPOTHESIS 1: DECK

With help of the previously conducted research on hydrodynamic forces on bridge decks, both with and without debris, as discussed in chapter 2, predictions of the soliciting forces (such as drag force, lift force and overturning moment) under various river conditions can be made. The connection between the pier and the deck provided the resistance to movement of the bridge deck against these forces. This section explores whether the capacity of the connection was sufficient to resist the hydrodynamic forces.

3.1.1 HYDRODYNAMIC FORCES WITHOUT DEBRIS

The report of the FHWA (6) provides drag, lift and moment coefficients for a 3-girder bridge with a geometry quite similar to the Yabitsu Bridge. These coefficients are used to calculate hydrodynamic forces on the bridge deck. The data in Table 2 is taken from figures 31, 32 and 33 of that report.

Derived for Fr = 0.32	h*								
	0,00	0,25	0,50	0,75	1,00	1,25	1,50	1,75	2,00
C_D	n/a	1,50	1,30	1,05	1,10	1,50	1,60	1,65	1,75
C_L	n/a	-0,15	-0,40	-1,35	-1,55	-1,20	-0,95	-0,65	-0,40
C_M	n/a	0,07	0,05	0,08	0,10	0,03	0,02	0,00	-0,07

Table 2: Drag, lift and moment coefficients as given by the FHWA for a three-girder bridge

These coefficients can be used in Equation 2-5, Equation 2-6 and Equation 2-7 to calculate the drag and lift forces as well the moment on the bridge. The equations are repeated here for clarity.

$$F_D = \frac{1}{2} C_D \rho U^2 s \qquad \text{if} \quad h^* \geq 1$$

$$F_D = \frac{1}{2} C_D \rho U^2 h^* s \qquad \text{if} \quad h^* < 1$$

$$F_L = \frac{1}{2} C_L \rho U^2 B$$

$$M_{cg} = \frac{1}{2} C_M \rho U^2 B^2$$

As was explained in paragraph 2.1.6, the value of C_M and thus M_{cg} stems from eccentricity of the drag and/or lift forces relative to the center of gravity. Figure 21, Figure 22 and Figure 23 show drag, lift and moment respectively, as a function of inundation ratio for different Froude numbers. It must be noted that these graphs were made using coefficients that were originally derived for the $Fr = 0.32$ case, therefore the accuracy of the predictions at higher or lower Froude numbers may be off by a few percent.

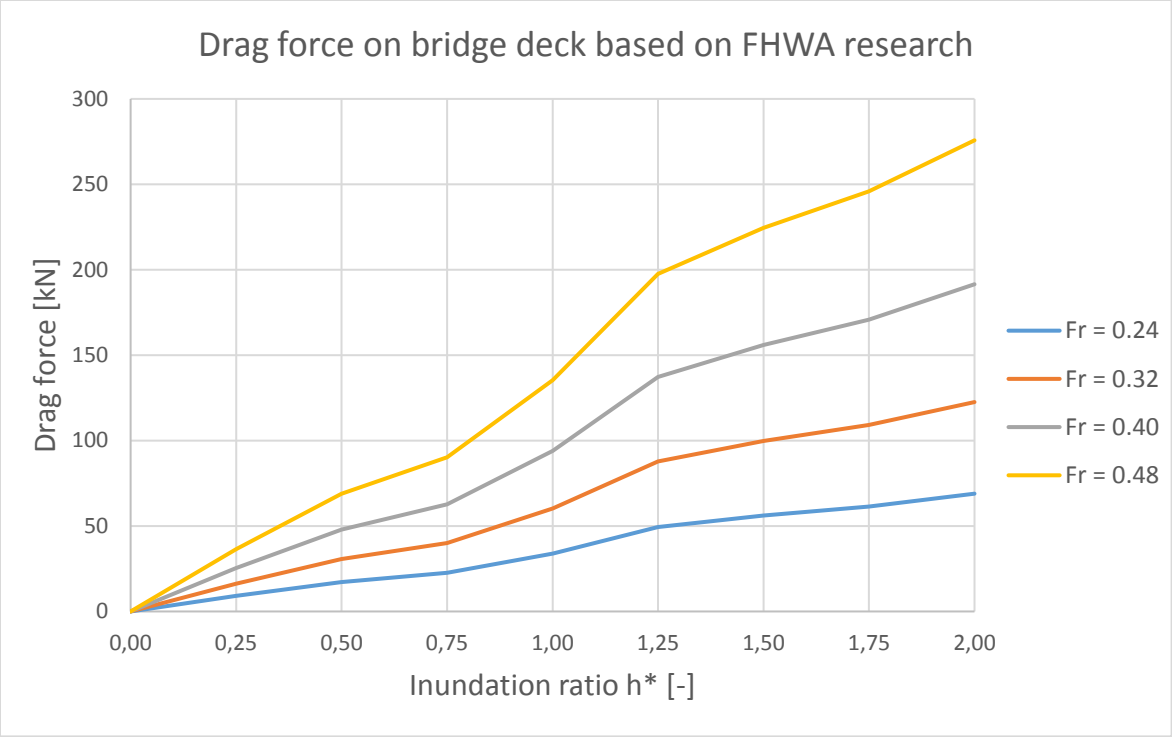

Figure 21: predicted values of the drag force on the bridge deck based on FHWA research

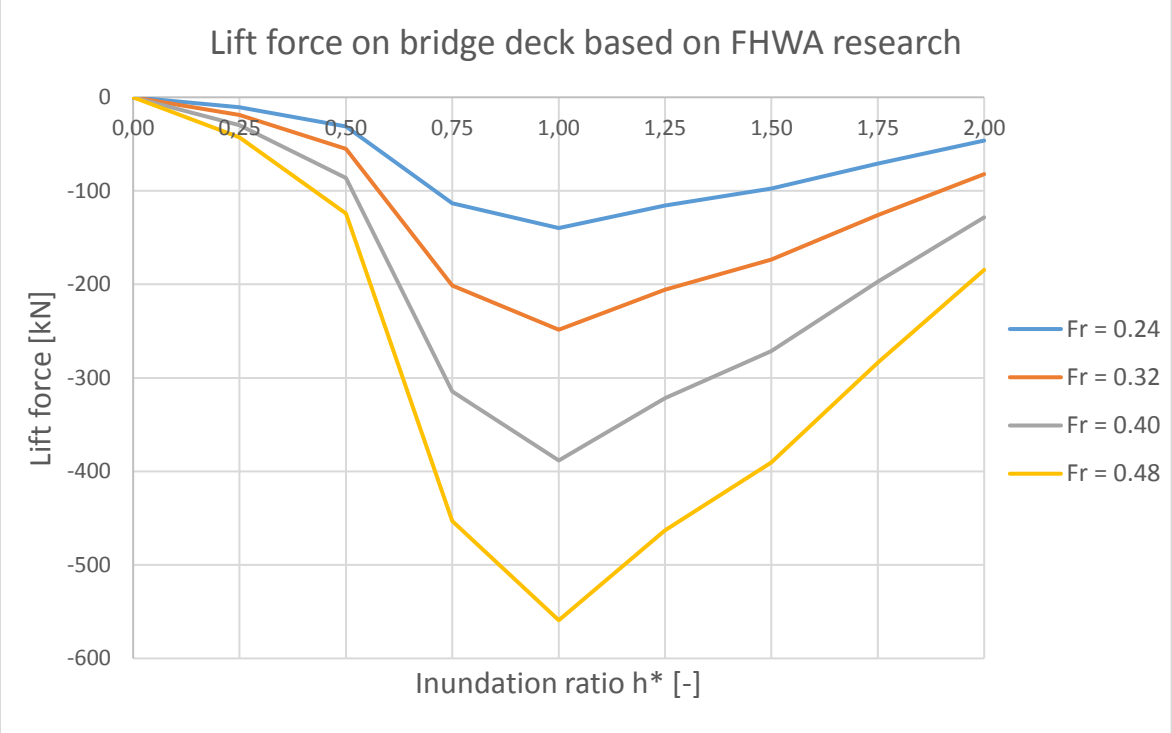

Figure 22: predicted values of the lift force on the bridge deck based on FHWA research

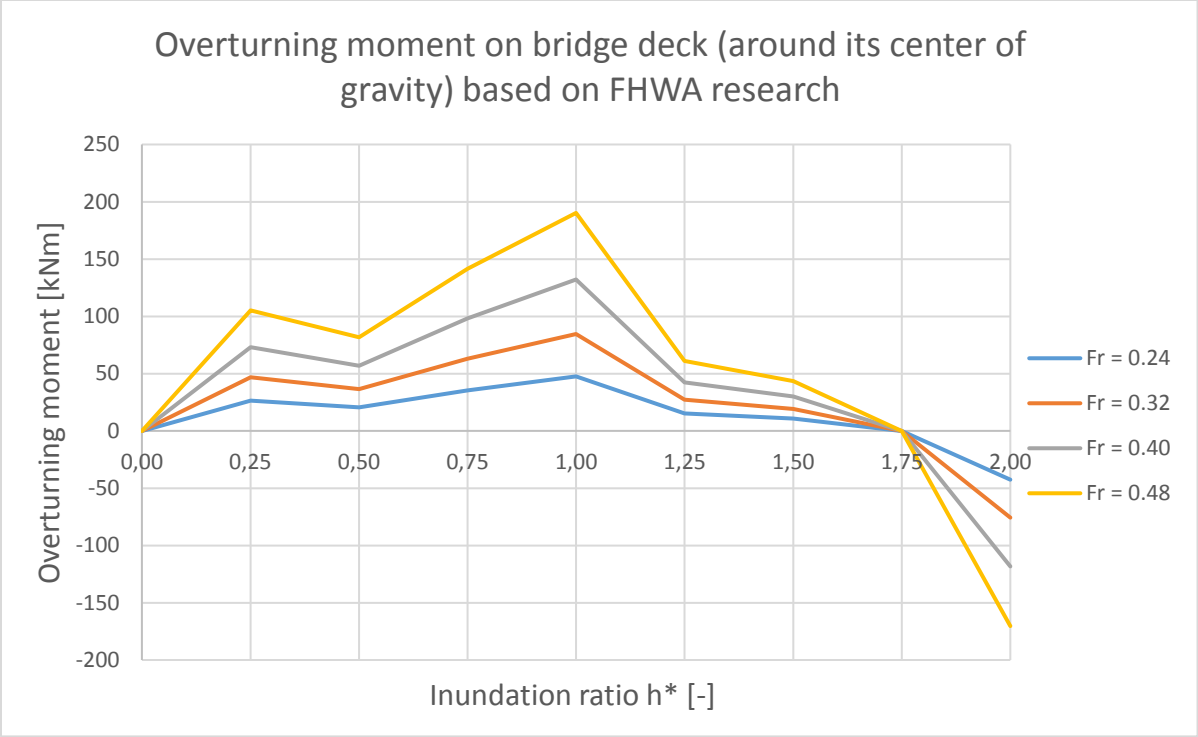

Figure 23: predicted values of overturning moment on the bridge deck based on FHWA research

3.1.2 HYDRODYNAMIC FORCES WITH DEBRIS

Potential for debris accumulation against the bridge over the Yabechi River was large. The area upstream of the bridge is foresty and many trees grow on the steep banks of the river. The river is a heavily meandering one, as a result many gravel plains form in the inner bends of the river at low discharge levels where much debris can accumulate. When the water level in the river rises, a large debris load from these plains suddenly enters the river. On post-failure photographs of the bridge (see section 1.1) a lot of debris can also be seen still lodged against the destroyed bridge components.

It is difficult to estimate the additional forces on bridge superstructures caused by debris accumulations due to their large variability in permeability, size and effects on the surrounding flow. As pointed out in (8), drag coefficients for use in a general drag force equation such as Equation 2-5 can vary anywhere from 0.6 to 3.5 depending on many factors.

The research done by Kerenyi et al. for the FHWA didn't focus on the effects of debris, so another source is used for the estimation of hydrodynamic forces on bridge decks with debris. Equation 2-11 from the Australian design standard AS5100 (see also section 2.2.1) provides a design value (i.e. a safe, conservative, upper bound value) for the drag force. For this calculation the exact shape of the debris accumulation is not needed, only the projected frontal area. It is assumed that the debris covers the entire face of the bridge deck segment and extends down into the flow by approximately half the height of the deck. This assumption is based on research by Wellwood and Fenwick (9) and was also used by Jempson in (2), who used a scaled model of a typical debris accumulation approximately 1.5 times the height of the bridge deck (Figure 24). AS5100 does not provide any information on altered lift or moment.

Figure 24: photo of experimental work performed at University of Queensland (Jempson, 2000)

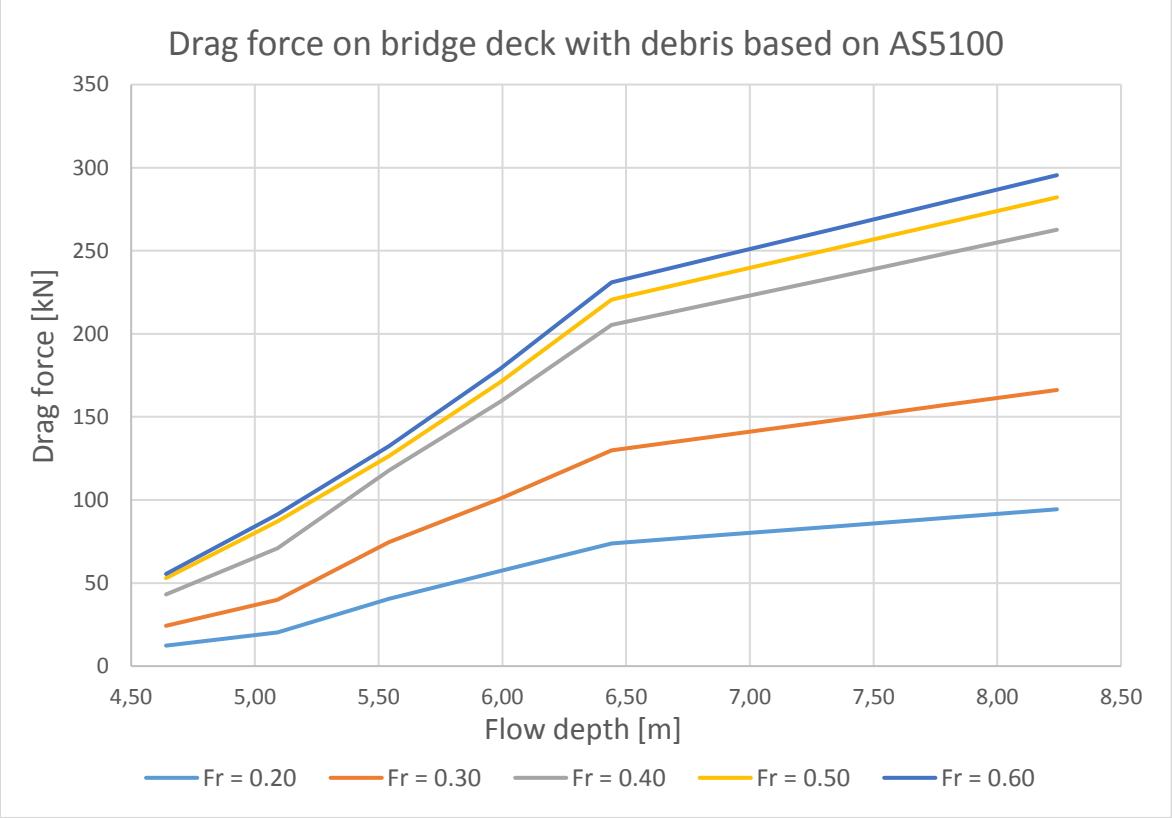

Figure 25: Predicted drag force on a bridge deck with debris according to AS5100 for different Froude numbers.

3.1.3 CAPACITY OF THE CONNECTION

The type of connection between the bridge deck and bridge piers plays a critical role in the governing failure mechanism of a bridge. Two limit cases of the deck-pier connection are given; a bridge of which the deck-pier connections are completely rigid (i.e. the deck and pier being monolithic) will fail as a whole by rotation around the foundation of the pier when it is exposed to a lateral (hydrodynamic) force and its movement in the lateral direction is restricted, assuming that the concrete material itself does not fail. This process is in accordance with the second hypothesis explained in the introduction of this chapter. The other limit case is described by a deck-pier connection which doesn't restrain movement between the two components at all (so there is not much of a connection to speak of). A bridge deck sitting on a frictionless surface of the pier by gravity only would fit this type of 'connection'. When subjected to the same conditions, this will result in subsequent failure of the deck by sliding off the pier and the pier by rotation, which describes the first hypothesis. In conclusion, the type of connection and its strength determines the failure mechanism.

Unfortunately, it is not possible to state with any degree of certainty the type and strength of the pier-deck connection of the bridge crossing the Yabechi River, as this information was lost by Japanese authorities. Regardless of the connecting method used, it is however possible to say that the connection that existed between the bridge deck and the bridge pier was in between the two limit cases. There is no middle ground when it comes to the question how the piers must have toppled over; either they toppled over on their own, or when the deck was still connected.

Upon closer inspection of the post-failure photographs of the bridge (Figure 26 and Figure 27), remnants of what seem to be bearings can be seen on both the bridge pier and bridge deck at positions where one would expect to find those. Bearings are structural elements that allow for some displacement or rotation between two components while still facilitating transfer of forces and moments between them, and are commonly found in bridges as the connection between a bridge deck and pier.

Figure 26: collapsed pier showing remains of a bearing

Figure 27: dislodged bridge deck segment showing remains of a bearing

Many different types of bearings exist. A type of bearing known as an elastomeric bearing is often used for short-span, reinforced or prestressed concrete bridge girders such as the bridge under investigation. Ease of installation, low cost maintenance and favorable expansion/compression characteristics contributed that elastomeric bearings are now in service in thousands of bridges worldwide (10).

It is likely that this type of bearing was also used in the design of the collapsed bridge. This is evidenced by the sole plates which are clearly visible still anchored to the pier and to the undersides of the bridge girders. Sole plates are typically steel plates which are anchored to the concrete with dowels or studs on one side, and vulcanized to the elastomeric material (neoprene or rubber) on the other side. A schematization of an elastomeric bearing with sole plates and anchors is shown in Figure 28.

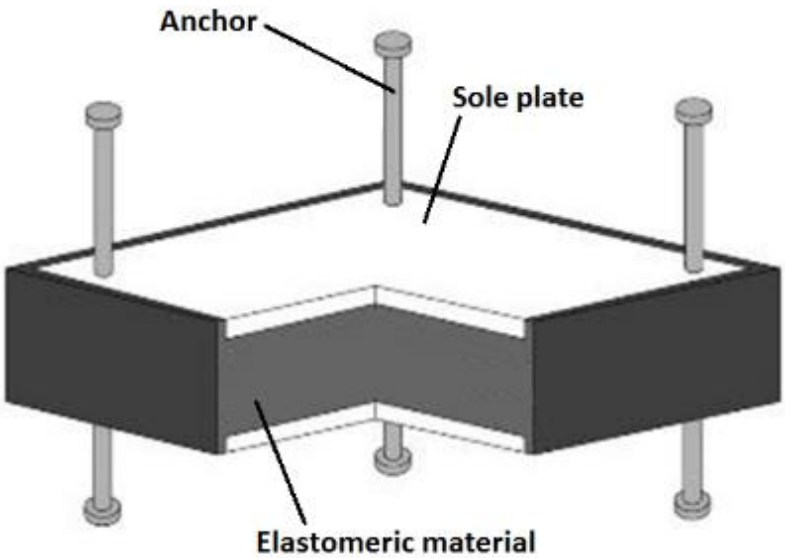

Figure 28: schematic drawing of a reinforced elastomeric bearing with sole plates and anchors (adapted from C. van der Veen, 2018)

The following describes possible failure modes of an anchored elastomeric bearing and aims to predict the forces necessary to activate these modes for the bridge under investigation.

Excessive deformation

Equation 3-1 shows the relation between horizontal force and displacement of an elastomeric bearing, as shown in Figure 29.

$$H_D = \frac{G * A_{bear} * \Delta x}{t} \qquad \text{Equation 3-1}$$

where

H_D	Horizontal force against the bearing	[N]
G	Shear modulus of the elastomeric material	[N/m^2]
A_{bear}	Plan area of the bearing	[m^2]
Δx	Shear deformation	[m]
t	Thickness of the bearing	[m]

Figure 29: shear deformation Δx of an elastomeric pad with thickness t by a horizontal force H.

In order to prevent rollover at the edges and/or delamination of steel reinforcement due to fatigue in reinforced elastomeric bearings, too large deformations must be prevented (11). The phenomenon of rollover is shown graphically in Figure 30.

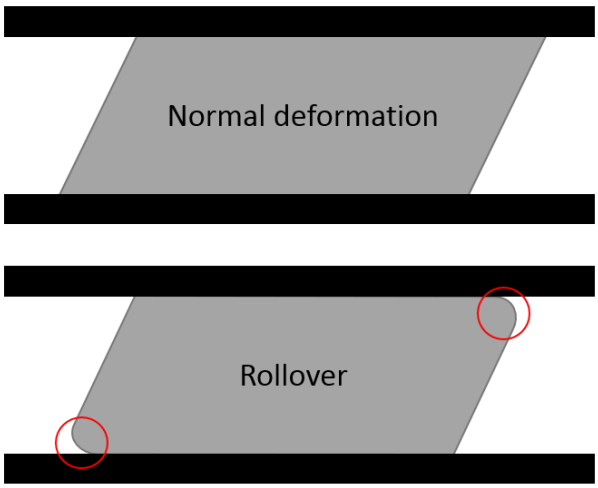

Figure 30: rollover mechanism in elastomeric bearings

The maximum safe shear deformation of the bearing Δx_{max} is defined differently by different design guidelines. Some define it as half of the bearing thickness [(10), (12), (13)] while others mention for example 70% of the

thickness as the maximum allowable deformation (14). Using the conservative value of 50%, the maximum horizontal force can be calculated with Equation 3-2.

$$H_{max,D} = \frac{1}{2} G A_{bear} \qquad \text{Equation 3-2}$$

where

$H_{max,D}$	Maximum horizontal capacity of the bearing (deformation failure mode)	[N]

The shear modulus G of the elastomer is an important property that takes on different values depending on the hardness of the material. The latter can be expressed either as "Shore A"-hardness or "IRHD"-hardness, depending on the testing method used. Different sources provide different values of the shear modulus for the various levels of hardness. See the following tables.

Hardness (Shore A)	50°	60°	70°
Shear Modulus *G*	0.68 MPa	1.04 MPa	1.69 MPa

Table 3: Different shear moduli for different types of elastomer according to manufacturer Cosmec (15)

Hardness (IRHD(± 2))	35	40	45	50	55	60	65	70	75
Shear Modulus (G) (MPa)	0.38	0.45	0.53	0.63	0.75	0.89	1.04	1.22	1.42

Table 4: Different shear moduli for different types of elastomer according to Lee (1994) (16)

From the post-failure photos it can be seen that there was a sole plate anchored to each girder supporting the bridge deck. There were a total of three girders with a sole plate on each end, therefore each deck element was supported by 6 bearings in total. The sole plates seem to be square in shape with the length of the sides equal to the width of a girder, which is about 435 mm according to the bridge drawings (see Appendix A). Therefore it assumed that the sole plates have an area A_{sp} of $(435)^2 = 189 \bullet 10^3$ mm² each. Furthermore it is assumed that the elastomer has the same area as the sole plate. A representative value of G = 1.00 MPa is also assumed.

According to Equation 3-2, the maximum horizontal force on a bearing pad will therefore be:

$$H_{max,D} = {}^1/_2 * 1.00 * 189 \cdot 10^3 = 95 \text{ [kN]}$$

Friction limit

Movement of the bearing pad along its mating surface should not be allowed. This is referred to as "slippage" and will occur when the lateral forces are higher than the friction factor multiplied by the actual normal force. See Equation 3-3.

$$H_{max,F} = \mu * (F_Z - F_L - F_B) \qquad \text{Equation 3-3}$$

where

$H_{max,F}$	Maximum horizontal capacity of the bearing (friction failure mode)	[N]
μ	Friction factor between elastomeric material and its mating surface	[-]
F_Z	Gravitational force	[N]
F_L	Hydrodynamic lift force	[N]
F_B	Buoyancy force	[N]

The friction factor of importance here is that between the elastomeric material and the steel sole plate. Different manufacturers of bearings refer to different friction factors, such as 0.20 (15) and 0.25 (17). (14) also states a range of friction fractors between 0.20 and 0.33. A friction factor of 0.25 will be assumed.

The gravitational force, lift force and buoyancy force follow from the weight of the deck, previous research and submerged volume of the deck, respectively. These values are taken directly from section 3.1.1.

Gravitational force F_Z	606,4	kN
Lift force F_L at h* = 1.00 and Fr = 0,32	-248,5	kN
Buoyancy force at full submergence	252,7	kN
Total normal force	**602,3**	**kN**

The maximum horizontal force against the bridge deck without "slippage" occurring will be, according to Equation 3-3:

$$H_{max,F} = 0.25 * (606.4 - -248.5 - 252.7) = 151 \text{ [kN]}$$

Anchorage

Failure of the anchorage(s) of the sole plates to the concrete bridge girder and/or the concrete piers is also a possibility. Because no specifics are known about the actual anchors used for the bearings, it is necessary to make some assumptions in order to assess the strength of the anchor. These are summarized below, together with a top view (more precisely, 'under view') of the girder and anchor.

Concrete strength class		C20/25	
	fck	20	N/mm2
Anchor type and steel properties	Headed stud		
	fy	435	N/mm2
	fu	500	N/mm2
Length of the anchor	hef	200	mm
Diameter of the anchor	d	20	mm
Edge distance parallel to force	ca1	60	mm
Edge distance perpendicular to force	ca2	450	mm
Anchor spacing parallel to force	sa1	315	mm

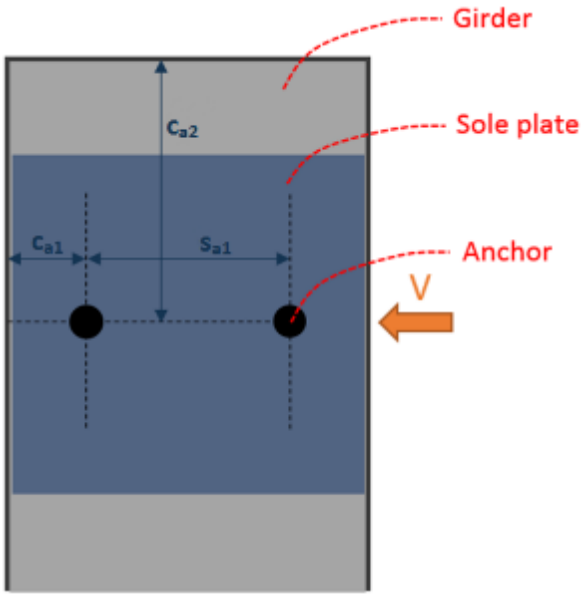

Figure 31: anchorage of the bearing sole plate

Anchor failure

It is assumed that steel headed studs were used for fulfill the role of anchor. These can easily be welded to a sole plate and cast into the concrete. The shear resistance of headed studs can be calculated according to Eurocode 4 part 1-1 section 6.6.3.1. Equation 3-4 describes the resistance of the headed stud to shearing of the steel and Equation 3-5 describes resistance of the concrete to crushing. The minimum of these two resistances is governing

$$P_{Rd} = \frac{0.8 f_u \pi d^2/4}{\gamma_V} \qquad \text{Equation 3-4}$$

where

P_{Rd}	Design value of the shear resistance of the headed stud	[N]
f_u	Maximum tensile stress of the steel	[N/mm²]
d	Diameter of the shaft of the headed stud	[mm]
γ_V	Partial safety factor (equal to 1.25)	[-]

$$P_{Rd} = \frac{0.8 * 500 * \frac{\pi * 20^2}{4}}{1.25} = 100531 \text{ [N]} = 101 \text{ [kN]}$$

$$P_{Rd} = \frac{0.29 \alpha d^2 \sqrt{f_{ck} E_{cm}}}{\gamma_V} \qquad \text{Equation 3-5}$$

where

P_{Rd}	Design value of the shear resistance of the headed stud	[N]
f_{ck}	Characteristic compressive strength of the concrete (cube)	[N/mm²]
d	Diameter of the shaft of the headed stud	[mm]
α	$0.2 * \left(\frac{h_{sc}}{d} + 1\right)$ for $3 \leq \frac{h_{sc}}{d} \leq 4$ 1 for $\frac{h_{sc}}{d} > 4$	[-]
E_{cm}	Modulus of elasticity of the concrete	[N/mm²]
γ_V	Partial safety factor (equal to 1.25)	[-]

$$P_{Rd} = \frac{0.29 * 1 * 20^2 * \sqrt{20 * 30000}}{1.25} = 71883\ [N] = 72\ [kN]$$

Ollgaard, Slutter and Fisher (18) produced a prediction equation for the capacity an anchorage using steel studs:

$$Q_u = 0.5 A_s \sqrt{f_c' E_c} \leq A_s F_{ut} \qquad \text{Equation 3-6}$$

where

Q_u	Nominal shear stud connector strength embedded in a solid concrete slab	[N]
A_s	Cross-sectional area of the stud shear connector	[mm^2]
f'_c	Concrete compressive strength	[N/mm^2]
E_c	Modulus of elasticity of the concrete	[N/mm^2]
F_{ut}	Ultimate tensile strength of the stud steel	[N/mm^2]

$$Q_u = 0.5 * (\pi * 10^2) * \sqrt{20 * 30000} = 121673\ [\text{N}] = 122\ [\text{kN}] \leq (\pi * 10^2) * 500 = 157080\ [\text{N}] = 157\ [\text{kN}]$$

Finally, ACI 318-14 17.5.1.2 (19) states that the nominal strength for a cast-in headed stud anchor shall not exceed

$$V_{sa} = A_{se,V} f_{uta} \qquad \text{Equation 3-7}$$

where

V_{sa}	Nominal strength of an anchor in shear	[N]
$A_{se,V}$	Effective cross-sectional area of an anchor in shear	[mm^2]
f_{uta}	Ultimate tensile strength of the stud	[N/mm^2]

$$V_{sa} = (\pi * 10^2) * 500 = 157080\ [\text{N}] = 157\ [\text{kN}]$$

From this comparison between different calculation methods, it is apparent that the resistance of the concrete against crushing according to the Eurocode is governing in this situation.

Concrete failure

The sole plate of the bearing is anchored at the end of a girder, which is a narrow concrete member. Anchorages that are located close to an edge of a concrete member can cause a breakout of the concrete at the side due to too high shear forces. ACI 318-14 17.5.2 (19) provides a method for calculating the resistance of concrete against this edge failure.

$$V_{cb} = \frac{A_{Vc}}{A_{Vc0}} \psi_{ed,V} \psi_{c,V} \psi_{h,V} V_b \quad \text{with} \quad V_b = \min\left\{ \left(0.66 \left(\frac{h_{ef}}{d} \right)^{0.2} \sqrt{d} \right) \sqrt{f_c'} c_1^{1.5} \ ; \ 3.7 \sqrt{f_c'} c_1^{1.5} \right\} \qquad \text{Equation 3-8}$$

where

V_{cb}	Concrete breakout strength	N

A_{Vc}	Approximate full surface area of the breakout cone for a particular arrangement of anchors.	[mm^2]
A_{vc0}	Maximum projected area for a single anchor that approximates the surface area of the full breakout cone for an anchor unaffected by edge distance, spacing or depth of a member. Equal to $4.5c_{a1}^2$	[mm^2]
$\psi_{ed,V}$	Modification factor for edge effect. Equal to 1.0 as long as $c_2 > 1.5c_1$. Otherwise $\psi_{ed,V} = 0.7 + 0.3 \times (c_{a2} / 1.5c_{a1})$	[-]
$\psi_{c,V}$	Modification factor for presence of reinforcement. Equal to 1.0 for calculations in cracked concrete without anchor reinforcement	[-]
$\psi_{h,V}$	Modification factor for the thickness of the concrete member. Equal to 1.0 as long as $h_a > 1.5c_1$	[-]
V_b	Basic concrete breakout strength for a single anchor	[N]

The code also states that if both anchors are welded to the same stiff steel plate, it is allowed to have the entire shear force V be carried by the anchor which is farthest away from the edge. The argument for this method lies in the redistribution of forces from the front anchor to the back anchor once a failure cone starts forming around the anchor closest to the edge. Therefore, in the following calculation, c1 = ca1 + sa1

$$V_{cb} = 0.90 * 0.94 * \min\left\{\left(0.66\left(\frac{200}{20}\right)^{0.2}\sqrt{20}\right)\sqrt{20} * (60 + 315)^{1.5}\ ;\ 3.7\sqrt{20} * (60 + 315)^{1.5}\right\} = 101656\ [\text{N}] = 102\ [\text{kN}]$$

The sole plate anchored to the pier is not close to any edges. Still, failure of the anchorage can occur by shear forces by a failure mode called pryout. Figure 32 shows the crack pattern and section of the concrete which fails that is typical for this type of failure.

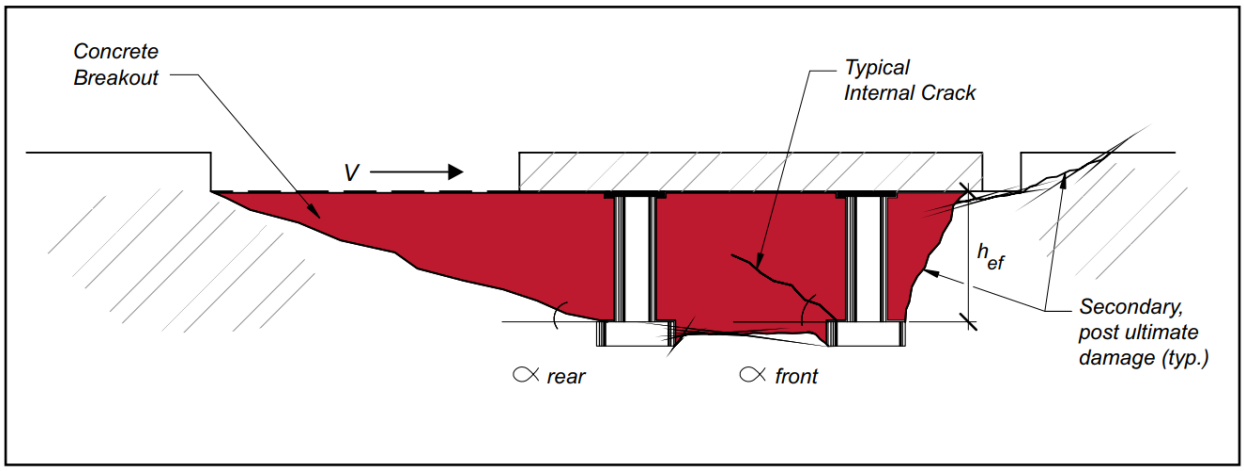

Figure 32: failure mechanism of concrete pryout failure due to shear (from Anderson and Meinheit (20))

Fuchs et al. (1995) (21) found that the pryout shear resistance of an anchor is closely related to the tensile breakout strength. This is reflected in ACI 318-14 17.5.3, where the pryout shear resistance for a group of anchors is given as

$$V_{cpg} = k_{cp} N_{cpg} \quad \text{with} \quad N_{cpg} = \frac{A_{Nc}}{A_{Nc0}} \psi_{ec,N} \psi_{ed,N} \psi_{c,N} \psi_{cp,N} N_b \quad \text{with} \quad N_b = \max\{ k_c \sqrt{f_c'} h_{ef}^{1.5} ; 3.9 \sqrt{f_c'} h_{ef}^{5/3} \}$$ Equation 3-9

Where

V_{cpg}	Concrete pryout strength for a group of anchors	[N]
N_{cpg}	Concrete breakout strength for a group of anchors	[N]
A_{Nc}	Actual projected concrete failure area of the anchorage, considering multiple anchors or proximity of edges.	[mm^2]
A_{Nc0}	Projected concrete failure area of a single anchor, placed sufficiently far from any edges. Equal to $9h_{ef}^2$	[mm^2]
$\psi_{ec,N}$	Modification factor for eccentricity. Equal to 1.0 as long as the tensile forces are not eccentric.	[-]
$\psi_{ed,N}$	Modification factor for edge effects. Equal to 1.0 as long as ca,min ≥ 1.5hef	[-]
$\psi_{c,N}$	Modification factor for cracking. Equal to 1.0 if cracked concrete due to service load levels is assumed.	[-]
$\psi_{cp,N}$	Modification factor for concrete splitting due to post-installed anchors. Equal to 1.0 if cast-in anchors are used.	[-]
k_{cp}	Factor, equal to 1 for hef < 60 mm and equal to 2 for hef ≥ 60 mm.	[-]
k_c	Factor, equal to 10 for cast-in anchors (when using SI units)	[-]
N_b	Basic concrete breakout strength of a single anchor in tension in cracked concrete	[N]

$$V_{cpg} = 2 * \frac{549 \cdot 10^3}{360 \cdot 10^3} * \max\{10 * \sqrt{20} * 200^{1.5} ; 3.9 * \sqrt{20} * 200^{5/3}\} = 385798\ [N] = 386\ [kN]$$

Table 5 summarizes the resistances of each of the failures modes investigated. It is apparent that sliding due to insufficient friction is the governing failure mode, as it provides the least amount of resistance. The frictional resistance depends on the lift force which in turn depends on the hydraulic conditions.

	Resistance of		
Failure mode	1 anchor	1 pad	1 deck
Friction	13	25	151
Deformation	47	95	568
Stud shear	72	144	863
Edge failure	51	102	610
Pryout	193	386	2315

Table 5: Resistances of the different failure modes of the connection. All values in kN, the values in red indicate the resistance calculated in this section

It needs to be stressed that this conclusion regarding the governing failure mechanism only holds for a bearing which is not fixed. Other types of bearings which are fixed (i.e. lateral movement in one or multiple directions is restricted) exist. A possible bearing configuration for the bridge deck under investigation is shown in Figure 33. Such a configuration restricts movement of the deck in X- and Y-direction while still allowing for thermal expansion for example. Obviously these types of bearings also have a finite resistance, which will be stated by the manufacturer. A typical 300 mm × 400 mm elastomeric bearing pad fixed in one or two direction can take up to 180 kN of lateral load (22). When two of these fixed bearings are used as in Figure 33, these provide a

resistance of at least 360 kN. This is more than double the resistance of friction only, but still less than all the other failure modes.

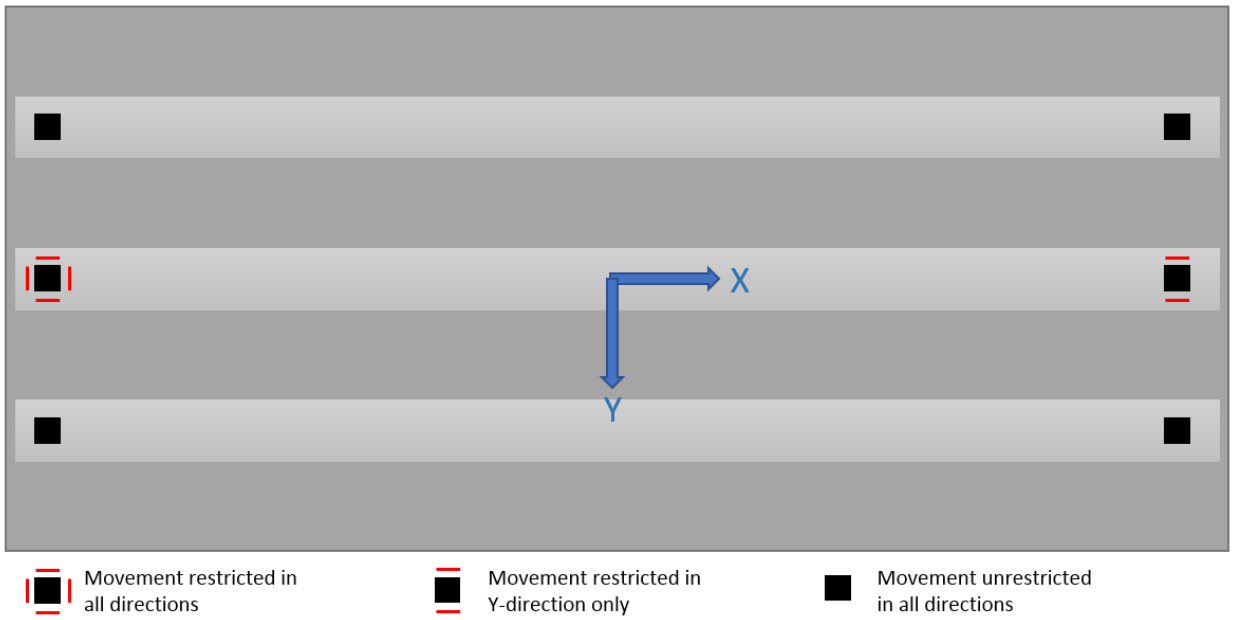

Figure 33: possible configuration of bearings on a bridge deck, fixing it in both X- and Y-directions, while still allowing for expansion in both directions.

3.1.4 RESISTANCE AGAINST MOVEMENT

A method to assess failure probability is use of a limit state function, $Z = R - S$, where R stands for restoring and S for soliciting. When Z becomes negative, the soliciting forces are greater than the restoring forces and the structure fails. Typically the limit state function is used in probabilistic calculations, i.e. when both the restoring and soliciting forces are distributed according to a certain probability distribution. In combination with a Monte Carlo analysis the probability of failure can then be calculated by finding the ratio of simulations in which $Z < 0$ to the total number of simulations performed. However, the concept of the limit state function can just as well be used for deterministic calculation and is preferred in this research over the concept of the unity check, defined as $UC = S / R$.

Equation 3-10, Equation 3-11 and Equation 3-12 define the limit state functions for vertical forces, lateral forces and overturning moments, respectively. Figure 34 shows the positive directions of forces in these expressions on the bridge deck. In the assessment of the resistance against movement it is assumed that the weight and buoyancy forces of the potential debris are not transferred to the deck. Also, the values of C_L and C_M are assumed to be identical in both the without-debris and the with-debris case. Hence, the values of $Z_{vert,d}$ are equal in both the without-debris and the with-debris scenarios.

$$Z_{vert,d} = R_{vert,d} - S_{vert,d} = F_{Z,d} - \left(F_{B,d} + F_{L,d}\right) \qquad \text{Equation 3-10}$$

where

$Z_{vert,d}$	Resistance against vertical movement of the deck, expressed in N	[N]
$R_{vert,d}$	Vertical restoring force of the deck	[N]
$S_{vert,d}$	Vertical soliciting force of the deck	[N]

$$Z_{hor,d} = R_{hor,d} - S_{hor,d} = F_{R,bear} - F_{D,d} \quad \text{where} \quad F_{R,bear} = F_F = \mu * Z_{vert,d}$$

Equation 3-11

where

$Z_{hor,d}$	Resistance against horizontal movement of the deck, expressed in N	[N]
$R_{hor,d}$	Horizontal restoring force of the deck	[N]
$S_{hor,d}$	Horizontal soliciting force of the deck	[N]
$F_{R,bear}$	Restoring force exerted on the bridge deck by the bearing	[N]
F_F	Frictional force	[N]

$$Z_{over,d} = R_{over,d} - S_{over,d} = F_{Z,d}L_{cg,d} - \left[(F_{L,d} + F_{B,d})L_{cg,d} + F_{D,d}h_{cg,d} - M_{cg,d}\right]$$

Equation 3-12

where

$Z_{over,d}$	Resistance against rotation of the deck, expressed in Nm	[N]
$R_{over,d}$	Restoring moment of the deck	[N]
$S_{over,d}$	Overturning moment of the deck	[N]
$L_{cg,d}$	Horizontal distance from the center of gravity to the point of rotation (deck)	[N]
$h_{cg,d}$	Vertical distance from the center of gravity to the point of rotation (deck)	[N]

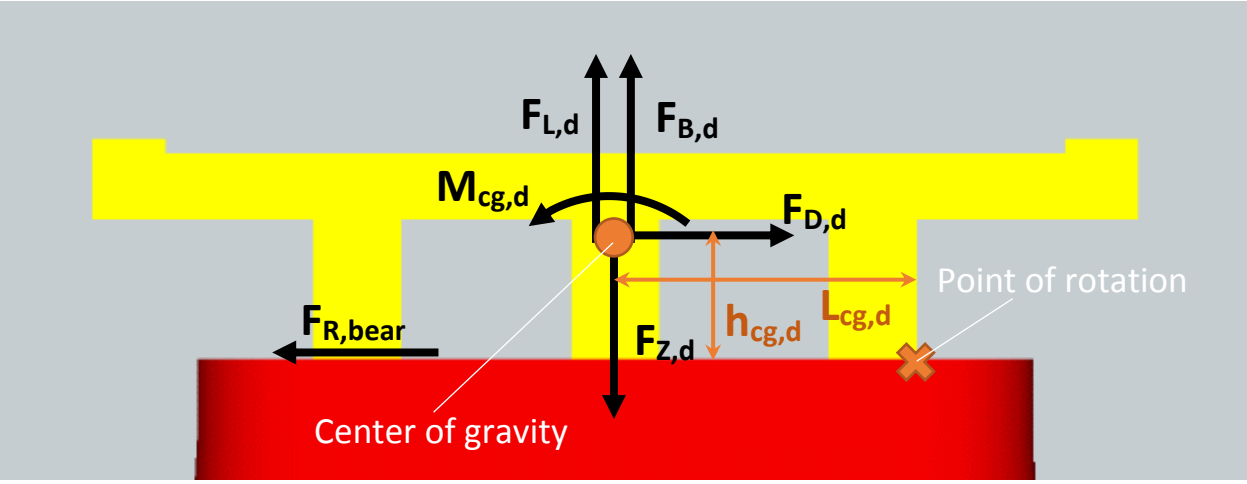

Figure 34: forces acting upon a submerged bridge deck

Figure 35 plots $Z_{vert,d}$, $Z_{lat,d}$ and $Z_{over,d}$ for both with and without debris (recognizable by either the + or – subscript) according to the data in sections 3.1.1, 3.1.2 and 3.1.3 for a constant Fr = 0.20 (inter- and extrapolation used where necessary). The resistance against lateral displacement approaches critical values as h^* > 2.00 at Fr = 0.20 for the scenario with debris, while resistances against vertical movement and overturning are sufficient. As a comparison the same plots are repeated in Figure 36, but for a constant Fr = 0.48. The following important observations can be made:

- Resistance against vertical movement and overturning is sufficient at all times. The deck will not fail by rotation or liftoff.
- At higher Froude numbers, the effect of debris on the inundation ratio at which the resistance to lateral movement is no longer sufficient, becomes smaller. In other words, at higher Froude numbers, the deck will fail at approximately the same flow depth, independent on the presence of debris.

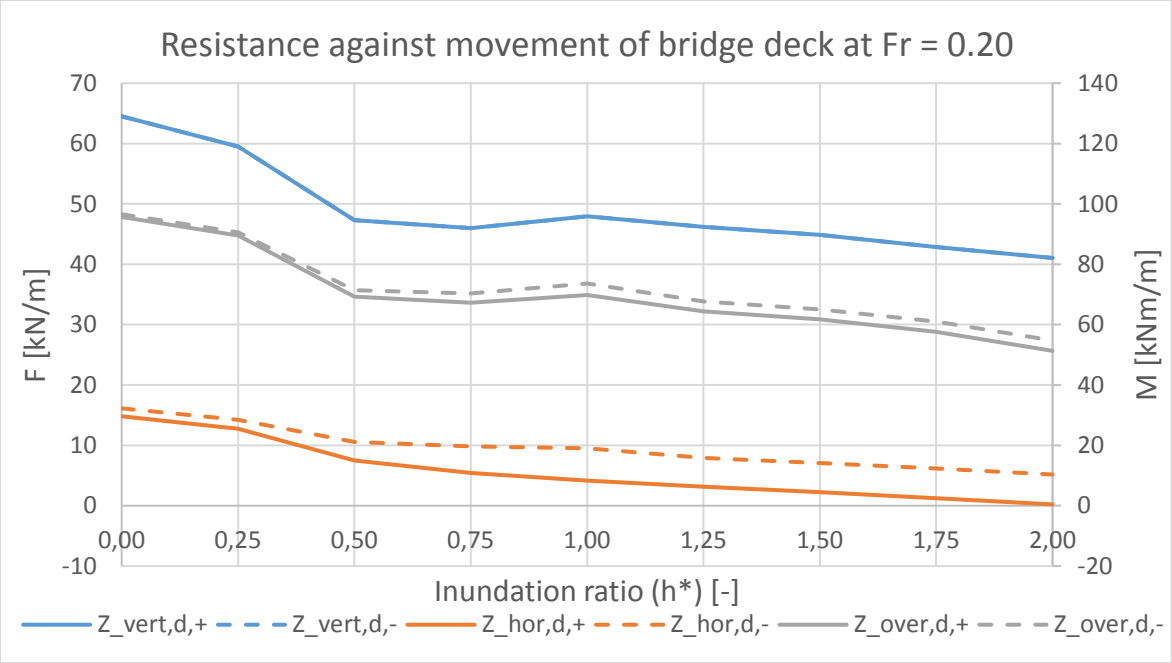

Figure 35: Resistance against movement of the bridge deck (predicted values, with and without debris, at Fr = 0.20)

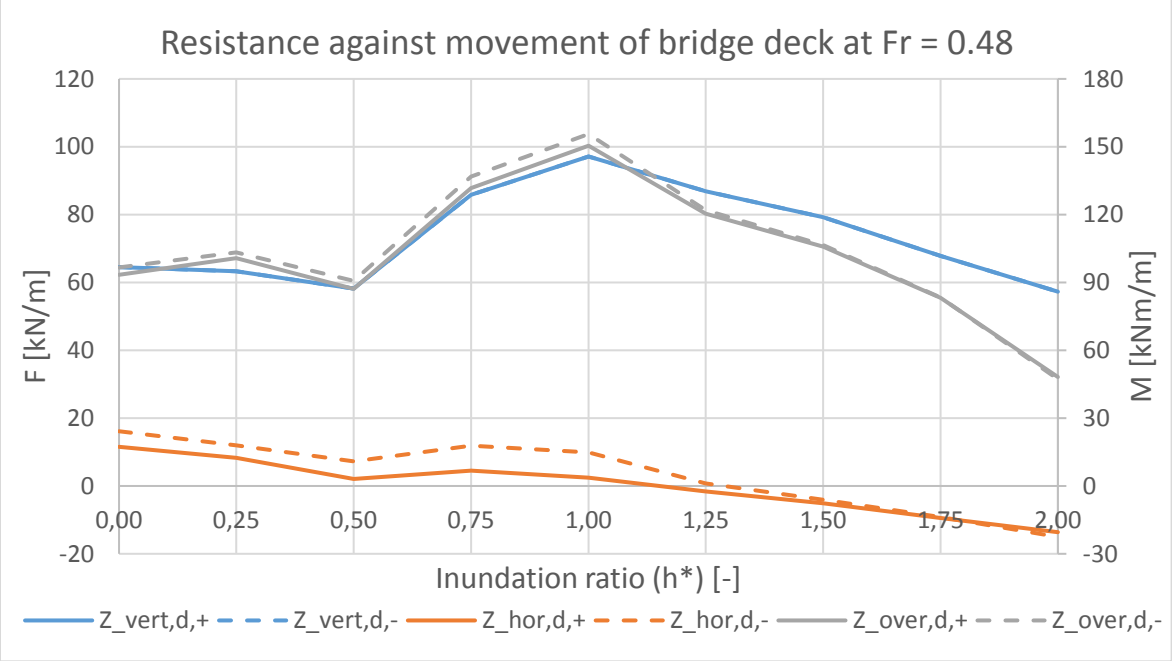

Figure 36: Resistance against movement of the bridge deck (predicted values, with and without debris, at Fr = 0.48)

3.2 HYPOTHESIS 1: PIER

This section aims to provide estimates of forces on the bridge pier. Only drag forces are taken into account, as it is assumed that no hydrodynamic lift forces will be exerted on the pier, at least not in the vertical direction. Any forces perpendicular to the flow (along the axis of bridge road) that would be caused by an asymmetric flow pattern around the pier due to a certain angle of attack of the flow, are not considered. Following these assumptions, the drag and buoyancy are the only forces creating an overturning moment, while the weight of the pier acts as the only restoring moment.

3.2.1 HYDRODYNAMIC FORCES WITHOUT DEBRIS

Estimates on the forces exerted on the pier are based on well-known basic fluid mechanics on the subject of flow around objects. The shape of the base of the piers is rectangular with rounded (circular) ends. The drag coefficient for this shape is approximately 0.7 (23). The top of the pier lacks well rounded ends, and a drag coefficient of 2.0 is more appropriate, comparable to a rectangular shape (24). It is assumed that the pier's only failure mode is rotation, as the embedment into the bedrock prevents lateral movement and the solid pier is so heavy that it will not be lifted. Rotation is assumed to be around the point indicated in Figure 37. This figure also indicates the manner in which the drag forces and overturning moments are estimated. Figure 38 shows the overturning moment on the bridge pier as a result of the drag force at a high constant Froude number of 0.60 and due to buoyancy according to Equation 3-13.

$$S_{over,p,-} = F_{D,p,base} e_{D,p,base} + F_{D,p,cap} e_{D,p,cap} + F_{B,p} L_{cg,p} \qquad \text{Equation 3-13}$$

$$F_{D,p,base} = \frac{1}{2} C_D \rho B_{p,a} U^2 * \min\{h_u; h_{base,atk}\} \text{ with } C_D = 0.7$$

$$F_{D,p,cap} = \frac{1}{2} C_D \rho B_{p,a} U^2 * \text{if}\{h_u > h_{baseatk}; \min\{h_u - h_{base,atk}; h_{cap}\}; 0\} \text{ with } C_D = 2.0$$

$$e_{D,p,base} = \min\{\frac{h_u}{2} + h_{base,udg}; \frac{h_{base,atk}}{2} + h_{base,udg}\}$$

$$e_{D,p,cap} = \min\{\frac{h_u - h_{base,atk}}{2} + h_{base}; \frac{h_{cap}}{2} + h_{base}\}$$

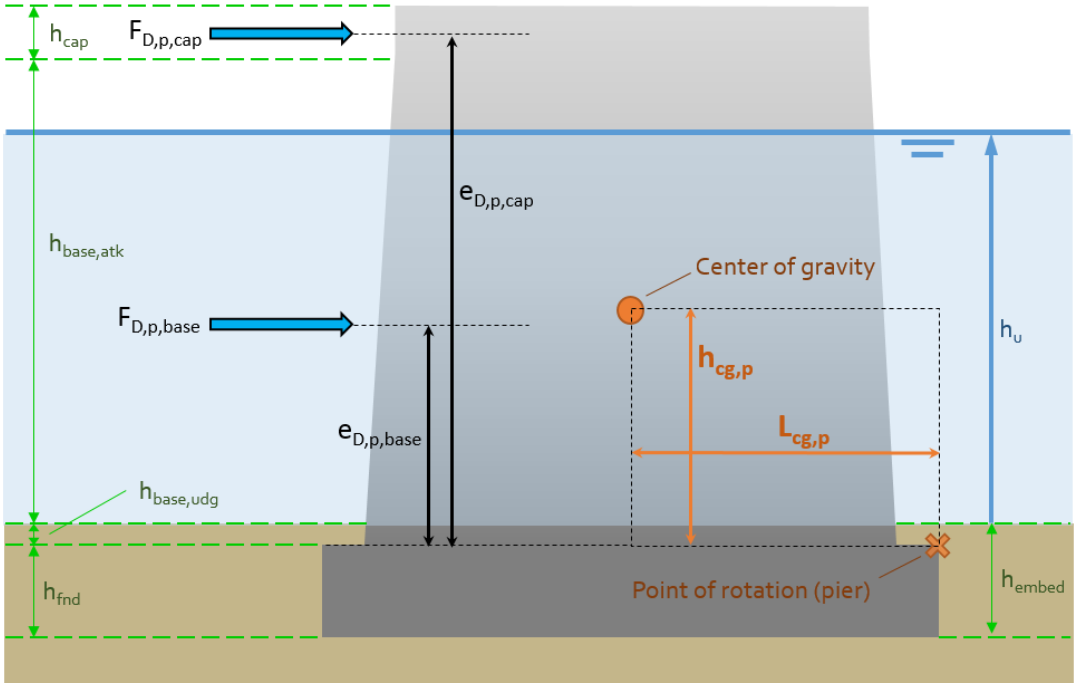

Figure 37: Drag forces on the pier and their eccentricities with respect to the point of rotation.

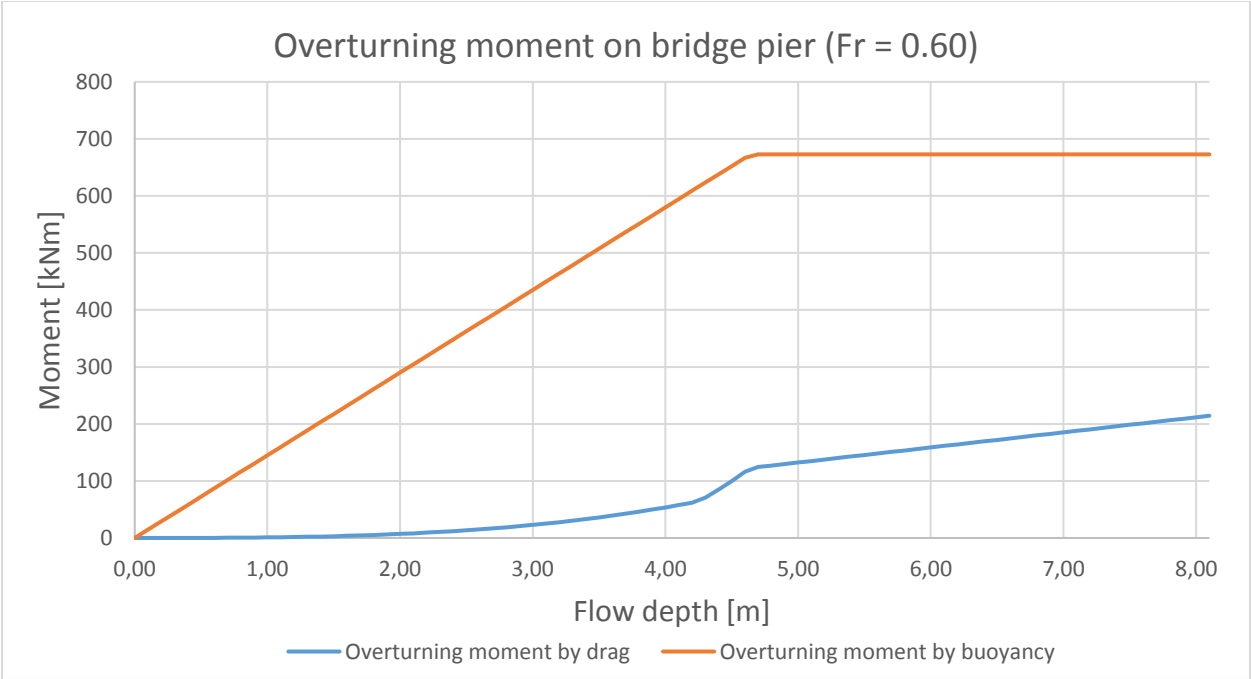

Figure 38: overturning moment on a pier without debris.

It is clear the contribution by buoyancy is largest. In the plot for overturning moment by drag force three regions can be distinguished:

- Until approximately $h_u = h_{base,atk}$ (4.25 m) the overturning moment by drag increases cubically, because both the total force and the lever arm increase linearly as the flow depth rises, as well as the velocity if the Froude number is kept constant.
- Between approximately $h_u = h_{base,atk}$ (4.25 m) and $h_u = h_b$ (4.64 m) there is a faster rise of the drag force because the cap of the pier has a higher drag coefficient.
- When $h_u > h_b$ (4.64 m) the total drag force only increases linearly because the flow velocity is increases.

3.2.2 HYDRODYNAMIC FORCES WITH DEBRIS

Estimates of the drag force against the pier are based on Wellwood and Fenwick (9) and AS5100 (7). Wellwood and Fenwick stated that a typical debris accumulation against a pier bier can be idealized as a half-cone with diameter equal to the adjacent spans and depth half the height of the pier. This corresponds to a projected frontal area of 0.5 × 9.4 m × 2.3 m = 10.8 m². Equation 2-10 is used to calculate the drag forces at varying Froude numbers. The total overturning moment is calculated according to **Error! Reference source not ound.** and is split up between the overturning moment caused by the drag force and the (unchanged) overturning moment by buoyancy. Figure 40 plots it as a function of flow depth.

$$S_{over,p,+} = F_{D,p,deb} e_{D,p,deb} + F_{B,p} L_{cg,p} \qquad \text{Equation 3-14}$$

$$F_{D,p,deb} = \frac{1}{2} C_D \rho U^2 A \text{ with } A = -\frac{1}{4} L(h_b - 2 * \min\{h_u; h_b\}) \left(\frac{2 * \min\{h_u; h_b\}}{h_b} - 1 \right) \text{ and } C_D \text{ is variable}$$

$$e_{D,p,deb} = \frac{1}{6} (h_b + 4 * \min\{h_u; h_b\}) + h_{base,udg}$$

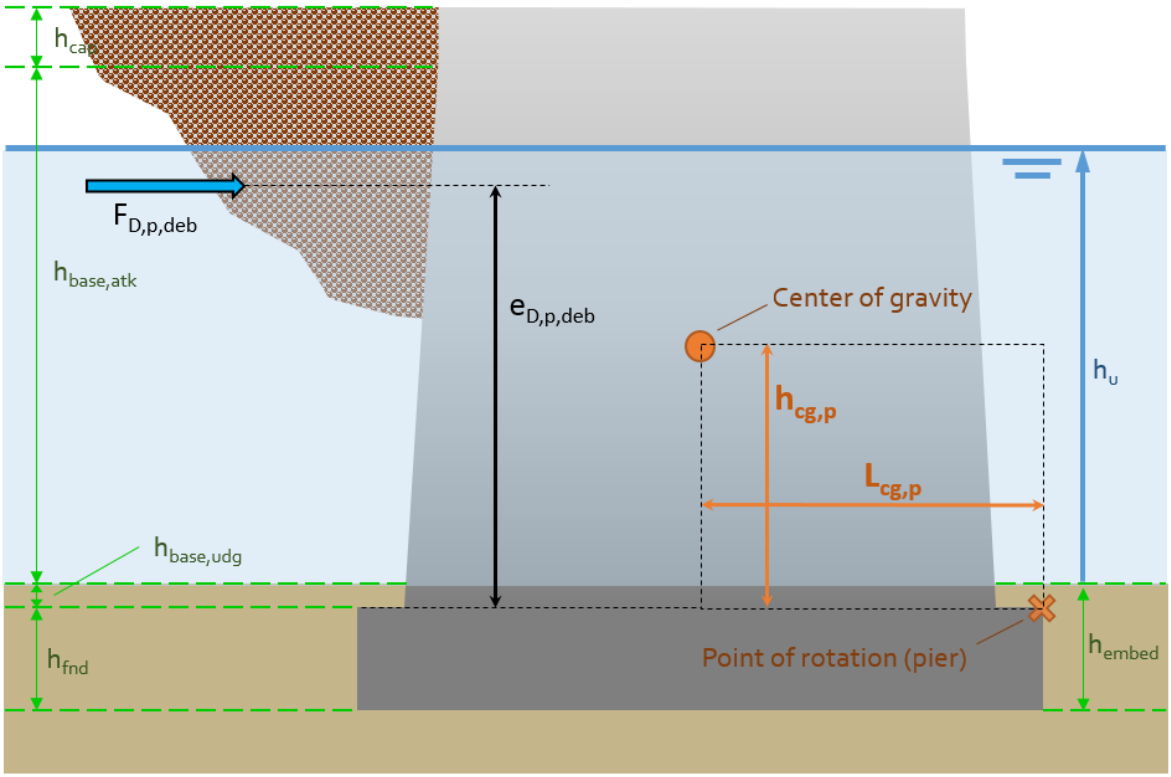

Figure 39: Drag force on the pier (with-debris scenario) with its eccentricity with respect to the point of rotation.

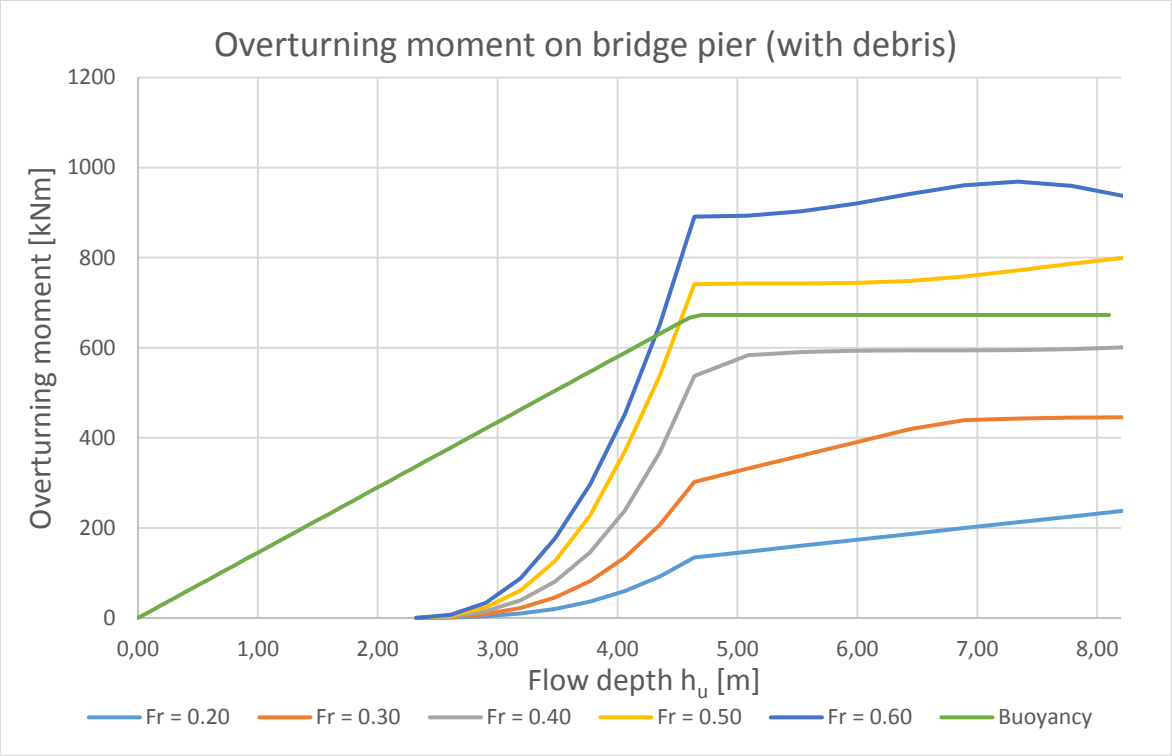

Figure 40: overturning moment on a bridge pier (with debris)

The drag caused by the still aerodynamically shaped bottom half of the pier has been neglected in Figure 40. It can be seen from the graph that the effect of drag quickly starts dominating the effect of buoyancy, in contrast to what can be seen from Figure 38. However this makes sense because the drag coefficient becomes larger (the rounded nose of the pier is covered with irregularly shaped debris) and the area attacked by flow is also much larger. The overturning moment doesn't increase much due to increased velocities, as drag coefficients actually decrease when flow velocity increases (Figure 12).

3.2.3 RESTORING FORCES

The piers stand on a spread footing foundation that is recessed some distance into the riverbed. Most likely the recess was filled up with concrete up to the level of the riverbed once the pier was properly positioned. Lateral movement is assumed to be fully restrained by the bedrock and concrete fill surrounding the foundation. Furthermore the concrete pier is assumed to be solid (not hollow) so vertical movement due to buoyancy forces is also ruled out ($F_{B,p} < F_{Z,p}$ at all times). This leaves rotation out of its recess as the only possible movement that would cause failure. Only the weight of the pier itself and strength of the connection between the foundation and the surrounding bedrock and/or concrete fill are able to provide resistance against rotation. Because the tensile strength of concrete that would've been used to fill the gaps between the foundation and the bedrock is very limited, the resistive capacity of this connection is not taken into account.

The mass of the entire pier is calculated as 85195 kg, the weight of the pier $F_{Z,p}$ = 835.8 kN. The reader is referred to Appendix A for the calculation of these numbers. There is no water pressure against the underside of the pier, as the bedrock riverbed is assumed to be impermeable to water. Figure 41 shows the straightforward restoring moment for the standalone bridge pier, according to Equation 3-15.

$$R_{over,p} = F_{Z,p} L_{cg,p} \qquad \text{Equation 3-15}$$

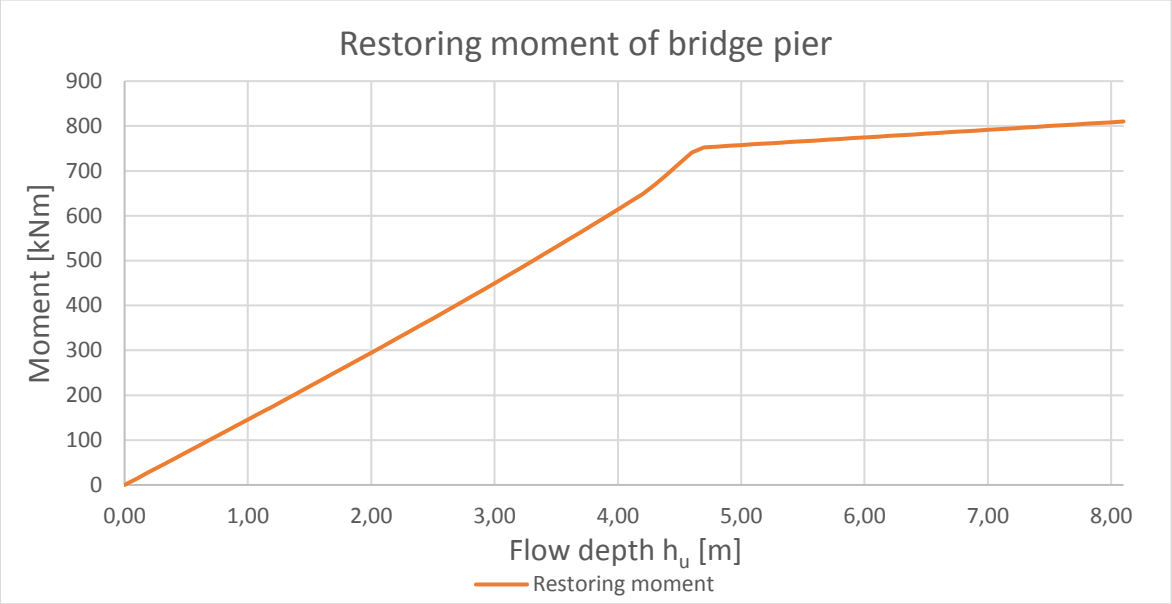

Figure 41: resistance to movement of the bridge pier

3.2.4 RESISTANCE AGAINST ROTATION

In a similar fashion to section 3.1.4, resistance against rotation is calculated according to Equation 3-16. The results of this calculation are plotted as a function of flow depth in Figure 42.

$$Z_{over,p} = R_{over,p} - S_{over,p} \qquad \text{Equation 3-16}$$

where

$Z_{over,p}$	Resistance against rotation of the pier, expressed in Nm	[Nm]
$R_{over,p}$	Restoring moment of the pier	[Nm]
$S_{over,p}$	Overturning moment of the pier	[Nm]

It may be concluded that in the without-debris case, drag forces/overturning moments against the pier are – by a large margin – not high enough to cause failure. The streamlined shape of the nose has an important role in this. Also, even with debris, the weight of the pier sufficiently high to resist the overturning moments caused by drag forces under the assumptions of drag coefficient and area of attack lined out in section 3.2.2.

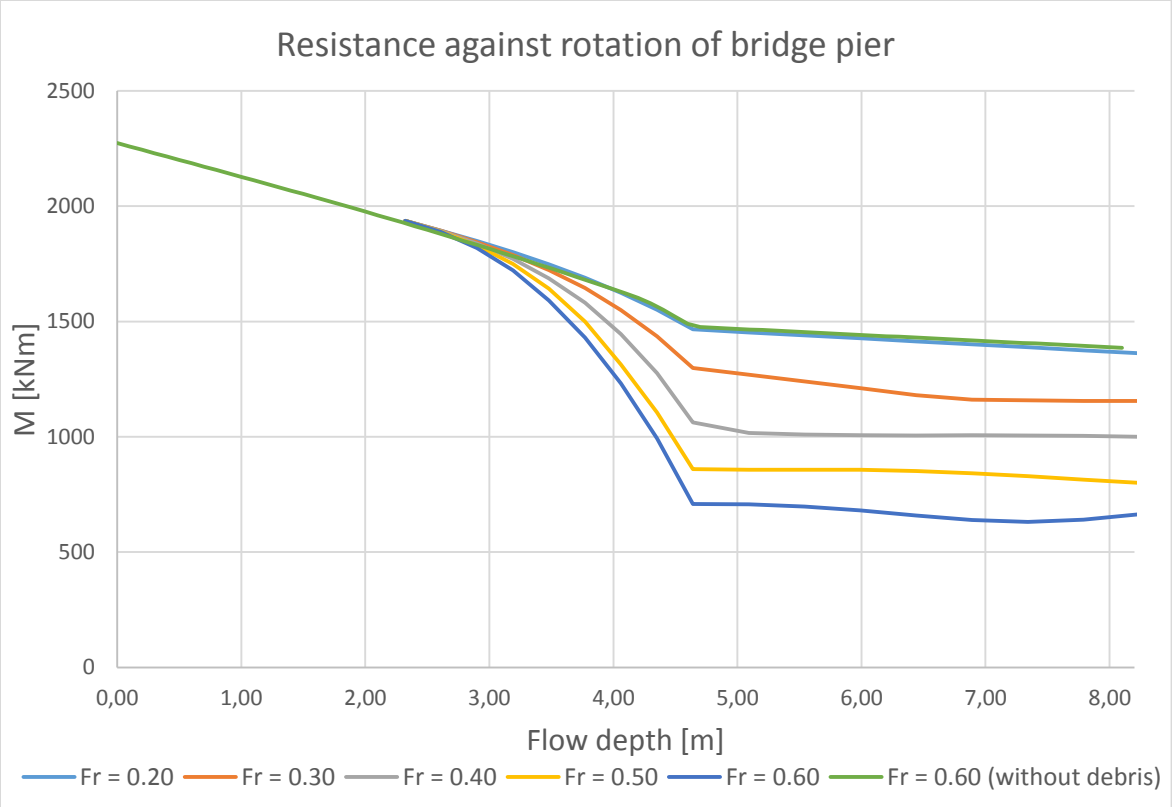

Figure 42: moments acting on bridge pier

3.3 HYPOTHESIS 2: COMBINED FAILURE

The second hypothesis assumes that the pier and two decks were connected at the moment of failure. Like the pier, only failure by rotation is considered, as the embedment into the bedrock would prevent horizontal movement. This paragraph simply adds up estimated forces on the deck and pier found in sections 3.1 and 3.2, disregarding any interaction that one component might have on the flow pattern around the other.

3.3.1 ADDING UP HYDRODYNAMIC FORCES (WITHOUT DEBRIS)

Figure 43 shows the overturning moment caused by hydraulic drag forces, hydraulic lift forces (on the decks) and buoyancy at $Fr = 0.48$ as a function of flow depth h_u, calculated according to Equation 3-17. This graph is a summation of the moment around the point of rotation at the foundation (as shown in Figure 20) of both the drag forces on the bridge pier as well as the bridge deck. From the rapidly changing overturning moment from $h_u = 4.64$ m (corresponding to the water level reaching the deck) it is clear that the drag and negative lift forces on the deck play the largest role in this failure mechanism. The jumps in the graph are caused by the discrete values of h^* for which the drag, lift and moment coefficients are known.

$$S_{over,t,-} = S_{over,p,-} + 2F_{D,d,-}e_{D,d,-} + 2\left(F_{B,d} + F_{L,d}\right)L_{cg,p} - 2M_{cg,d} \qquad \text{Equation 3-17}$$

where

$S_{over,t,-}$	Overturning moment on deck-pier system without debris	[Nm]
$S_{over,p,-}$	Overturning moment on pier without debris (Equation 3-13)	[Nm]
$F_{D,d,-}$	Drag force on the deck without debris	[N]
$e_{D,d,-}$	Vertical distance between the line of $F_{D,d,-}$ and the point of rotation	[m]
$F_{B,d}$	Buoyancy force on the deck	[N]

$F_{L,d}$	Lift force on the deck	[N]
$L_{cg,p}$	Distance between the center of gravity of the pier and the point of rotation	[m]
$M_{cg,d}$	Moment around the center of gravity of the deck	[Nm]

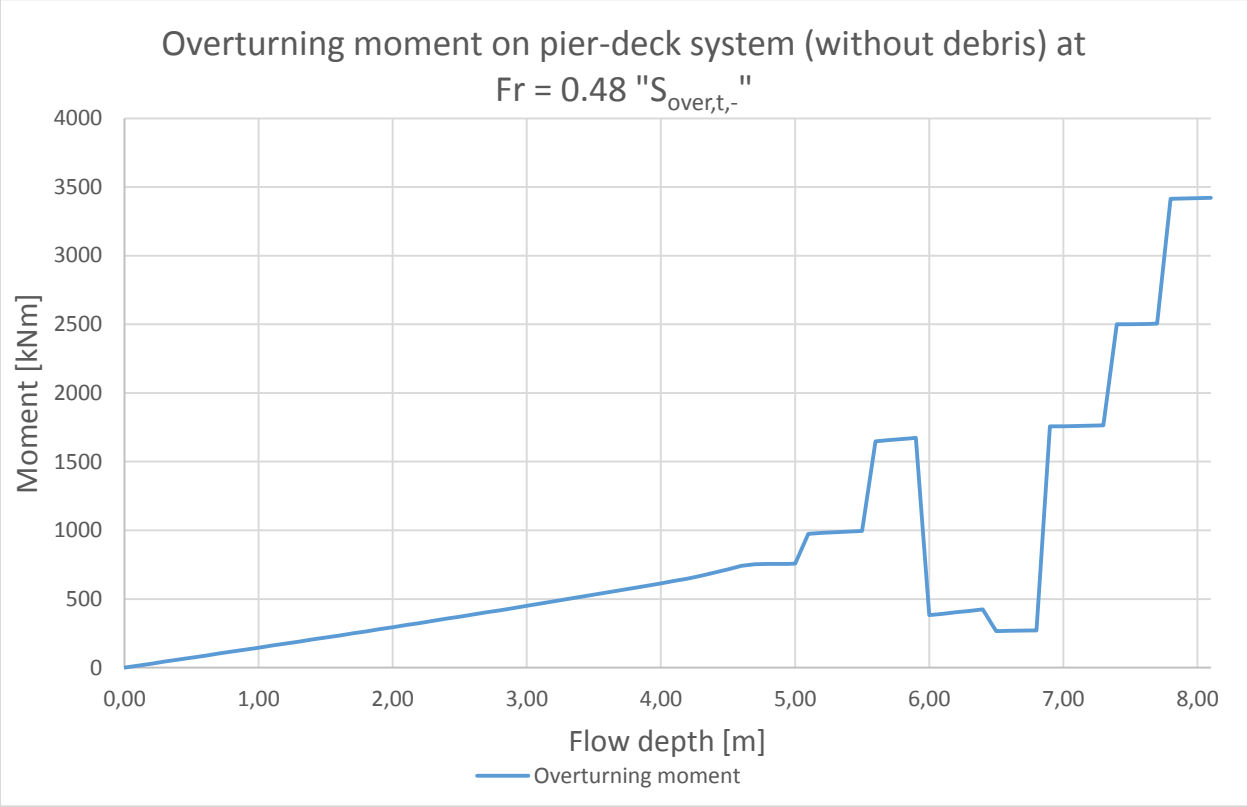

Figure 43: overturning moment on the combined deck-pier system

3.3.2 ADDING UP HYDRODYNAMIC FORCES (WITH DEBRIS)

The approach is similar to section 3.3.1. Figure 44 plots the overturning moment on the pier-deck system with debris according to Equation 3-18. The graph for $S_{over,t,+}$ has much the same shape as $S_{over,t,-}$, indicating once again that the hydrodynamic drag and lift forces on the deck are dominant.

$$S_{over,t,+} = S_{over,p,+} + 2F_{D,d,+}e_{D,d,+} + 2(F_{B,d} + F_{L,d})L_{cg,p} - 2M_{cg,d} \qquad \text{Equation 3-18}$$

where

$S_{over,t,+}$	Overturning moment on deck-pier system with debris	[Nm]
$S_{over,p,+}$	Overturning moment on pier with debris (Equation 3-14)	[N]
$e_{D,p,deb}$	Vertical distance between the line of $F_{D,p,deb}$ and the point of rotation	[m]
$F_{D,d,+}$	Drag force on the deck with debris	[N]
$e_{D,d,+}$	Vertical distance between the line of $F_{D,d,+}$ and the point of rotation. Equal to $h_{base,udg} + h_b + h_{cg,d}$	[m]
$F_{B,d}$	Buoyancy force on the deck	[N]
$F_{L,d}$	Lift force on the deck	[N]
$L_{cg,p}$	Distance between the center of gravity of the pier and the point of rotation	[m]
$M_{cg,d}$	Moment around the center of gravity of the deck	[Nm]

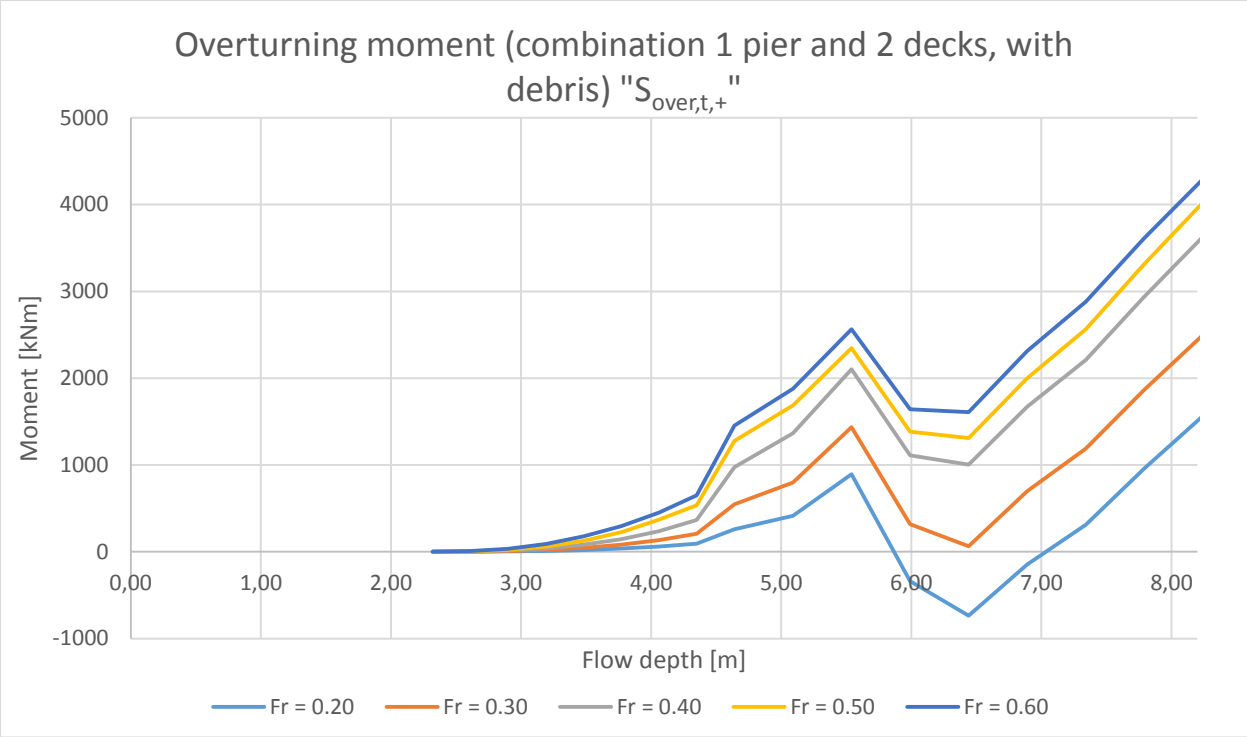

Figure 44: overturning moment on the pier-deck system with debris

3.3.3 RESTORING FORCES

Resistance against overturning is provided only by the weight of the pier and the decks, and is readily calculated according to Equation 3-19. Only failure by rotation is considered, as horizontal movement is assumed to be fully restricted.

$$R_{over,t} = (W_{pier} + 2W_{deck})L_{cg,p} \qquad \text{Equation 3-19}$$

where

W_{pier}	Weight of the pier (836 kN)	[N]
W_{deck}	Weight of the deck (606 kN)	[N]

Evaluation of the formula yields:

$$R_{over,t} = (836 + 2 * 606) * 2.72 = 5571 \text{ [kNm]}$$

3.3.4 RESISTANCE AGAINST ROTATION

Figure 45 plots the predicted $Z_{over,t}$ according to Equation 3-20. It needs to be stressed that this estimation doesn't include potential transfer of debris-buoyancy forces onto the system. While these forces may not be large, the moment arm between the debris and point is rotation is. Equation 3-20 therefore overpredicts the resistance against overturning.

$$Z_{over,t} = R_{over,t} - S_{over,t} \qquad \text{Equation 3-20}$$

where

$Z_{over,t}$	Resistance against rotation of the deck-pier system, expressed in Nm	[Nm]

$R_{over,t}$	Restoring moment of the deck-pier system	[Nm]
$S_{over,t}$	Overturning moment of the deck-pier system	[Nm]

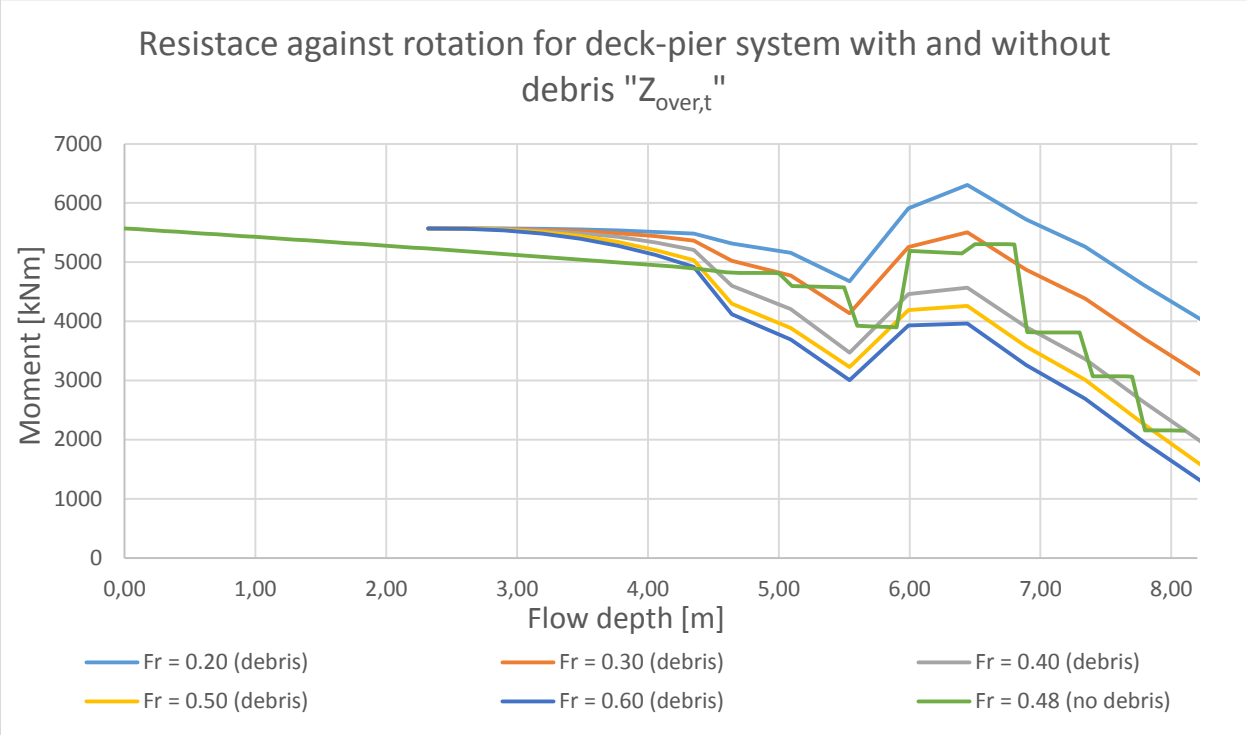

Figure 45: resistance against rotation for the deck-pier system under various conditions

3.4 SUMMARY OF PREDICTIONS

- Failure of the pier on its own, according to hypothesis 1, will not occur under any circumstance.
- Failure of the deck will occur by lateral movement due to insufficient friction provided by the elastomeric bearings
  - With debris: at h^* = 1.15 when Fr = 0.48. Failure is also possible at lower Froude numbers but then the inundation ratio needs to be higher: at h^* = 2.00 when Fr = 0.20 failure can occur.
  - Without debris: at h^* = 1.25 when Fr = 0.48. No failure when Fr = 0.20
  - The influence of the debris diminishes at Froude number increases. This makes sense as area is linear in the expression for drag force while velocity is squared.
- Failure of the combined system might occur at h_u > 8.00 m (h^* > 3.00) for very high Froude numbers, only when debris is present and when debris-buoyancy forces/moments are transferred to the system.
  - However, individual failure of the deck occurs well before these conditions can be reached.
- In these predictions, buoyancy forces from the debris are not assumed to be transferred to the bridge components, while in reality, this will happen at least partially. Because of this, resistances against movement are higher in the predictions than in reality.
- The debris will have an effect on the C_L and C_M coefficients of the bridge deck. However C_L and C_M values for the non-debris case are used even in scenarios with debris.

4 EXPERIMENTAL METHOD

The first step in being able to answer the research question of this thesis is finding out which of the two hypotheses is true and which hypothesis needs to be rejected. To do so, experiments in a flume with scale models of the bridge have been developed. A scale model deck is placed on a scale model pier – ensuring that the friction factor between the two contact surfaces is equal to the friction factor between elastomer and steel (hypothesis 1) – and exposed to a certain range of hydraulic conditions in a flume. Another scale model that has the pier and (two) decks rigidly connected (hypothesis 2) is exposed to the same range of hydraulic conditions. When of the scale model is visually observed to fail prior to the other under the same conditions, the governing failure mechanism (according to either hypothesis 1 or 2) is known. In other words, the first focus of the research is finding the governing failure mechanism of the bridge. The second step is to know the magnitude of forces acting on the bridge at the moment of failure. To this end a (component of the) scale model of the bridge is exposed to a flow whilst being monitored by load cells.

The aim of the experiments is thus twofold:

- Determining at which inundation ratio, Froude number and amount of debris the bridge fails according to both hypotheses. After completion of this stage, it is possible to discard one of the two hypotheses.
- Determination of the drag, lift and moment coefficients (C_D, C_L and C_M) of several bridge components as a function of the inundation ratio h^*, the Froude number Fr, and the amount of debris.

Because the components cannot be displaced (i.e., fail) while being restrained by a load cell which is rigidly connected to the outside environment, these tasks cannot be performed simultaneously. Two separate experimental runs (at identical conditions) must be executed. During one, the component is free to move (disconnected from the load cell) and loaded until failure. During the second run the component is restrained by the load cell that measures the forces acting on the component. By also measuring the flow velocity and the water level at the moment of failure during the 'free standing'-experiment and finding the corresponding drag, lift and moment coefficients found during the 'load cell'-experiment, the forces on the component at the time of failure are known.

4.1 SCALE MODEL

The dimensions of the available flume compared to the actual dimensions of the bridge in the field dictate the scale at which the experiments take place. In this case, the width of the flume was the limiting factor. The flume width was measured to be 770 millimeters, while the bridge had a total length of 28.2 meters in reality. A simple calculation reveals that the highest scale at which the experiments can be performed in the available flume is 1:37.

ABS (Acrylonitrile butadiene styrene) plastic is chosen as the main material for the scale model, because it is relatively easy to process ABS into the required shapes. A small amount of hardwood has also been used for the model. The scale model is made out of different components, namely the base of the pier, the pier foundation, the deck segments and the abutments (see Figure 46). Since plastic has a lower density than concrete, the material used for the bridge in reality, each component has a hollow cavity that can be filled with for example lead (density higher than concrete) sheets to achieve the correct weight. For more detailed information the reader is referred to Appendix B.

A shortcoming of the scale model is that the railings that were on the sides of the bridge are not modelled. These railings would be too weak and fragile for the experiments if scaled down to the correct size. Nevertheless, it can be assumed that the influence of the railings on the hydraulic forces on the deck as a whole is small, given that the effective area that is blocked by the railings is small. Thus omission of the railings in the

scale model is justifiable. Following this argument, the inundation ratio h^* will be calculated using s_m instead of s_f (Figure 20), for both the experiments and the field. The effect of the railings on the accumulation on debris will be discussed in section 4.3.

As mentioned the scale model consists of four different components:

- Abutment
- Foundation of the pier
- Base of the pier
- Bridge deck

In order to accommodate using the same scale model for testing both hypotheses, the components bridge deck and base of the pier as well as the base of the pier and the foundation of the pier can either be rigidly connected to each other or left separated (meaning there is no transfer of forces between those components). A 3D-schematization of the scale model showing the different components is shown in Figure 46. The way the scale model is placed into the flume is shown in Figure 47 (top-view) and Figure 48 (side-view).

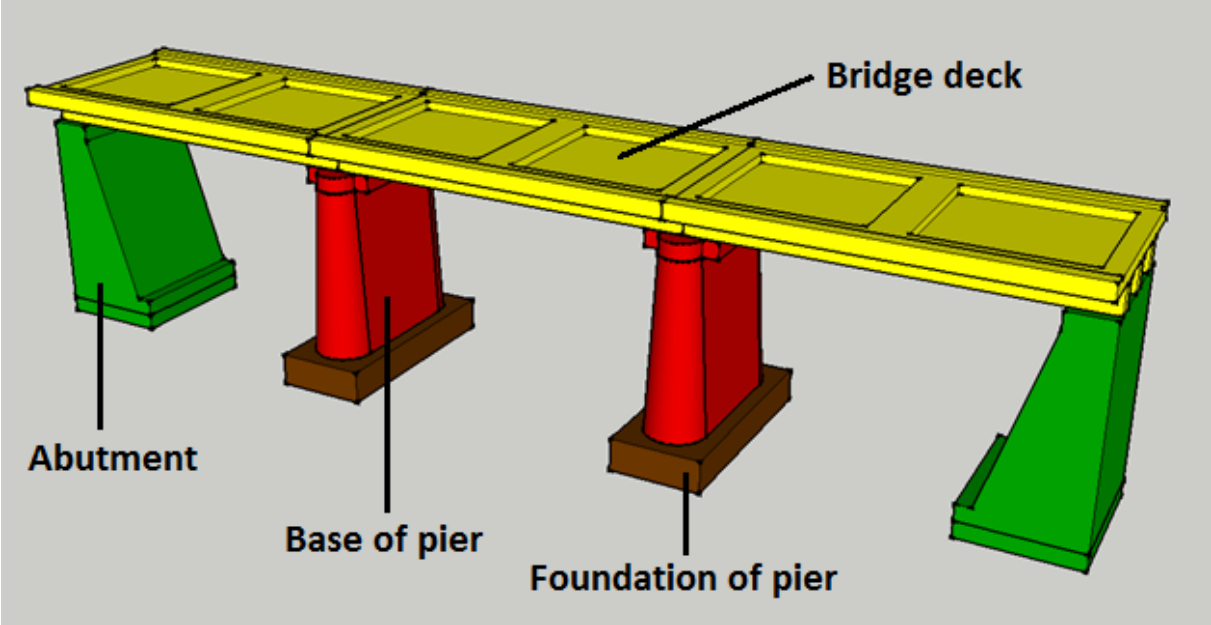

Figure 46: 3D-schematization of the scale model. The 'pits' in the deck segments are filled with lead to achieve the correct weight (Appendix B), and then covered with a plastic sheet, so that the deck surface becomes smooth.

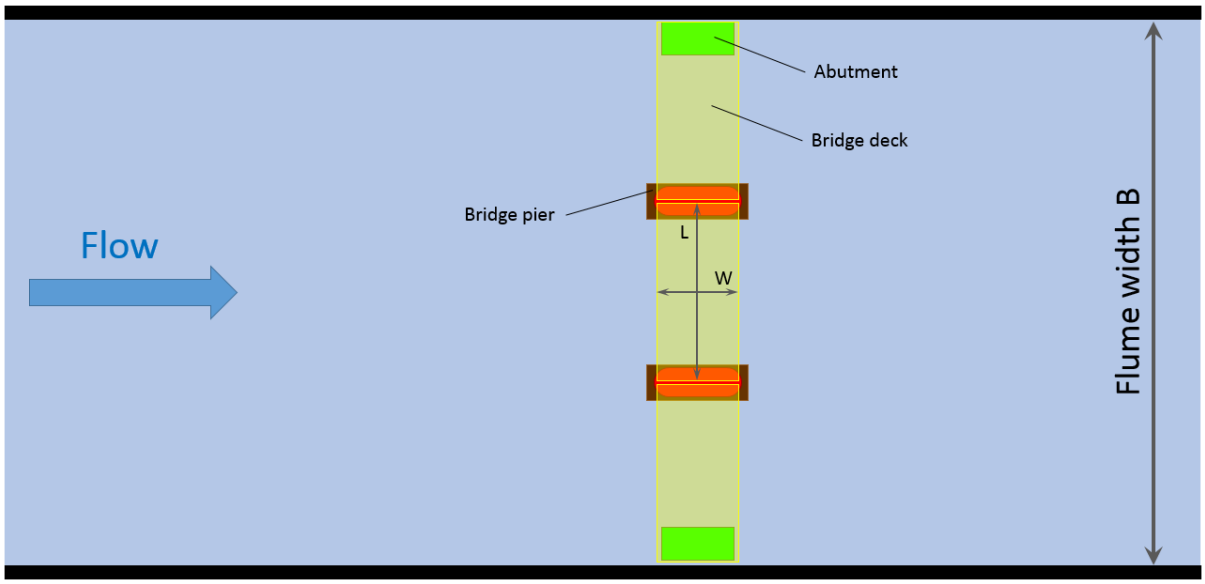

Figure 47: top-view of the bridge model in the flume.

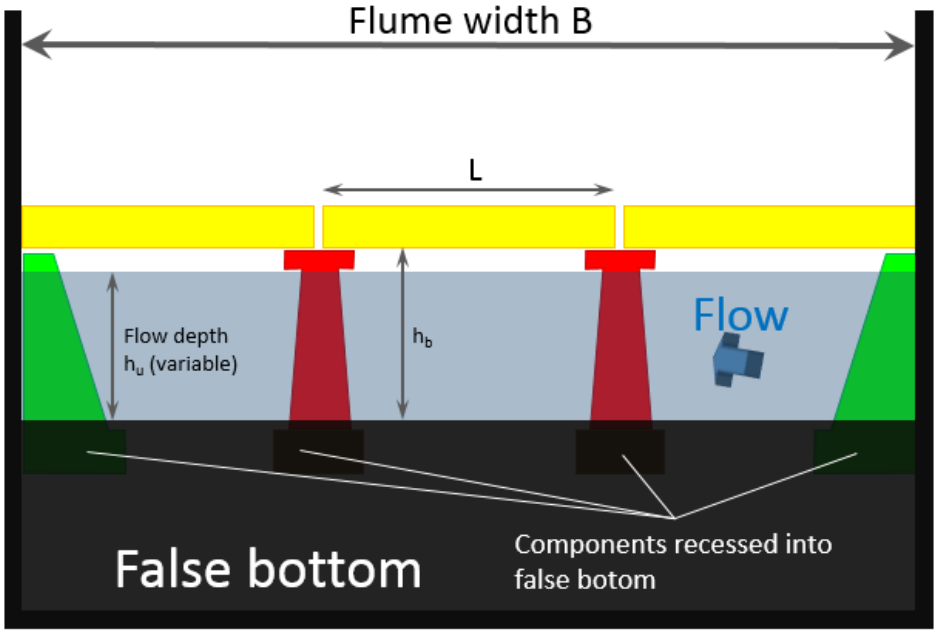

Figure 48: front-view (horizontal and vertical dimensions not to scale) of the scale model in the flume, recessed into a false bottom (see section 4.6)

If only a single component or section of the bridge were modelled it would have been possible to perform the experiments at a larger scale. However, the choice to model the entire bridge instead of just a section or using symmetry is based on the inclusion of the effects flow patterns caused by adjacent components. This way it is possible to measure, for example, potential differences between hydrodynamic forces on the middle deck segment and the side deck segments. Recreating the shapes and dimensions of the bridge as accurate as feasible with the material used instead of resorting to basic shapes also allows for more accurate reproduction of the flow field around the components. This in turn leads to more accurate results.

Skin friction is not accurately modelled by these scale models, since the surface roughness of the plastic model is much less than the surface roughness of the non-finished concrete bridge in the field. However, it is assumed that most of the horizontal forces on the bridge decks and piers are caused by form drag instead of skin friction, so this is justifiable.

4.1.1 SCALING EFFECTS

Ideally, a less than full scale experiment has geometric similarity, kinematic similarity and dynamic similarity compared to the real world scenario. Geometric similarity can easily be achieved by scaling down all dimensions of the objects by the scaling factor, according to:

$$\lambda = \frac{L_F}{L_M} \qquad \text{Equation 4-1}$$

where

λ	Scaling factor	[-]
L_F	Length of an object in the field	[m]
L_M	Length of an object in the model	[m]

It is said that the scale experiment also has kinematic similarity if the rates of displacement (for example velocity) of the objects in the field and in the model are scaled by the same scaling factor λ.

$$\lambda = \left(\frac{dx}{dt}\right)_F \Big/ \left(\frac{dx}{dt}\right)_M \qquad \text{Equation 4-2}$$

where

λ	Scaling factor	[-]
$(dx/dt)_F$	Rate of displacement of an object in the field	[m/s]
$(dx/dt)_M$	Rate of displacement of an object in the model	[m/s]

Finally, full dynamic similarity is achieved if ratios of forces acting on the model and in the field are related by the same scaling factor, in other words if Equation 4-3 is satisfied:

$$\left(\frac{F_1}{F_2}\right)_F = \left(\frac{F_1}{F_2}\right)_M \qquad \text{Equation 4-3}$$

where

$(F_1/F_2)_F$	Ratio of F_1 over F_2 in the field	[N]
$(F_1/F_2)_M$	Ratio of F_1 over F_2 in the model	[N]

Unfortunately, it is physically impossible to achieve all these three similarities simultaneously when conducting less than full scale experiments. This is due to the fact that in the expressions of some forces, geometric quantities and kinematic quantities are raised to different powers. As an example, the expression for an important force in the research, the drag force, reads: $F_D = ½\ \rho\ A\ U^2$. When an experiment is conducted at a scale λ, the drag force in the model would be:

$$F_{D,model} = \frac{1}{2} * \rho * \frac{L}{\lambda} * \frac{L}{\lambda} * \left(\frac{U}{\lambda}\right)^2 = \frac{\rho L^2 U^2}{2\lambda^4}\,[N] \qquad \text{Equation 4-4}$$

$$F_{D,field} = \frac{1}{2} * \rho * L * L * U^2 = \frac{\rho L^2 U^2}{2}\,[N] \qquad \text{Equation 4-5}$$

When this is compared to for example the gravity force on $F_Z = \rho\, V\, g$

$$F_{G,model} = \rho * \frac{L}{\lambda} * \frac{L}{\lambda} * \frac{L}{\lambda} * g = \frac{\rho g L^3}{\lambda^3}\,[N] \qquad \text{Equation 4-6}$$

$$F_{G,field} = \rho * L * L * L * g = \rho g L^3\,[N] \qquad \text{Equation 4-7}$$

According to Equation 4-3, dynamic similarity is achieved if

$$\left(\frac{F_D}{F_G}\right)_{field} = \left(\frac{F_D}{F_G}\right)_{model} \qquad \text{Equation 4-8}$$

When Equation 4-8 is evaluated:

$$\frac{\rho L^2 U^2 / 2}{\rho g L^3} = \frac{U^2}{2gL} \quad \neq \quad \frac{\rho L^2 U^2 / 2\lambda^4}{\rho g L^3 / \lambda^3} = \frac{U^2}{2gL\lambda} \qquad \text{Equation 4-9}$$

Equation 4-8 is <u>not</u> satisfied so there is no dynamic similarity between drag forces and gravity forces in this case.

An assessment must be made of which ratio of forces is most important in the experiment, i.e. which dynamic similarity is most important, and which aspects of dynamic similarity may be neglected. Each ratio of forces can be expressed as a certain dimensionless number. According to the Buckingham-π theorem, depending on the amount of physical dimensions k involved in a set of equations with n physical variables, $p = n - k$ dimensionless parameters can be constructed.

From previously carried out experiments in open channel flow, it is clear that for these experiments the Froude number is the dimensionless number that is most important to be equal in both the real world scenario and the scale experiments. The Froude number Fr is calculated by:

$$Fr = U / \sqrt{gd} \qquad \text{Equation 4-10}$$

where

Fr	Froude number	[-]
U	Flow velocity	[m/s]
g	Gravitational acceleration (9.81 m/s^2)	[m/s^2]
d	Flow depth (also denoted by h_u)	[m]

This dimensionless number expresses the ratio between inertia and gravity forces. It is inevitable that certain scaling effects will occur. These scaling effects stem from the unavoidable dynamic dissimilarity. Is it important to investigate the impact these scaling effects can have on the results of the experiments. Especially the Reynolds number and its effect on C_D is of importance. The Reynolds number is the ratio of inertia force to viscous force and can be calculated using Equation 4-11**Error! Reference source not found.**.

$$Re = {}^{\rho UL}/_{\mu} = {}^{UL}/_{\nu}$$ Equation 4-11

where

Re	Reynolds number	[-]
U	Flow velocity	[m/s]
L	Characteristic length scale	[m]
ρ	Fluid density (1000 kg/m^3 for water)	[kg/m^3]
μ	Fluid dynamic viscosity (approximately 0.001 Ns/m^2 for water)	[Ns/m^2]
ν	Fluid kinematic viscosity (approximately 1 • 10^{-6} m^2/s for water)	[m^2/s]

Figure 49 shows a graph of measured drag coefficients for a smooth sphere as a function of Reynolds number. At low Reynolds numbers, flow around the sphere is laminar, with high drag forces. In the turbulent regime, the drag coefficient is more or less constant. At $Re = 2.5 \cdot 10^5$ a drop in drag coefficient occurs as a result of a transition from a laminar boundary layer to a turbulent boundary layer (25). For the rounded rectangular shape of the bridge pier under investigation, this sudden change in drag coefficient is not present, see Figure 50.

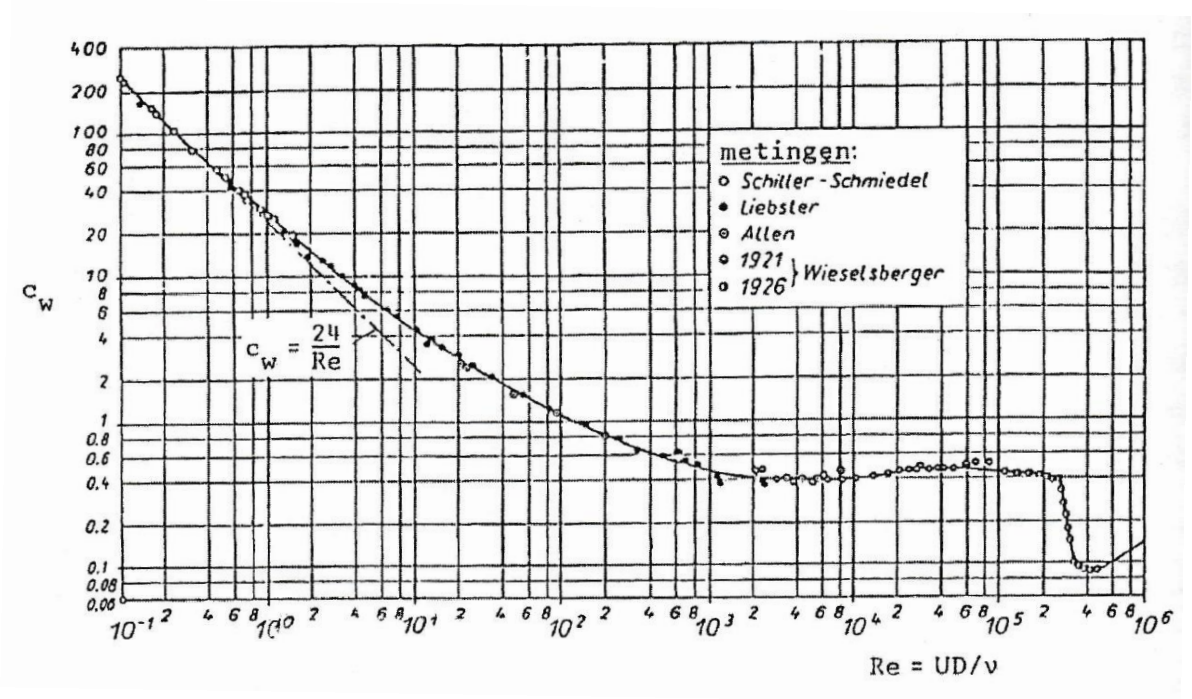

Figure 49: Drag coefficient for a sphere are a function of Reynolds number (from Battjes, 2002) (25)

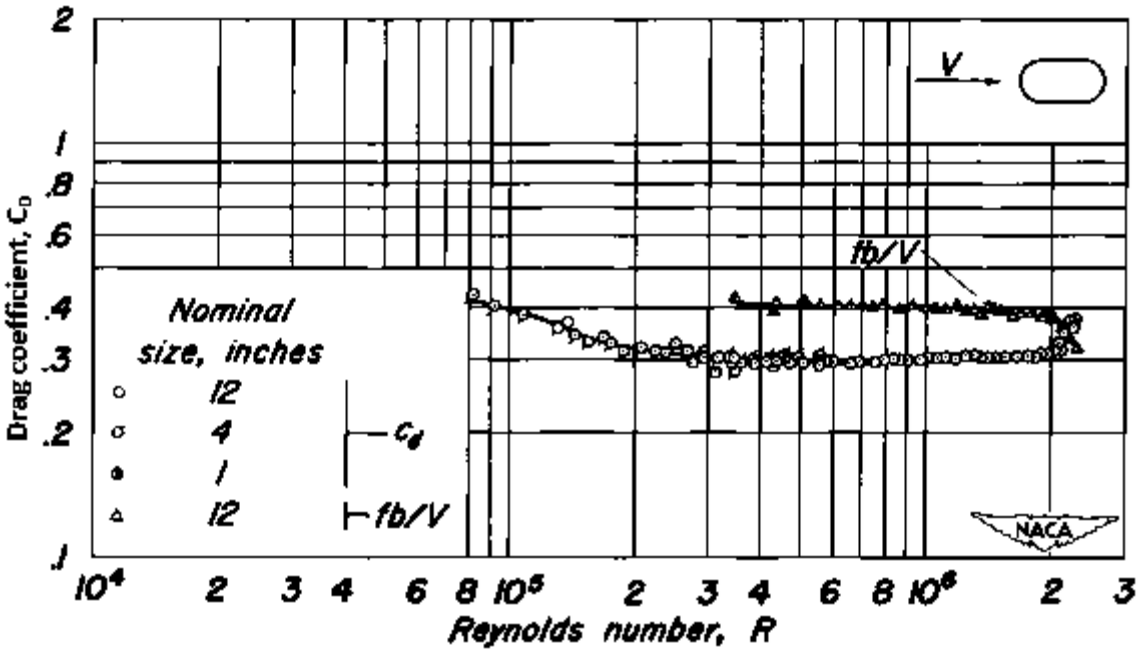

Figure 50: drag coefficient for a rounded rectangle (rounded data points) as a function of Reynolds number (from Delany and Sorenson, 1953) (26)

Figure 51 shows a graph of the Reynolds number for flow around the base of the pier, as a function of Froude number. Table 6 shows the assumed length scale and flow depth used for this plot. Comparing the plot with Figure 50 it can be seen that drag coefficient doesn't change significantly across the range of Reynolds numbers. Therefore is can be said that scaling effects due to different Reynolds numbers will be small and it is justifiable not to correct for this dynamic dissimilarity.

	Field	Model
Length scale L	1.28 m	3.5 cm
Flow depth h_u	5.18 m	14.0 cm

Table 6: Parameters for calculation of Reynolds number at field scale and at model scale

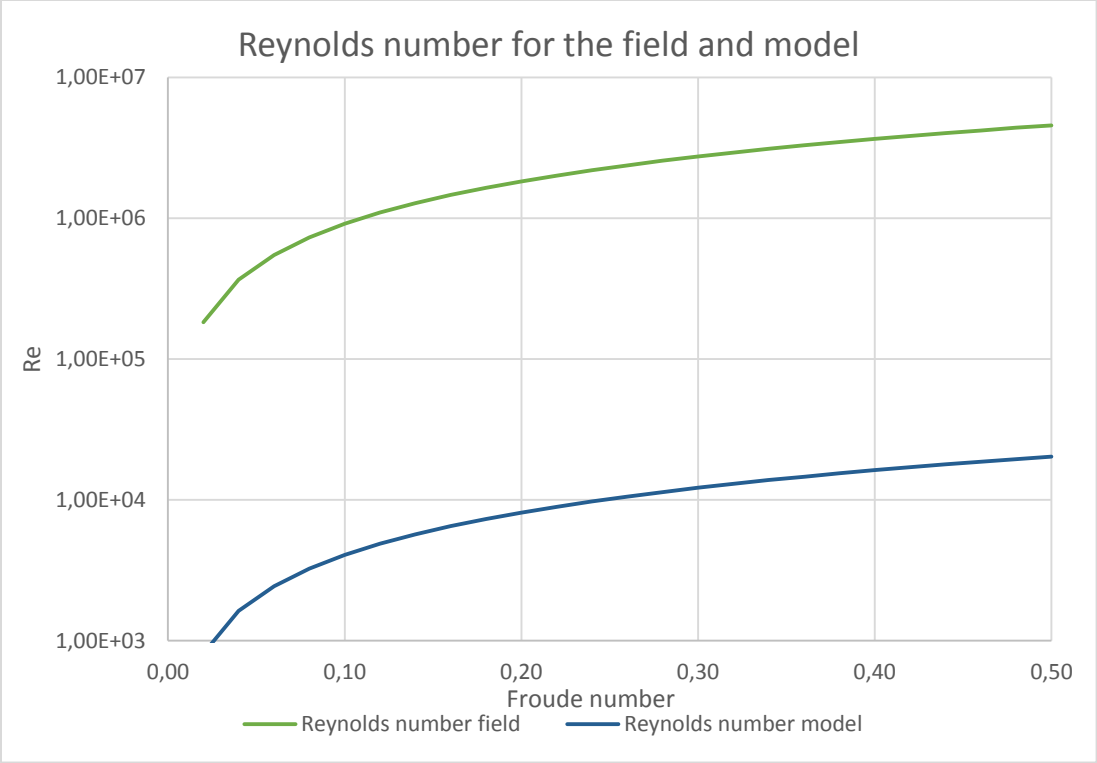

Figure 51: Reynolds number for the field and model (L is taken as the average width of the pier)

4.2 FLUME & PUMP

A recirculating flume is used for the experiments. The advantage of such a flume is that the flow depth and flow velocity can be easily be adjusted independently of each other. Once a certain amount of water has entered the flume (up to the desired flow depth), the inflow valves are shut and the water cannot leave the now closed system. A pump is then used to initiate and maintain the flow by recirculating water from the downstream end of the flume back to the upstream end. The flow depth can be altered by letting more water into the system or draining water from the system. The flow velocity can be regulated by setting the power and thus the discharge of the pump to the desired value using the simple discharge formula:

$$Q = B * h_u * U \qquad \text{Equation 4-12}$$

where		
Q	Discharge	[m^3/s]
B	Width of the flume	[m]
h_u	Flow depth	[m]
U	Depth-averaged flow velocity	[m]

The installed pump has a maximum discharge of approximately 400 L/s.

4.3 DEBRIS

To simulate woody debris such as logs, sticks and twigs, circular wooden sticks are glued together to form various shapes. Each stick has a diameter of approximately 1.0 cm and varying lengths. The density of the wood saturated with water ρ_{debris} is approximately 0.70 g/cm^3. The wooden sticks are stacked in such a way that the percentage of voids is minimized, i.e. in the shape shown in Figure 52. In nature, the stacking of the logs will

not be like this, however there will be many different sizes of logs and twigs intertwined. It is assumed that the structure used in the experiment and the natural structure of a debris accumulation have about the same volumetric ratio of voids to solid material.

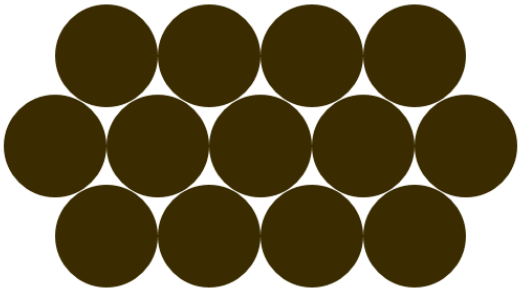

Figure 52: structure of the debris

Railings which were present on the bridge are omitted in the scale model. As discussed in section 4.1 this is justifiable as the drag force induced by the railings would not have been significant compared to the total drag force. However, the railings would be significant in their ability to catch debris. This is why the simulated debris extends above the bridge deck. Photos of the shapes used for the deck are shown in Figure 53. Shape 1 is the assumed geometry of a debris accumulation in its early stages (before it attains the final 'wedge'-form of Figure 24) and acts as the control. Shape 2 is made to investigate the effect of extension of the debris deeper into the flow. Shape 3 is similar to shape 1, but has been altered to have cutouts in the front. The shapes are held in place by fishing line wrapped around the shape and the deck. This method makes it so that not only lateral drag forces are transferred to the deck, but vertical forces (buoyancy, weight and potentially lift) as well. This is assumed to be realistic as in the field, the debris forms an interconnected matrix that must've been lodged under the deck. See Table 10 in section 5.5 for more details on the debris lodged against the deck.

Figure 53: Side views of debris shape 1 (left) and debris shape 2 (right). Shape 3 (not shown here) is identical to shape 1, except it has cutouts in the front.

The five pieces of simulated debris for the pier are shown in Figure 54. Each shape is larger than the previous, to simulate growth of the accumulations and discover what the critical volume will be. The shapes are based upon the previously carried out research by Jempson (2), who also used semi-cone shapes. During the experiments these shapes will be held into place at the top of the pier by fishing wire, otherwise the debris will float away. Again, this is assumed to be realistic as the debris that is wrapped around the pier and/or stuck under the cap will be intertwined with the debris that sticks out. See Table 11 in section 5.7 for full details on debris lodged against the pier in the experiments.

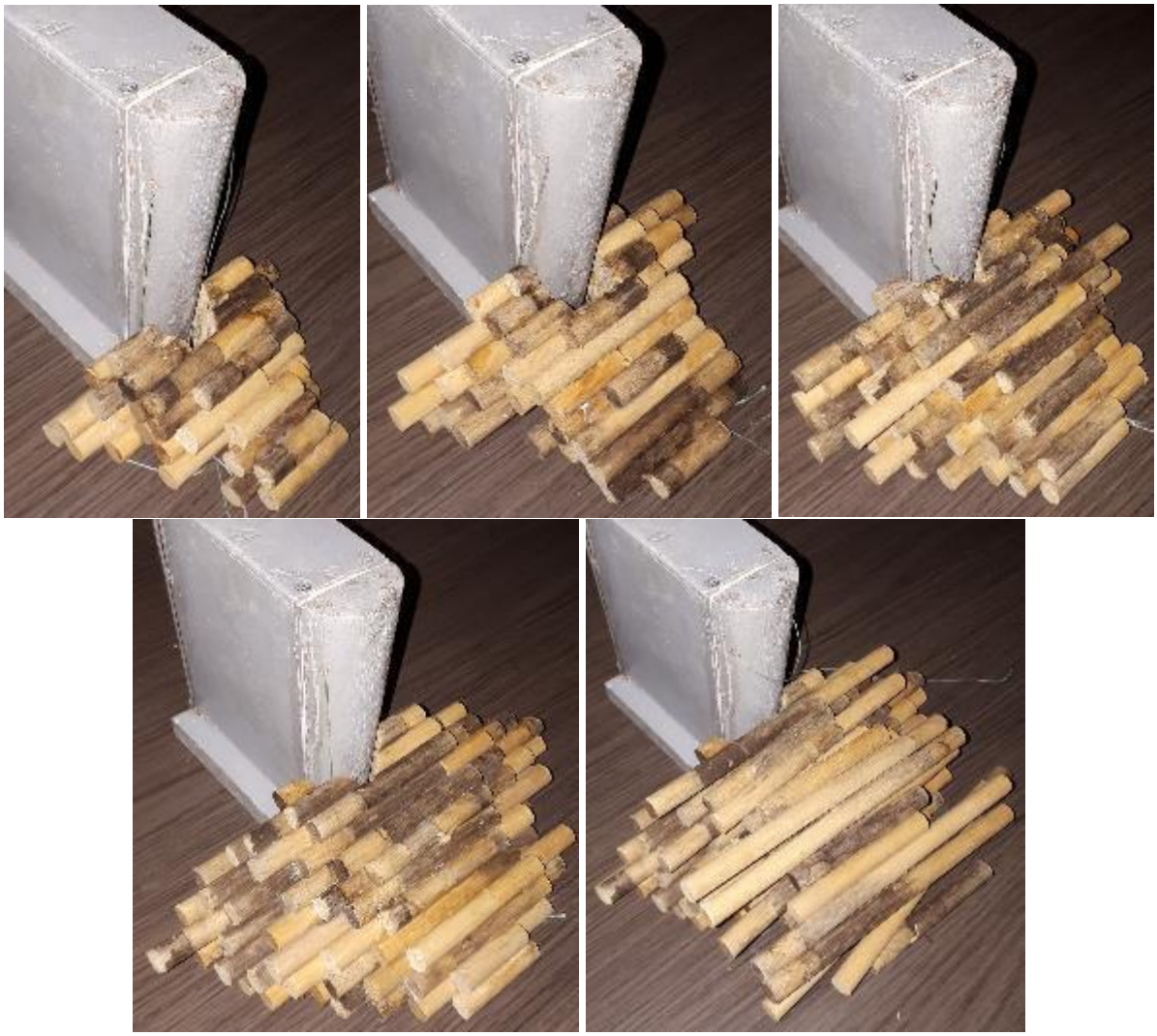

Figure 54: debris shapes (from left to right, top to bottom): S, M, L, XL, XXL. For visibility, the pier is placed up-side down and without foundation.

4.4 WATER LEVEL AND FLOW VELOCITY

The two most important characteristics of the flow to record for the experiments are the flow depth and the flow velocity. The flow depth will be measured at a distance of approximately half the width of the bridge deck in front of the bridge deck. Measurement of the flow depth will be done visually using a measuring tape stuck to the transparent side of the flume. The flow velocity is measured by an electromagnetic flow sensor (EMS) which is submerged into the flow. The EMS will serve mainly to measure local velocity (disturbances), as the depth-averaged velocity can be easily calculated using Equation 4-12. The discharge Q is measured using clamp-on ultrasonic flow meters.

4.5 LOAD CELL

Two separate load cells are used for this experiment. One is a 3-dimensional load cell capable of measuring forces in the X-, Y- and Z-direction of the type "K3D120" (rated load 500 N) by manufacturer ME-Meßsysteme GmbH. The other load cell used is a "TD110a" (rated load 50 Nm), also manufactured by ME-Meßsysteme GmbH, capable of measuring torques around a single axis.

These two load cells are connected in series to each other. The stator of the 3-dimensional load cell is bolted to a stiff plate which is seated in a clamp that is height-adjustable. The measuring platform of the 3D load cell is then connected to the stator of the torque-measuring load cell by means of a custom made adapter made from stiff material. The transfer of forces from the model to the measuring platform of the torque-measuring load cell is accomplished by another stiff connector. This connector must ideally be shaped in such a way that it disturbs the flow pattern as little as possible and produces as little extra drag as possible. Moreover, the connections between the model component and the connector as well as the load cell and the connector need to be full, moment-resisting, connections. A photo of the rig is shown in Figure 55.

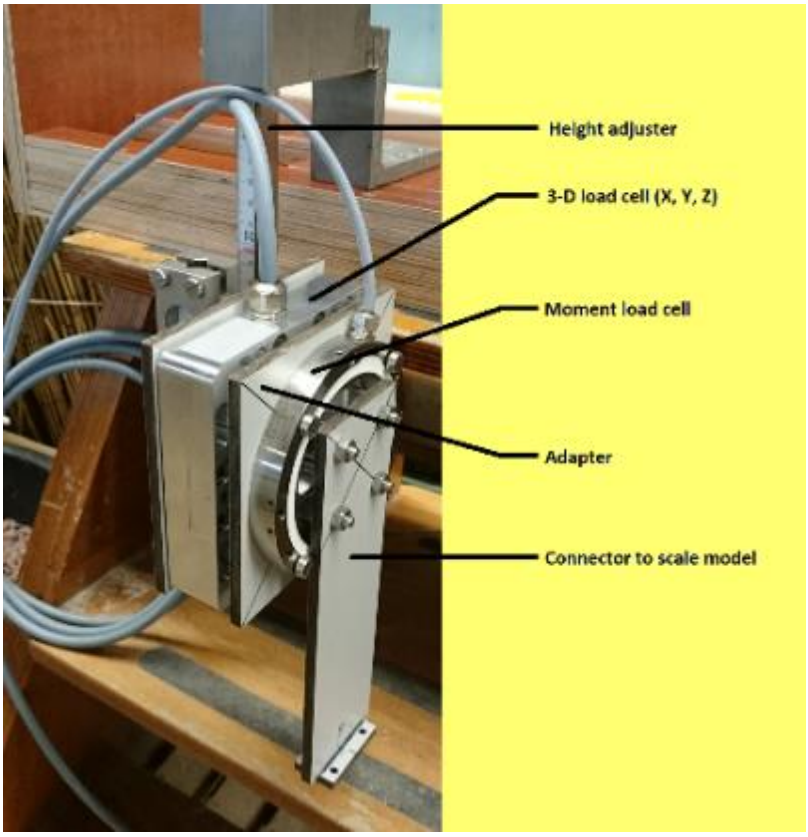

Figure 55: the load cells used for the experiment

The magnitude of the drag forces F_D can be measured directly from the measured horizontal force F_H, which is positive in the direction of the flow, according to Equation 4-13:

$$F_D = F_H \qquad \text{Equation 4-13}$$

where

F_D	Drag force	[N]
F_H	Horizontal force readout by the load cell (positive when a downstream force is applied)	[N]

During the experiment it will not be possible to measure the percentage of submergence of the scale model accurately. Therefore it is only possible to calculate the combined action of the lift and buoyancy forces acting on the model, according to Equation 4-14. This equation is only valid in case the output signal of the vertical load is set to 0 when no component is attached to it (that is, the situation shown in Figure 55).

$$F_L + F_B = -F_V + W_{model} + W_{debris}$$ Equation 4-14

where

F_L	Lift force (positive upward)	[N]
F_B	Buoyancy force (positive upward)	[N]
F_V	Vertical force readout by the load cell (positive when a downward force is applied)	[N]
W_{model}	Weight of the component(s) of the scale model	[N]
W_{debris}	Weight of the debris (if present)	[N]

The moment that is measured by the load cell needs to be corrected because it also includes the lever arm between the center of the load cell and the center of gravity of the model. The quantity of interest is M_{cg}. M_{cg} is the torque exerted on the model caused by the eccentricities of the drag and/or lift forces with respect to the center of gravity of the model. With the current experimental setup is not possible to determine the magnitude of the eccentricities, i.e. where the line of action of the total of the drag and lift forces is.

$$M_{cg} = M - F_D * e_{lc}$$ Equation 4-15

where

M_{cg}	Moment acting on a component, measured around its center of gravity (positive counterclockwise)	[N]
M	Moment readout by the load cell (positive when a counterclockwise moment is applied)	[N]
F_D	Drag force	[N]
e_{lc}	Moment arm between the center of gravity of the component(s) and the center of the load cell	[N]

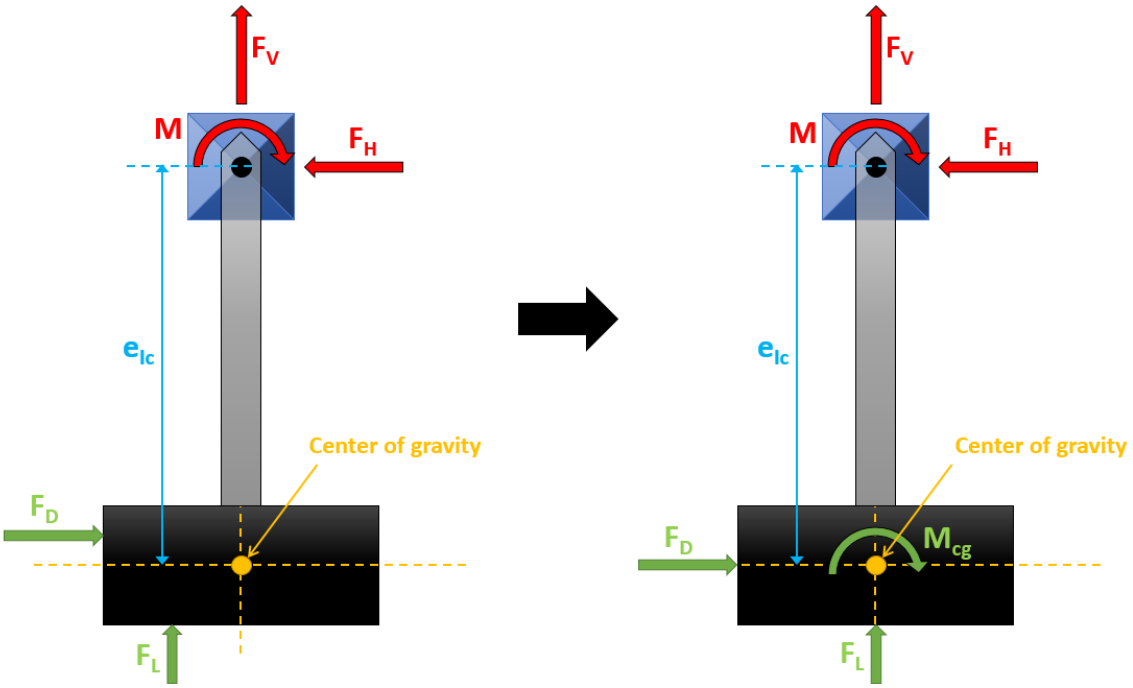

Figure 56: Free-body diagram of a scale model component, showing the eccentric drag and lift forces shifted under addition of a moment M_{cg}. The forces on the model remain equivalent. (F_Z and F_B not shown)

4.6 FALSE BOTTOM

The foundation of the scale model needs to be embedded in the bottom of the flume just like the foundation of the real pier was recessed into the riverbed. However, it is not possible to cut into the bottom of the actual flume without damaging it. For this reason a false bottom out of wood is constructed and placed into the flume. This false bottom is made to be just as wide as the inner width of the flume, save for some millimeters to allow for expansion of the wood when it becomes submerged. The hollow construction is weighed down with lead blocks so it will not move along the flume or float. Any entrapped air is allowed to escape through an opening in the back of the construction. See Figure 57.

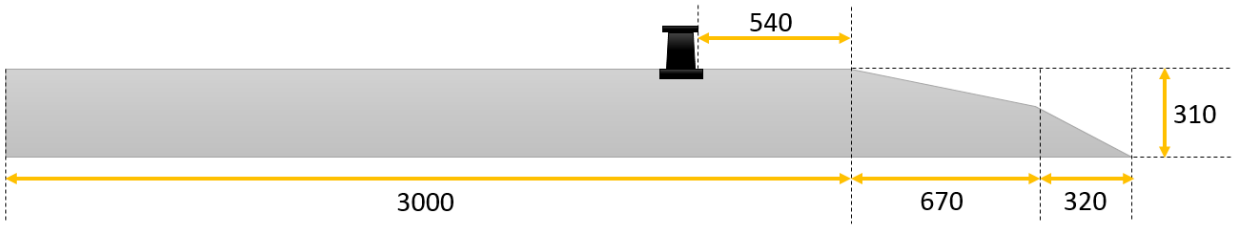

Figure 57: false bottom with dimensions in millimeters. Size of the bridge model (in black) is not to scale.

The flow at the most downstream point of the false bottom may be supercritical in some of the experiments. If there is a free overflow at that point, the free surface above the false bottom may be curved. To prevent any effect of the curved free surface, the false bottom extends sufficiently far beyond the position of the scale model, so that the scale model can be placed out of the area where a curved free surface can be present.

The entire top side of the false bottom is coated with gravel with a D_{50} of approximately 4 mm. The layer is approximately 10 mm thick. The goal of this layer is twofold:

- Upstream of the scale model it serves to add increased turbulence to the flow
- Downstream of the scale model it aims to mimic the roughness of the riverbed so that in the event of a collapse, the scale model components will not be washed away over a smooth wood surface. Instead, the post-failure position and orientation of the model components might be more similar to that of the real bridge.

4.7 EXPERIMENTAL SETUP

Each experiment is given a unique name composed in the following manner:

H#- X- Xx- ##,#- #,##- X.(#)

'H1' (hypothesis 1) or 'H2' (hypothesis 2)
'D' (deck) or 'P' (pier) or 'T' (total)
'Lc' (load cell) or 'Fs' (free standing)
h_u of the run, for example 16,0
Fr of the run, for example 0,40
'N' (no debris) or 'Y.#' (debris) where # is the debris shape

An 'H1'-experiment is carried out in order to test hypothesis 1 (failure in parts), while an 'H2'-experiment is done to learn more about the second hypothesis (failure as a whole). The second part of the expression indicates which component of the bridge is being investigated, either D(eck), P(ier) or (T)otal. The third part of the expression specifies whether the aforementioned component is connected to the load cell or not. The following digits show the flow conditions, namely water depth and Froude number. The last part of the name says whether the experiment was conducted with debris, and if so, what type.

As an example, an experimental run coded as 'H1-P-LC-14,0-0,48-Y.L' concerns a test where the forces on only the pier with the 'L'-type of debris attached are recorded by the load cell at the conditions h_u = 14.0 cm and Fr = 0.48.

Interconnections between components

When two components of the scale model are separated from each other, this is done to make sure there is no transfer of forces from the component that is attached to the load cell to other components of the model. However, to keep the flow pattern around the model identical, the components that are separated will still be placed in the flume at their usual positions relative to other components, while keeping the height of the gap that is created as small as possible.

Rigid connections between the components of the scale model are realized using multiple screws. The base of the pier has drilled holes with screw thread on the top and bottom. The foundation attaches to the bottom of the base and the deck to the top. The advantage of using screws lies in the fact that the connection is not permanent, but still tight enough to establish a moment-resisting connection.

The term scaled connection is used to describe a connection between components identical to that of the real bridge, yet appropriately scaled down in strength to be used in the experiments. In practice this means that the 'connection' between the foundation and the false bottom does not exist, as any tensile strength of the concrete fill around the foundation is neglected. In section 3.1.3 it was discovered that the frictional resistance of the bearing is governing. Therefore the connection between the base of the pier and the deck will also be based on friction. Two surfaces that mimic the friction coefficient of rubber on steel (μ = 0.25) need to be found.

The following paragraphs explain the experimental setup of the different experiments with the help of sketches and schematics.

4.7.1 Experiment: H1-D-Lc

This experiment is part of a series to test hypothesis 1 (failure in parts). Only the bridge deck is connected to the load cell, meaning that only the hydrodynamic forces exerted by the flow on the bridge deck will be measured.

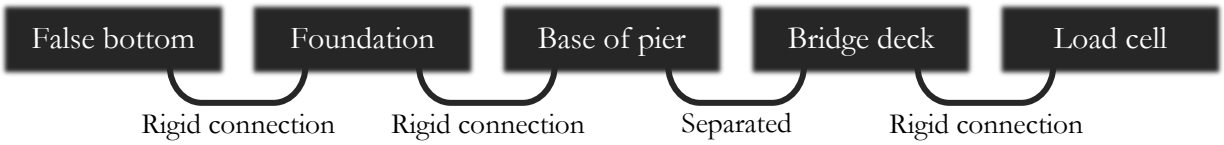

Figure 58: sketch and schematic for experiment H1-D-Lc

4.7.2 Experiment: H1-D-Fs

The counterpart to experiment H1-D-Lc, the bridge deck will now be loaded until failure. Using the data collected from experiment H1-D-Lc, it is possible to know the forces acting on the bridge deck at the moment of failure.

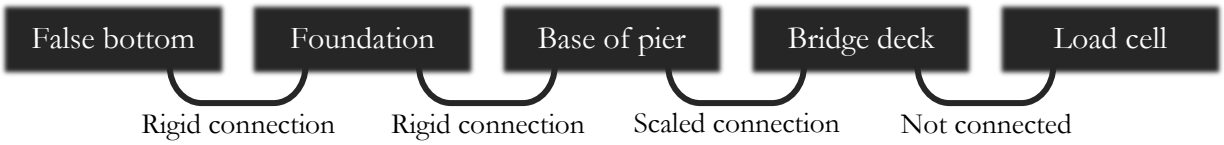

Figure 59: sketch and schematic for experiment H1-D-Fs

4.7.3 EXPERIMENT: H1-P-LC

In this experiment the bridge deck is removed, because following the first hypothesis, the deck has already failed before the pier fails. The purpose here is to measure the forces exerted by the flow on the bridge pier only. To ensure that there is no transfer of forces from the pier to the false bottom, the foundation is disconnected from the base. This is allowed considering the foundation is normally below the surface, it isn't exposed to the flow and therefore doesn't contribute to the drag forces. The measured lift forces and moments need to be corrected to compensate for the missing weight of the foundation.

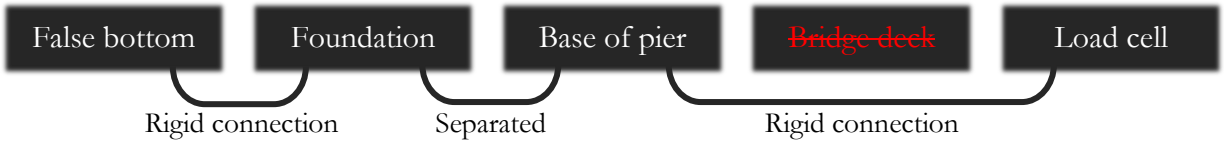

Figure 60: sketch and schematic for experiment H1-P-Lc

4.7.4 EXPERIMENT: H1-P-FS

Now the load cell is disconnected from the bridge pier, so as not to restrain its movement. The foundation is reattached, placed into a recess in the false bottom and held in place by its self-weight only. The recess in the false bottom is slightly oversized, to facilitate rotation of the pier out of the recess.

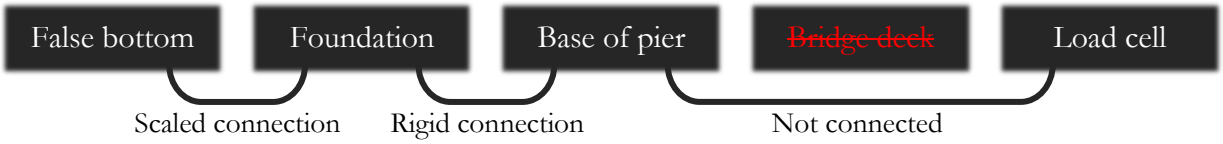

Figure 61: sketch and schematic for experiment H1-P-Fs

4.7.5 EXPERIMENT: H2-T-LC

The second hypothesis states that the bridge pier and the bridge deck have collapsed as a whole. To ensure this will indeed happen, two bridge decks and the base of one pier are rigidly connected at all times during this experiment. As in experiment H1-P-Lc, the foundation is disconnected from the base so there is no transfer of forces towards to false bottom.

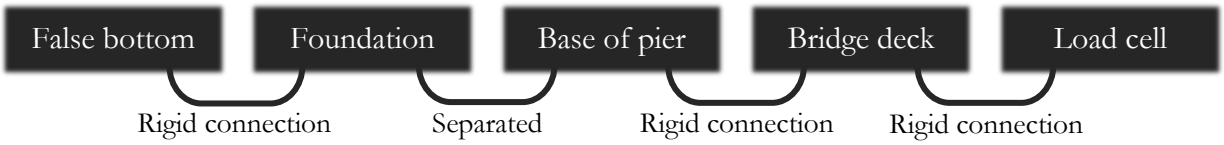

Figure 62: sketch and schematic for experiment H2-T-Lc

4.7.6 EXPERIMENT: H2-T-FS

The load cell is disconnected and the foundation is reattached. The combination of decks and pier is loaded until failure.

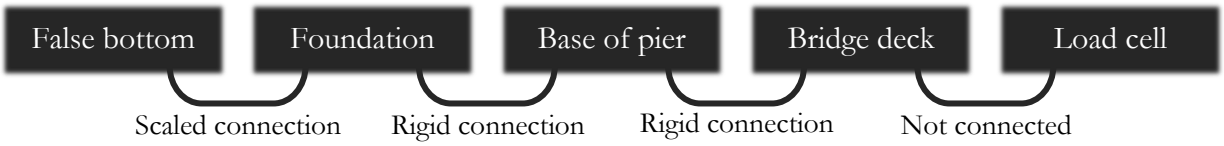

Figure 63: sketch and schematic for experiment H2-T-Fs

4.7.7 EXPERIMENT: DEBRIS

The load cell experiments (H1-T-Lc, H1-P-Lc and H2-T-Lc) are repeated, but with the different pieces of simulated debris described in section 4.3 attached. The measurements of forces when debris is added are then compared to the data without debris previously collected.

5 EXPERIMENTAL RESULTS

This chapter presents the results of over 200 experimental runs performed. Some immediate observations from the data are pointed out, but a detailed discussion of the experimental results is saved for chapter 6.

5.1 POSSIBLE FLOW CONDITIONS

As explained in chapter 4, the main purpose of the experiments was to determine the load on different components of the bridge and finding out whether or not these loads would lead to failure. The experiments were to be conducted by varying the inundation ratio h^* and the Froude number Fr independently of each other. During the initial stages of the experiment it became apparent that some combinations of flow depth and flow velocity just upstream of the scale model bridge cannot be replicated. In particular, achieving Froude numbers greater than 0.55 while $h^* \geq 0$ in front of the bridge proved to be difficult using the current experimental setup. An explanation to this observation is given.

The bridge piers, abutments and bridge deck act as a blockade in the river channel. Combined, more than one third of the gross cross-section is blocked compared to the case of an unrestricted flow that would reach the top of the deck, see Figure 64. It is obvious that when an object is placed into a flow, the flow in the area upstream of the object will slow down and its depth will increase (backwater effect). As long as the flow around the object remains subcritical, the flow depth downstream of the object influences the flow depth upstream of it.

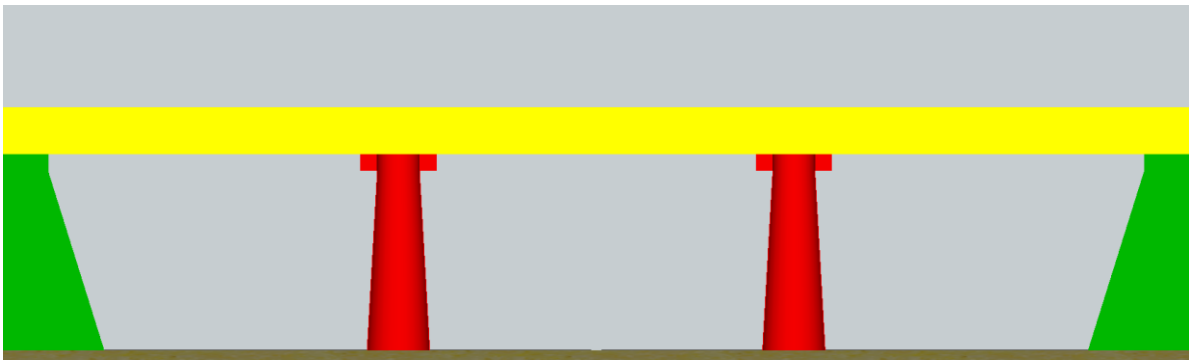

Figure 64: front view of the bridge scale model

Conversely, when the flow downstream of the bridge scale model becomes supercritical as a result of the contraction of flowlines caused by the scale model, the discharge and flow depth upstream of the model are no longer independent of each other. In fact, in the case of free flow over a weir, discharge and flow depth over the weir are related according to Equation 5-1. This means that when the total discharge is increased in an attempt to increase the flow velocity, the flow depth also increases. It is no longer possible to regulate flow depth and flow velocity independently of each other, while that ideally possible for the experiments.

$$Q \propto h_u^{3/2} \qquad \text{Equation 5-1}$$

where

Q	Discharge	[m^3/s]
h_u	Flow depth	[m]

During the experiments, the maximum flow velocity that could be achieved in the flume was approximately 80 cm/s at $h^* \approx 3.00$ ($Fr \approx 0.535$) when all components of the scale model were placed in the flume. The flow

behind the scale model is then supercritical. The maximum achievable velocity for different flow depths ranging from 10.0 cm to 22.0 cm was experimentally determined, see Table 7 and Figure 65.

h_u [cm]	h* [-]	U_u [cm/s]	Fr [-]
10,0	0,00	52,3	0,528
10,5	0,00	52,8	0,520
11,0	0,00	53,7	0,517
11,5	0,00	56,5	0,532
12,0	0,00	56,5	0,521
12,5	0,00	56,6	0,511
13,0	0,13	59,4	0,526
13,5	0,30	59,6	0,518
14,0	0,47	59,4	0,507
14,5	0,63	59,6	0,499
15,0	0,80	59,7	0,492
15,5	0,97	59,9	0,486
16,0	1,13	60,1	0,479
16,5	1,30	61,4	0,483
17,0	1,47	64,2	0,497
17,5	1,63	64,9	0,496
18,0	1,80	68,9	0,519
18,5	1,97	68,8	0,511
19,0	2,13	69,6	0,510
19,5	2,30	73,9	0,534
20,0	2,47	75,0	0,535
20,7	2,70	75,9	0,533
21,0	2,80	77,3	0,539
21,5	2,97	78,2	0,539
22,0	3,13	77,9	0,530

Table 7: Maximum flow velocities as a function of flow depth just upstream of the bridge model

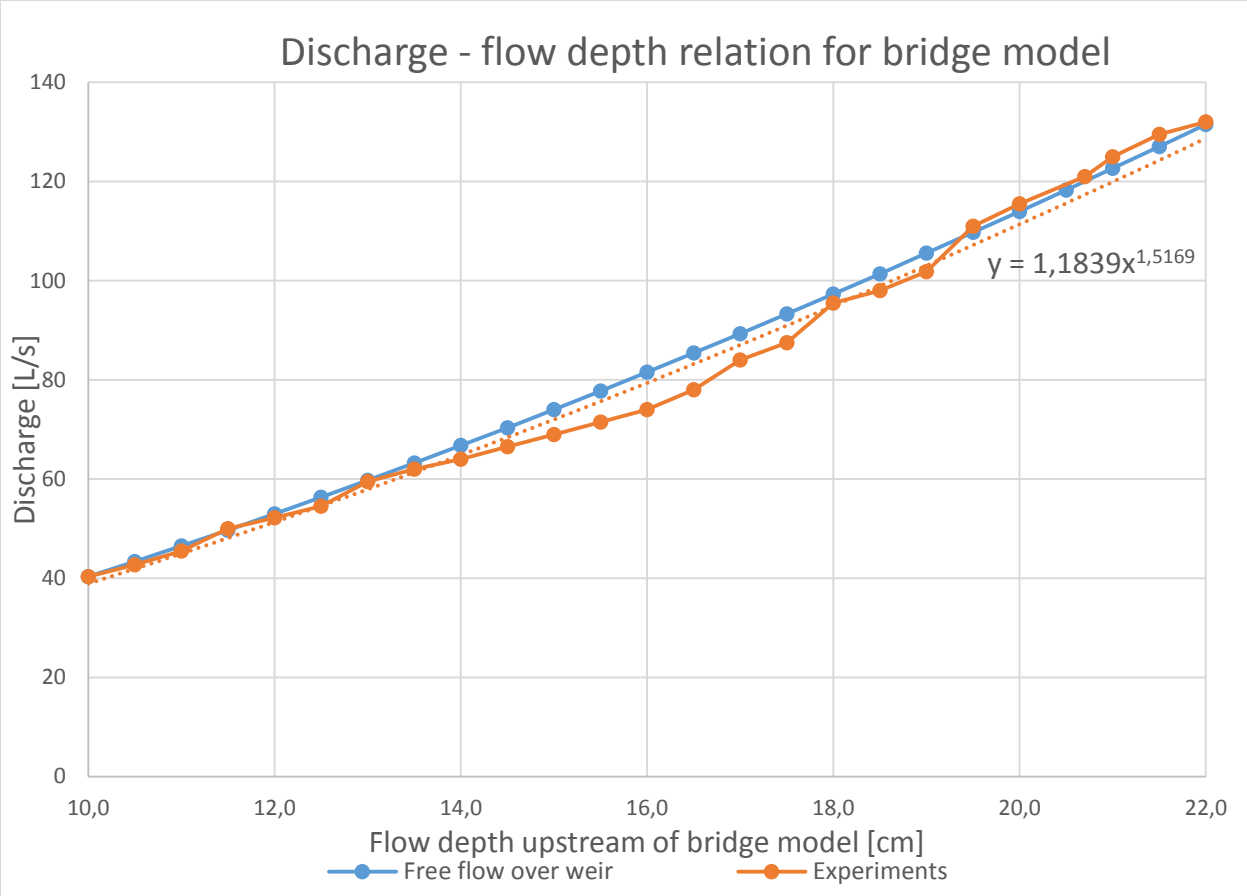

Figure 65: discharge – flow depth relation for bridge model, compared to the theoretical relation for free flow over a weir with a certain reference value Q_{ref} = 40.3 L/s at h_u = 10 cm

It may be concluded that some experiments with certain combinations of flow velocity and flow depth (for example U = 100 cm/s while h_u = 18 cm, Fr = 0.753) cannot be performed. This needn't be a limiting factor since the real bridge must have also restricted these characteristics of the river flow to certain bounds. Because the geometry and scaling of the scale model is quite accurate and Froude scaling is employed, it is expected that flow conditions unachievable in the experiments must have been unachievable in the field as well.

5.2 RANGE OF EXPERIMENTS

The following table shows the range of conditions under which experiments were performed. An experiment performed at 'maximum' Froude number entails that the flow velocity could not be increased any more at a specific flow depth, following the discussion in section 5.1.

Hypothesis 1 – deck – without debris	h_u = 12.0 cm to 20.0 cm	Fr = 0.33 to 'maximum'
Hypothesis 1 – deck – with debris	h_u = 13.0 cm to 19.0 cm	Fr = 0.10 to 'maximum'
Hypothesis 1 – pier – without debris	h_u = 8.0 cm to 21.0 cm	Fr = 0.40 to 'maximum'
Hypothesis 1 – pier – with debris	h_u = 8.0 cm to 17.0 cm	Fr = 0.34 to 0.52
Hypothesis 2 – combination – without debris	h_u = 12.0 cm to 21.0 cm	Fr = 'maximum'
Hypothesis 2 – combination – with debris	h_u = 16.0 cm to 21.0 cm	Fr = 'maximum'

Table 8: range of conditions for the experiments

5.3 SECOND HYPOTHESIS (COMBINED FAILURE)

As outlined in the introduction to chapter 4, the free-standing experiments were performed first. It was discovered early on that the combined pier-deck system was able to withstand even the most violent flow conditions that the flume could generate, both without and with large (exaggerated) amounts of simulated debris, as can be seen in Figure 66. Flow depths corresponding to an inundation ratio of over 3.0 and flow velocities as high as could be achieved were not able to cause the combined system to fail.

Figure 66: large amounts of simulated debris against the connected deck-pier system

The second hypothesis could therefore be discarded very early on, shifting the focus of the experiments to failure according to the first hypothesis. Nevertheless, load-cell experiments (without debris) were performed, to find the reason that no failure was observed. Figure 67, Figure 68, Figure 69 and Figure 70 show the drag forces, lift & buoyancy forces, moment around the object's center of gravity and resistance against rotation, respectively.

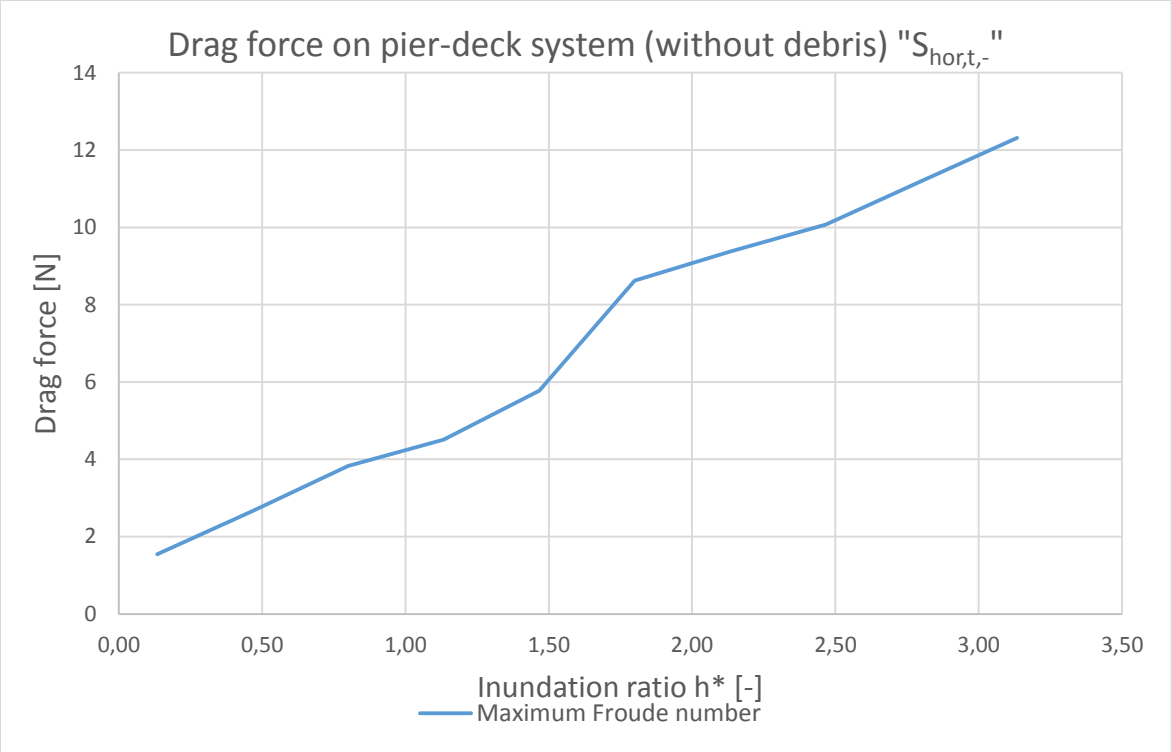

Figure 67: Drag forces on deck-pier system

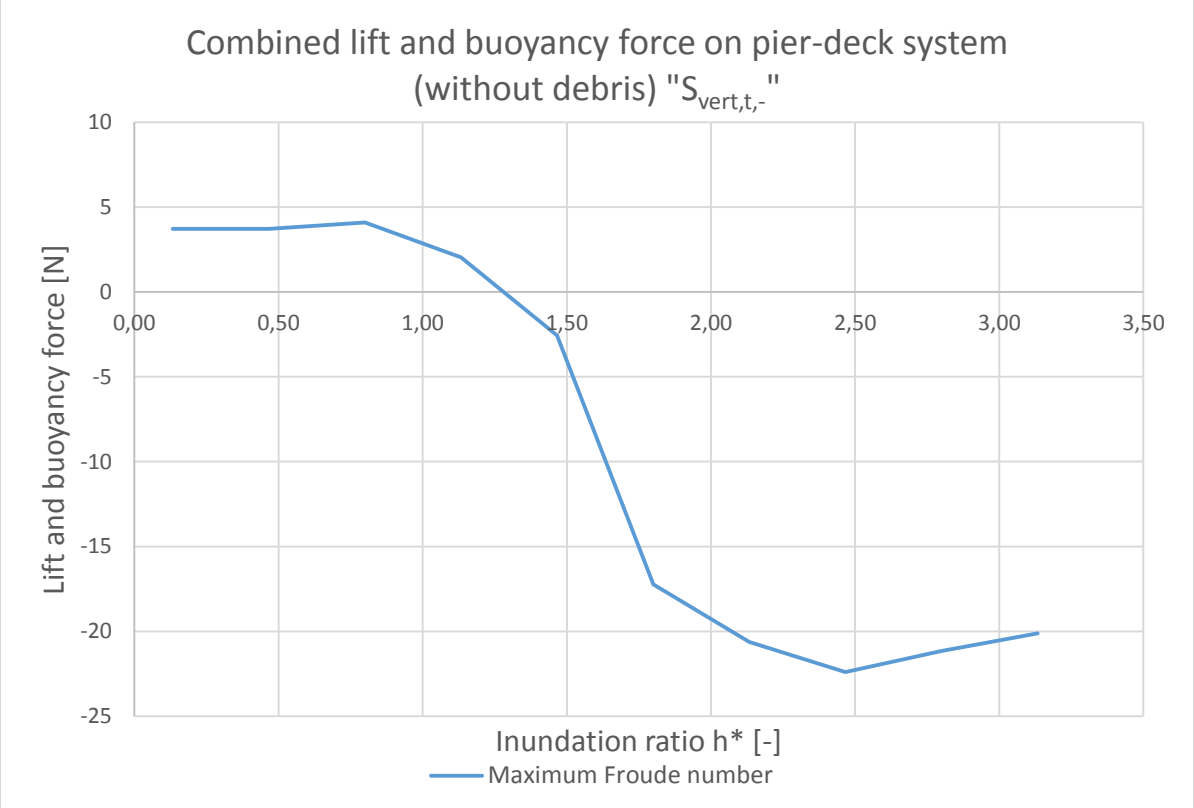

Figure 68: Combined lift and buoyancy forces on deck-pier system

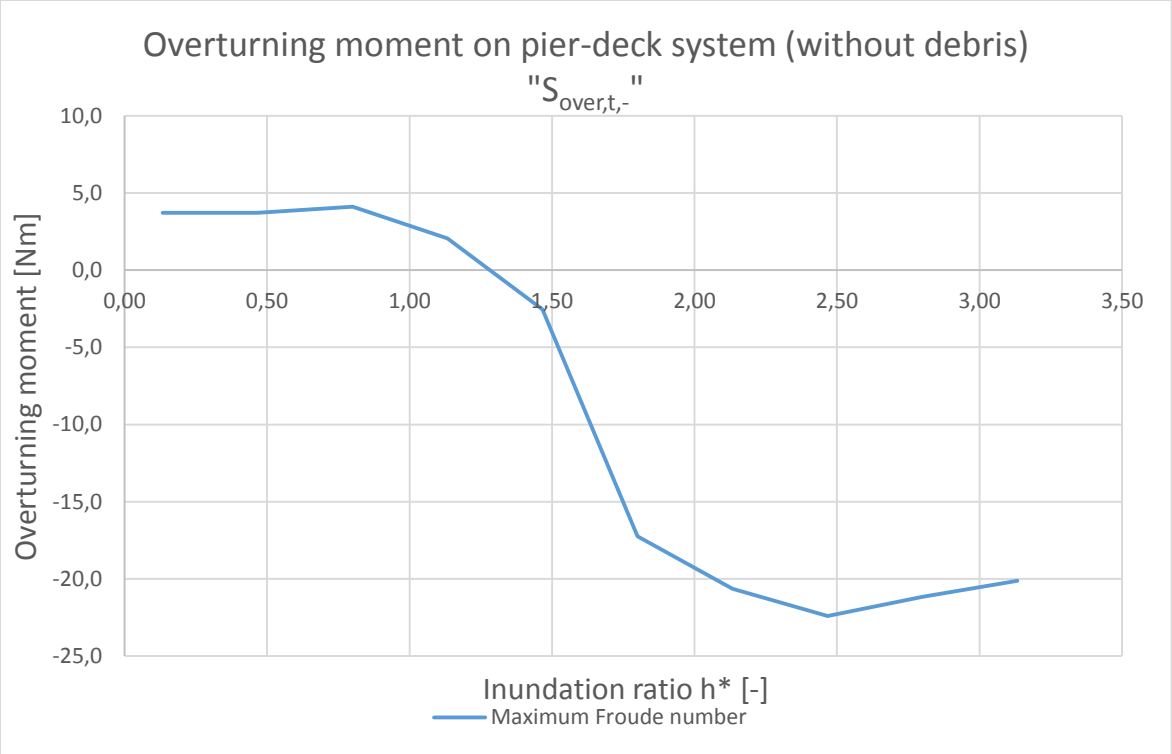

Figure 69: Overturning moment on deck-pier system around the point of rotation

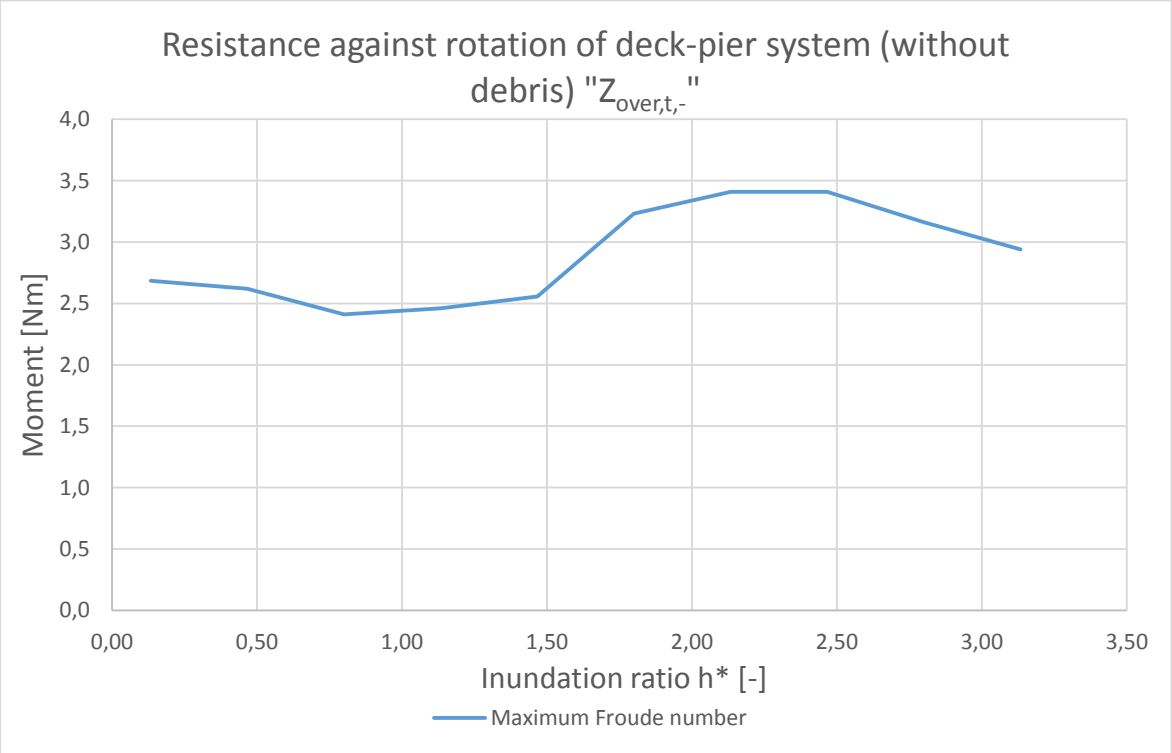

Figure 70: Resistance against rotation of deck-pier system without debris

It is evident that the results of the free-standing experiments (no observed failure) are consistent with the data from the load cell. It appears that the increasing drag force is fully compensated by the negative lift force are higher inundation ratios.

5.4 DECK (RESULTS, NO DEBRIS)

Following the hypothesis that failure of the bridge occurred in two stages, the forces associated with failure of the bridge deck were investigated. A photo of an experiment in progress is shown in Figure 71.

Figure 71: Experiment H1-D-Fs-18,0-0,40-N

Table 9 shows the results of the free standing experiments. A green cell indicates that no failure was observed, while a red cell means that failure was consistent. Yellow cells are critical values, and grey cells represent conditions that were above the maximum achievable Froude number or above a realistic inundation ratio. The numbers in the cells correspond to the Froude number of that experiment.

	h*	0,13	0,47	0,80	1,13	1,47	1,80	2,13	2,47	2,80	3,13	3,47	3,80
	h_u [cm]	13,0	14,0	15,0	16,0	17,0	18,0	19,0	20,0	21,0	22,0	23,0	24,0
U [cm/s]	50	0,443	0,427	0,412	0,399	0,387	0,376	0,366	0,357	0,348	0,340	0,333	0,326
	52	0,460	0,444	0,429	0,415	0,403	0,391	0,381	0,371	0,362	0,354	0,346	0,339
	54	0,478	0,461	0,445	0,431	0,418	0,406	0,396	0,386	0,376	0,368	0,359	0,352
	56	0,496	0,478	0,462	0,447	0,434	0,421	0,410	0,400	0,390	0,381	0,373	0,365
	58	0,514	0,495	0,478	0,463	0,449	0,436	0,425	0,414	0,404	0,395	0,386	0,378
	60	0,531	0,512	0,495	0,479	0,465	0,452	0,439	0,428	0,418	0,408	0,399	0,391
	62	0,549	0,529	0,511	0,495	0,480	0,467	0,454	0,443	0,432	0,422	0,413	0,404
	64	0,567	0,546	0,528	0,511	0,496	0,482	0,469	0,457	0,446	0,436	0,426	0,417
	66	0,584	0,563	0,544	0,527	0,511	0,497	0,483	0,471	0,460	0,449	0,439	0,430
	68	0,602	0,580	0,561	0,543	0,527	0,512	0,498	0,485	0,474	0,463	0,453	0,443
	70	0,620	0,597	0,577	0,559	0,542	0,527	0,513	0,500	0,488	0,476	0,466	0,456
	72	0,638	0,614	0,594	0,575	0,558	0,542	0,527	0,514	0,502	0,490	0,479	0,469
	74	0,655	0,631	0,610	0,591	0,573	0,557	0,542	0,528	0,516	0,504	0,493	0,482
	76	0,673	0,649	0,627	0,607	0,589	0,572	0,557	0,543	0,530	0,517	0,506	0,495
	78	0,691	0,666	0,643	0,623	0,604	0,587	0,571	0,557	0,543	0,531	0,519	0,508
	80	0,708	0,683	0,659	0,639	0,619	0,602	0,586	0,571	0,557	0,545	0,533	0,521

Table 9: free standing experiments (middle deck segment, μ = 0.25)

Figure 72 shows a photo taken during the load-cell experiment H1-D-Lc-18,0-0,40-N. One can see that the flow pattern across the bridge is almost identical as in Figure 71, which depicts the free-standing variant of this experiment. The replication of flow conditions has been successful.

Figure 72: Experiment H1-D-LC-18,0-0,40-N

Figure 73 shows the measured drag forces against a middle segment of the bridge deck (without debris). It concerns the 95th percentile of the measured forces (approximately equal to the mean plus two times the standard deviation). The reasoning behind choosing to plot the 95th percentile rather than the mean, has to do with the difference between static friction factor and dynamic friction factor. The dynamic friction factor is used to calculate the friction force when an object is already moving across a surface. The static friction factor is used to calculate the resistance against incipient motion. The static friction factor is always higher than the dynamic friction factor (except in some exotic cases). Since the change from static to dynamic friction factor can happen in milliseconds, the force causing incipient motion only has to be present during these milliseconds. As long as a sufficiently long data series was collected in steady-state conditions (this is the case for this research, every dataset spans at least 1 minute) the actual force exceeds the mean force half of the time. Only a very short period of time is necessary to initiate motion, and it is reasonable to assume a force greater than or equal to the 95th percentile of the series acts during this time.

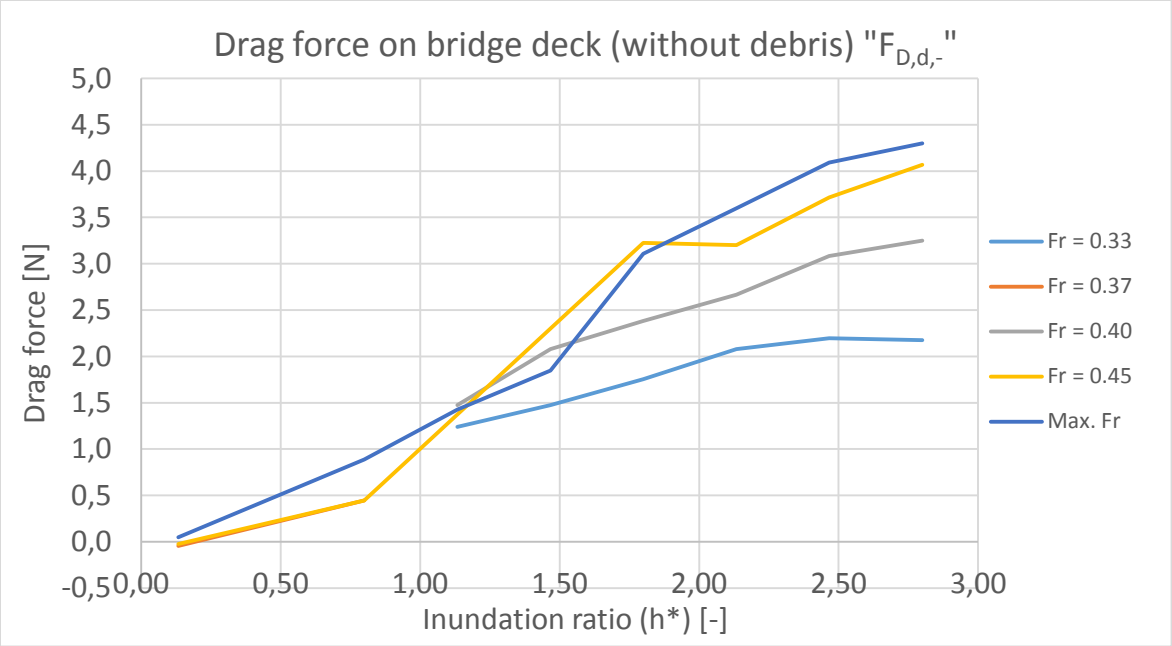

Figure 73: measured drag forces against a bridge deck without debris (middle segment), plotted against inundation ratio, for various values of the Froude number.

Figure 74 shows lift and buoyancy forces combined (5th percentile values). The reason for plotting the 5th percentile values follows the same motivation as for plotting the 95th percentile values of the drag force, however now the smallest values (which propagate to a smaller value of $Z_{hor,d}$) are of interest.

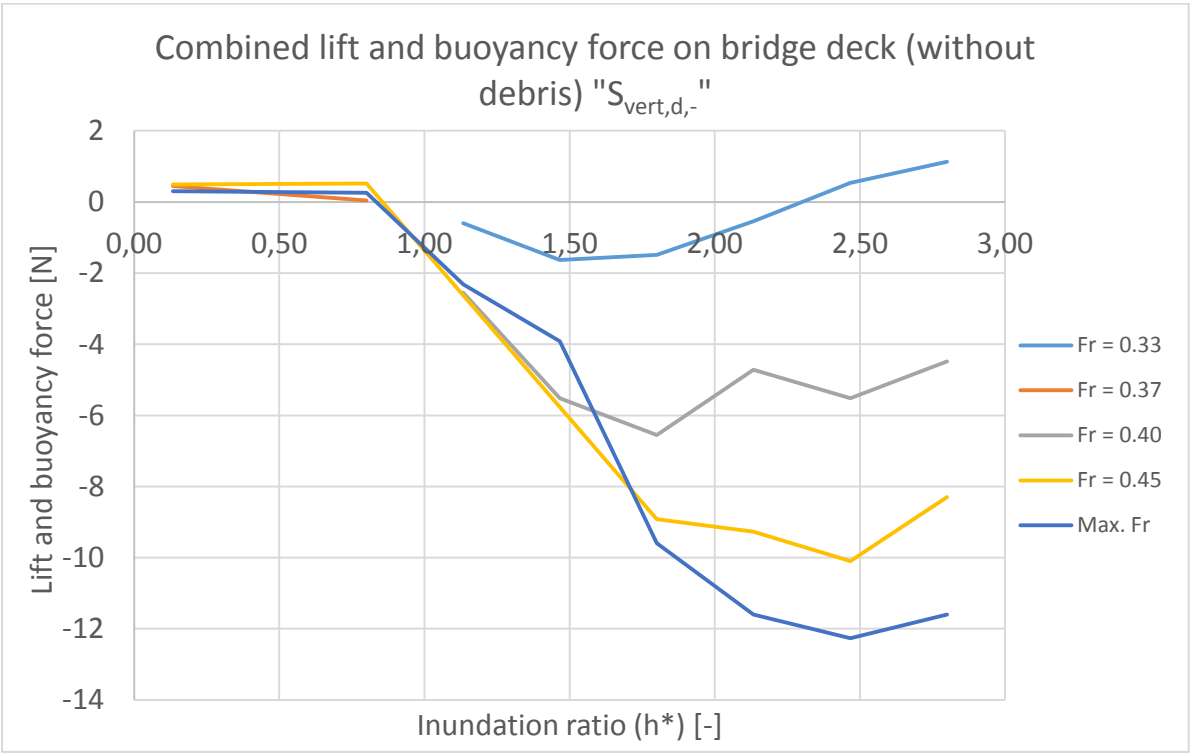

Figure 74: measured values of lift and buoyancy forces, for a bridge deck without debris, plotted against inundation ratio, for varying Froude numbers.

When the measurements of lateral (drag) forces and vertical (lift and buoyancy) forces are combined, it is possible to show the resistance to lateral movement, according to Equation 3-11, as in Figure 75.

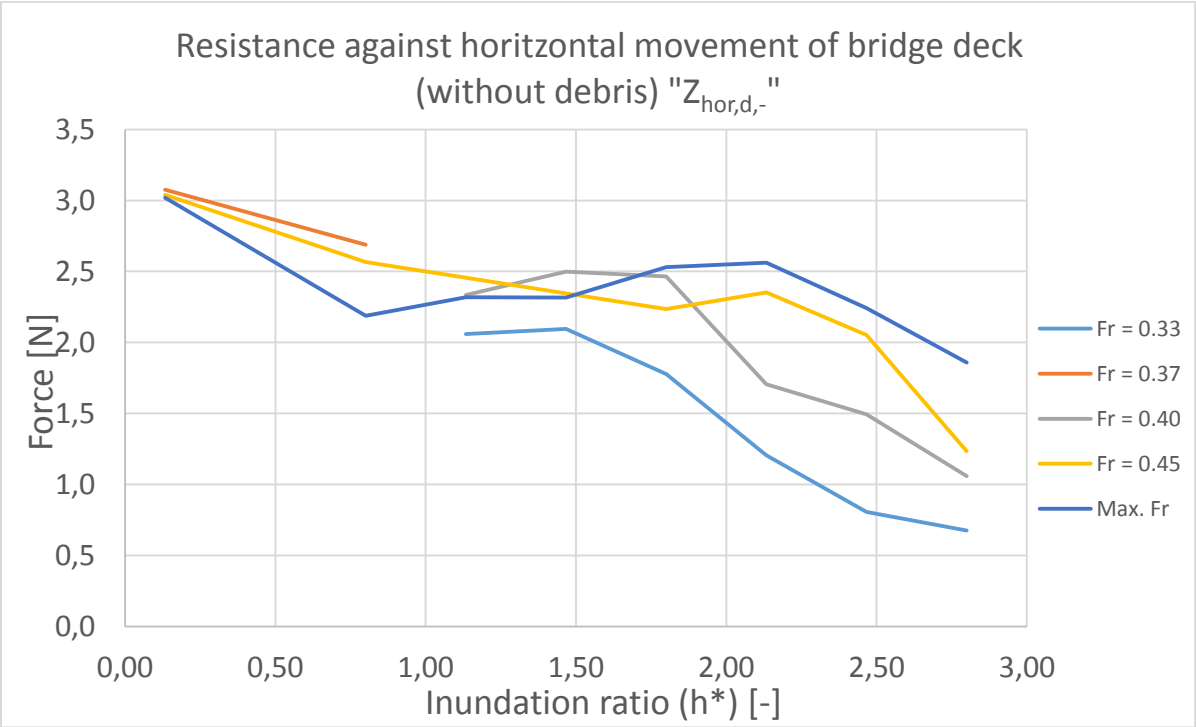

Figure 75: Resistance against horizontal movement of middle deck segment, friction factor μ = 0.25

Figure 76 shows the resistance against rotation of the deck.

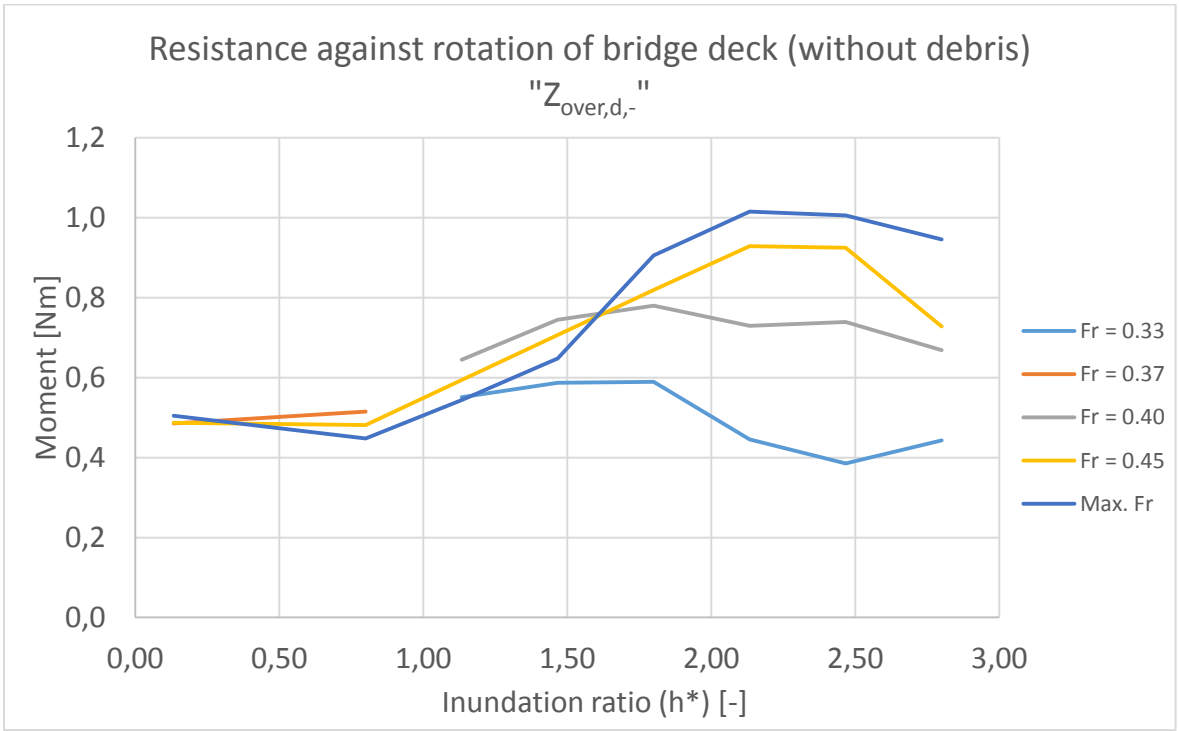

Figure 76: Resistance against rotation (middle deck segment, no debris)

Lastly, Figure 77 shows the resistance against horizontal movement of a side deck segment, which is to be compared to Figure 75.

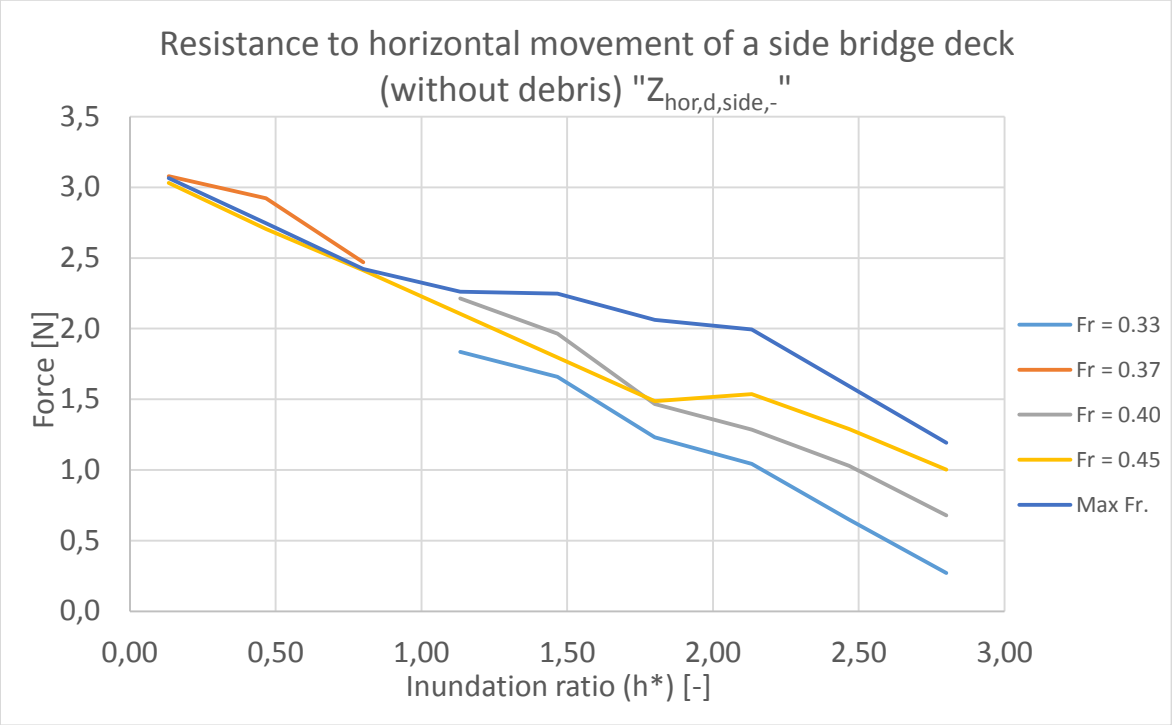

Figure 77: resistance to horizontall movement (side deck segment, no debris, μ = 0.25)

5.5 DECK (RESULTS, WITH DEBRIS)

The graphs in this section are presented differently than in section 5.4. Because of a larger variation of Froude numbers at which the experiments were performed, a 2D-graph would become cluttered, so a 3D-graph has a preference. Different shapes of debris and their effect on the forces were investigated. Data on the debris shapes is shown in Table 10.

	Wet weight (g)	Volume (cm^3)	Frontal area (cm^2)
Debris shape 1	364	520	132
Debris shape 2	330	471	132
Debris shape 3	322	459	109

Table 10: Data on the different debris shapes for the deck.

Two photos of experiment H1-D-LC-13,0-0,52-Y.1 are shown in Figure 78.

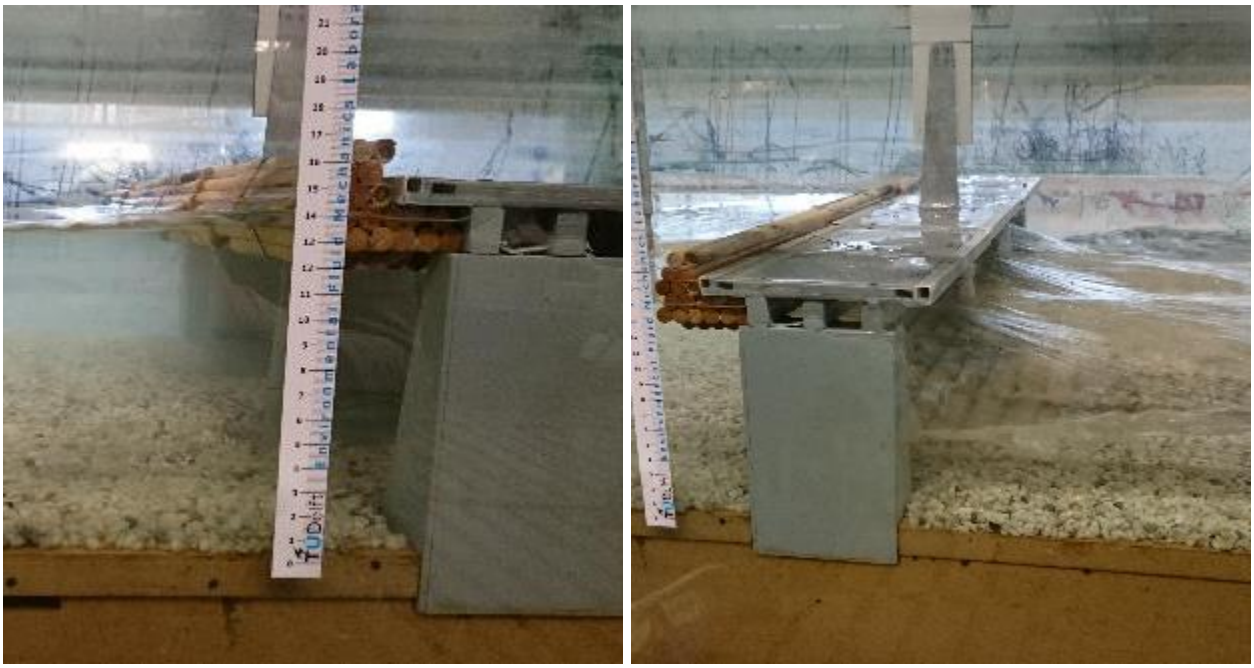

Figure 78: Experiment H1-D-LC-13,0-0,52-Y.1 in progress

Figure 79 aims to show the relation between 95th percentile of the measured drag force and the inundation ratio and the Froude number. Debris shape 1 was attached to all bridge deck segments.

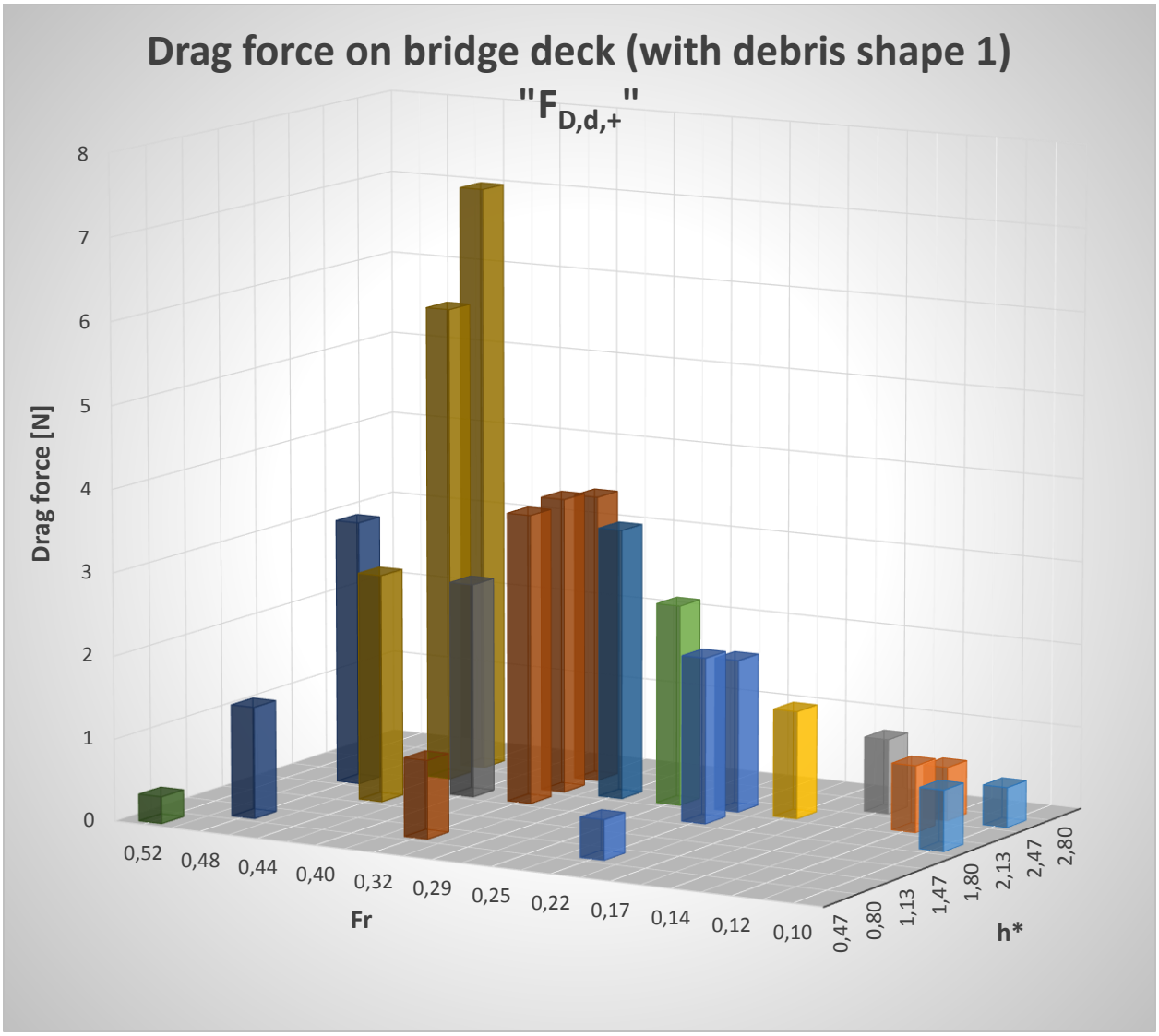

Figure 79: Drag forces on bridge deck (middle deck segment, with debris shape 1)

Figure 80 aims to show the relation between the 5th percentile value of the combined lift and buoyancy force and the inundation ratio and the Froude number.

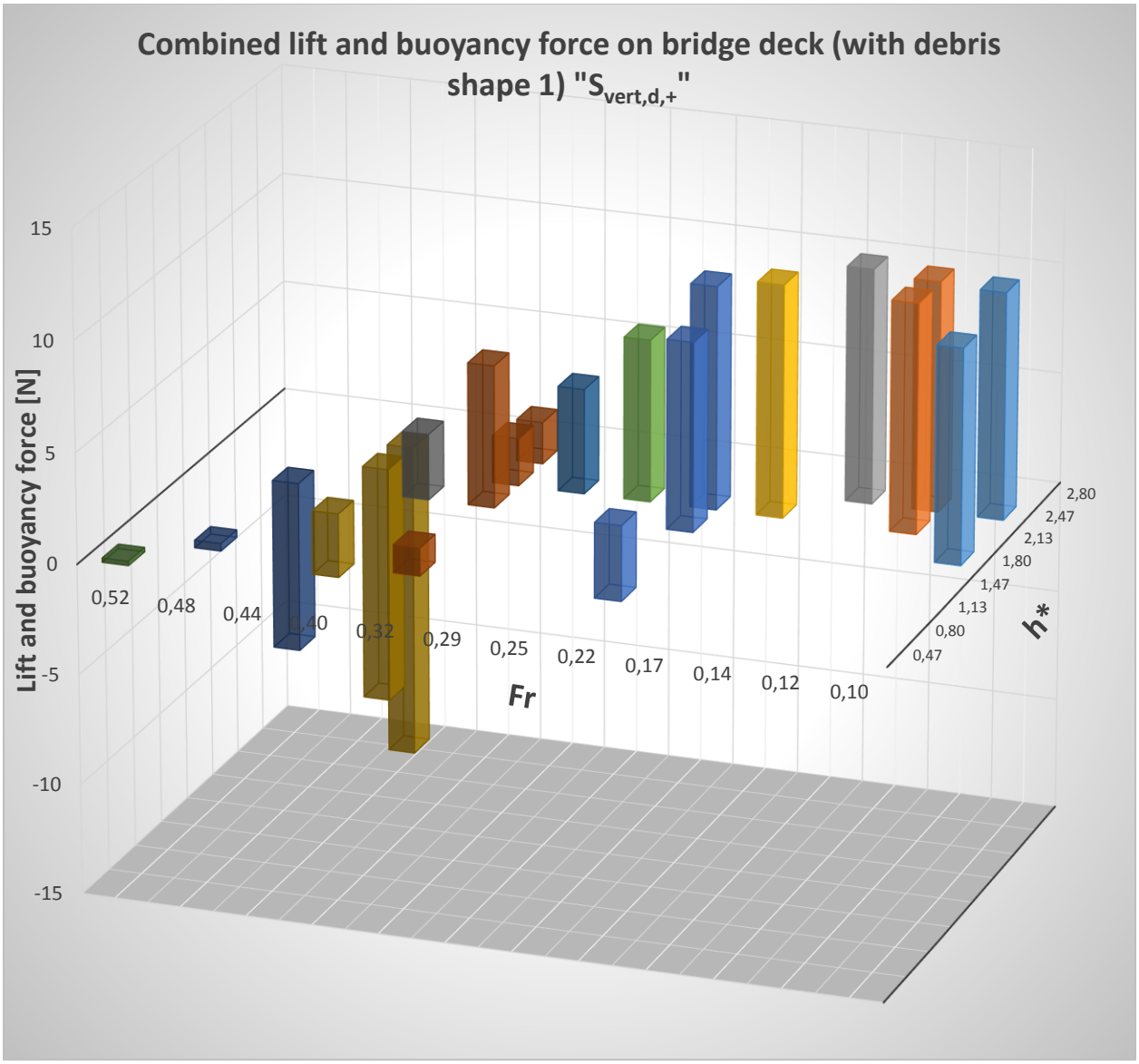

Figure 80: Lift and buoyancy forces on bridge deck (middle deck segment, with debris shape 1)

When the data on drag forces is combined with data on lift and buoyancy forces according to Equation 3-11, one can plot the resistance to lateral movement. This has been done in Figure 81. In this figure the solid dots denote non-failure of the deck, while the crosses denote that failure of the deck has been observed in the free standing experiments. The labels and the position on the horizontal axis denote the hydraulic conditions; Froude number and inundation ratio, respectively. The plot shows that for several experiments carried out at h* = 1.80, failure would be expected based on the load-cell experiment ($Z_{hor,d,+} < 0$) yet no failure was observed during the free standing experiments. Section 6.3 will elaborate further on this.

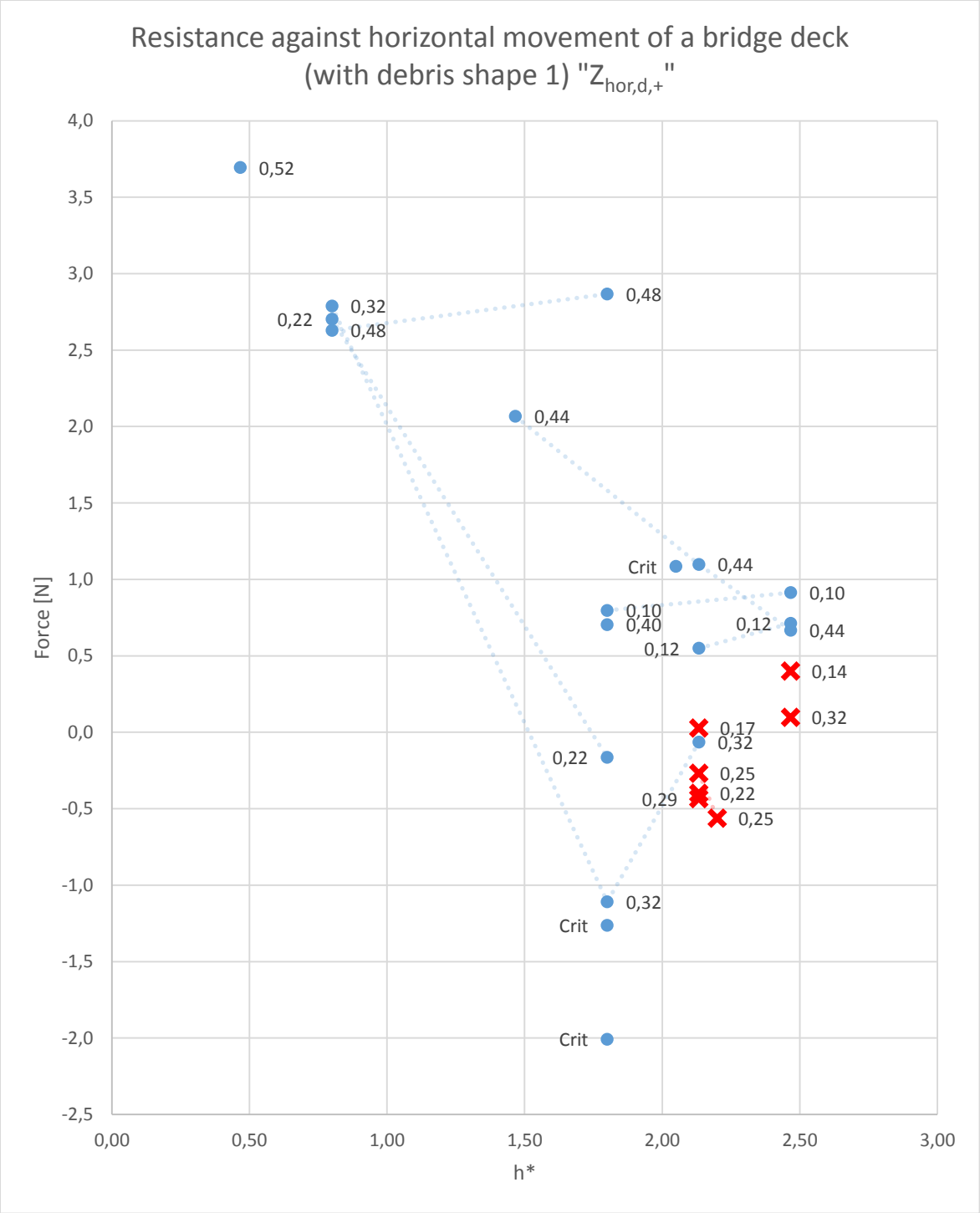

Figure 81: resistance against horzontal movement (middle bridge segment, with debris shape 1, μ = 0.25)

Finally, Figure 82 shows measured drag forces for different debris shapes under different flow conditions. Shape 1 and shape 2 have very similar drag characteristics, while drag forces were typically higher when shape 3 was used.

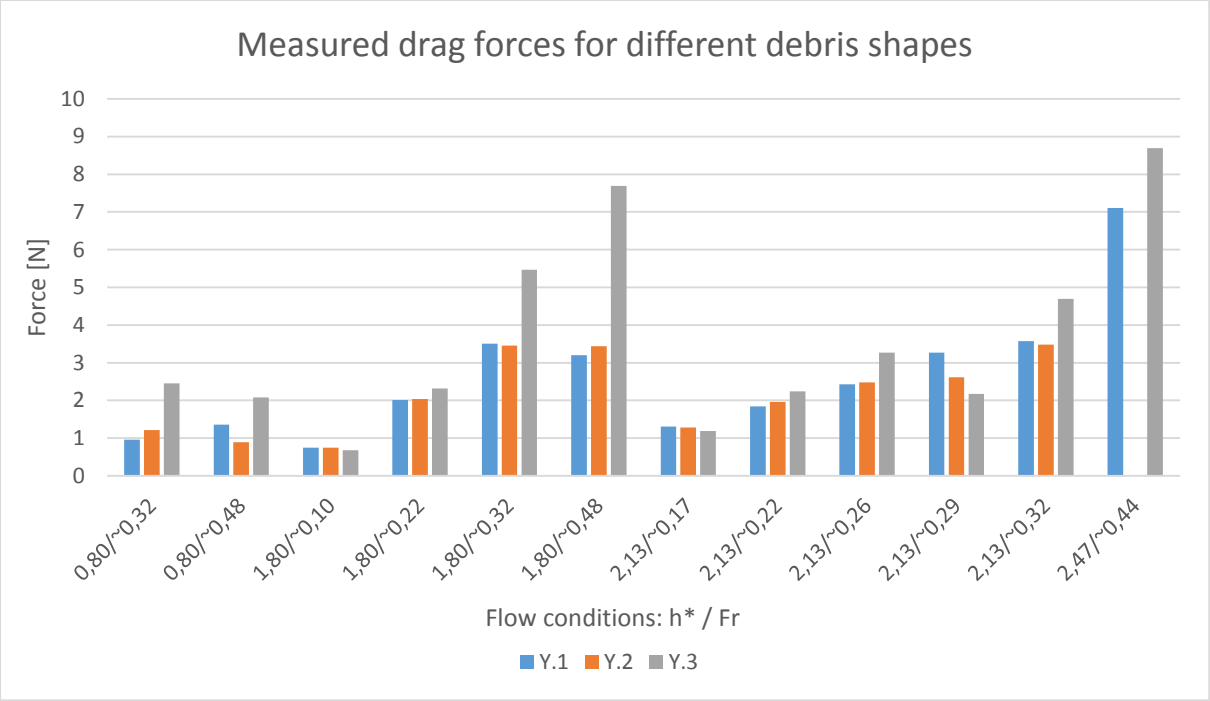

Figure 82: drag forces on middle deck segment, different debris shapes

5.6 PIER (RESULTS, WITHOUT DEBRIS)

A photo of a load-cell experiment on a pier in progress is shown in Figure 83.

Figure 83: Experiment H1-P-LC-14,0-0,45-N

Figure 84 shows drag force on the bridge pier without debris. Figure 85 shows the overturning moment acting on the bridge pier without debris (around its point of rotation). The data point at h_u = 17.0 cm for the highest Froude number is possibly an incorrect measurement.

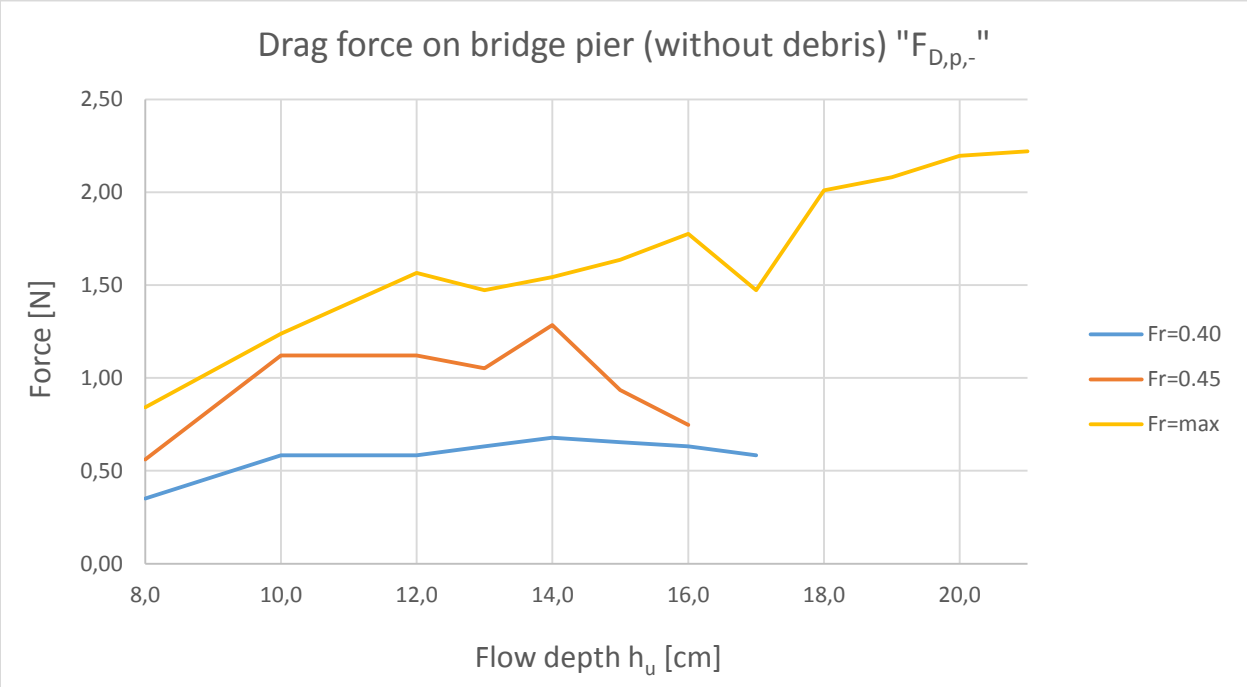

Figure 84: measured drag force (pier, no debris)

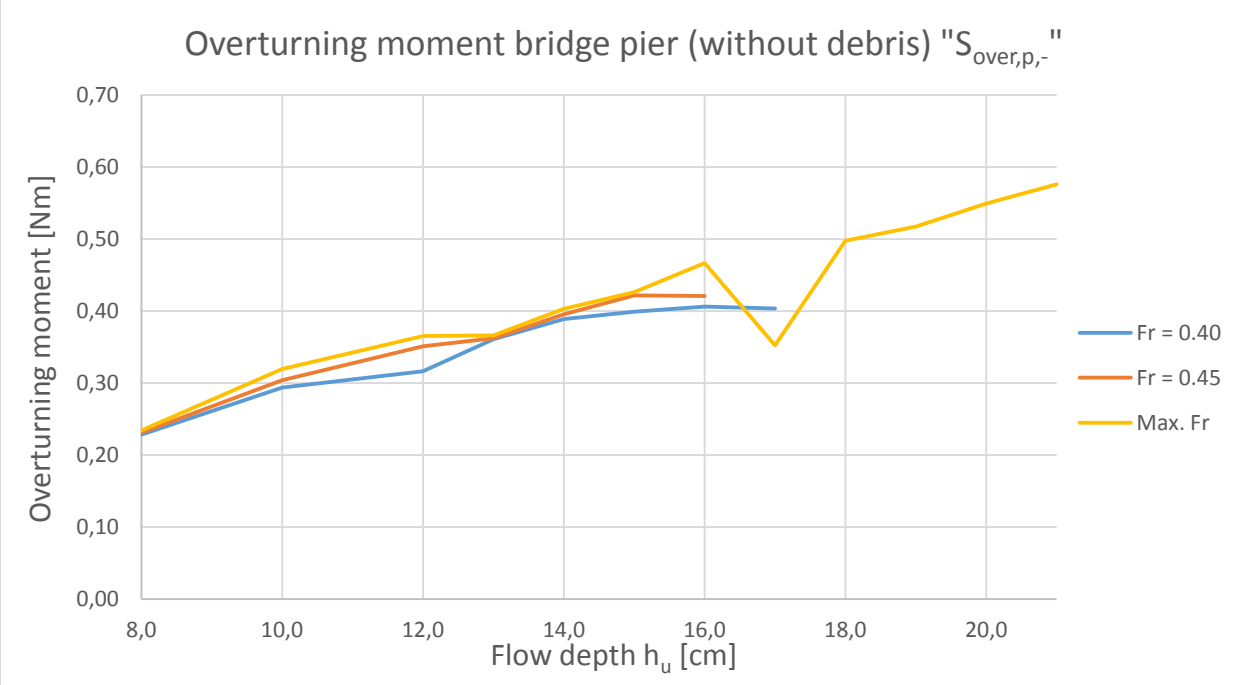

Figure 85: measured overturning moment (pier, no debris)

Since the only failure mode under consideration is failure by overturning, only the resistance against rotation is shown in Figure 86. Equation 5-2 is used to calculate the resistance against rotation.

$$Z_{over,p,-} = R_{over,p,-} - S_{over,p,-} \text{ where } R_{over,p,-} = F_{Z,p}L_{cg,p}\ ; S_{over,p,-} = F_{D,p,-}h_{cg,p} + F_{B\&L,p,-}L_{cg,p} - M_{cg,p,-}$$ Equation 5-2

where

$Z_{over,p,-}$	Resistance against rotation of the pier without debris	[Nm]
$R_{over,p,-}$	Restoring moment of the pier without debris	[Nm]
$S_{over,p,-}$	Overturning moment of the pier without debris	[Nm]
$F_{Z,p}$	Weight of the pier	[N]
$L_{cg,p}$	Horizontal distance between the center of gravity of the pier and the point of rotation	[m]
$F_{D,p,-}$	Measured drag force on the pier (without debris)	[N]
$h_{cg,p}$	Vertical distance between the center of gravity of the pier and the point of rotation	[m]
$F_{B\&L,p,-}$	Measured combined lift and buoyancy force on the pier (without debris)	[N]
$M_{cg,p,-}$	Measured moment around the center of gravity of the pier (without debris)	[Nm]

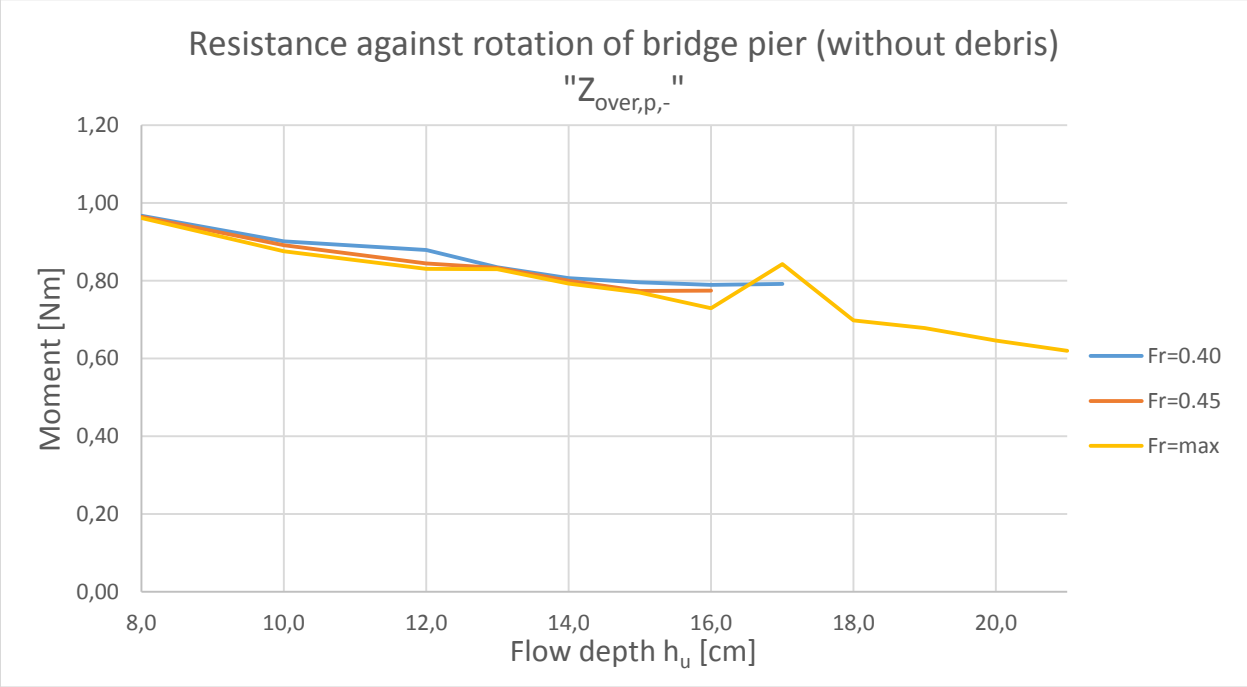

Figure 86: resistance to overturning (pier, no debris)

In the free standing experiments, no collapse of the piers was observed under any of the hydraulic conditions. This is backed up by the measurement data, which shows that there was sufficient resistance to overturning left even under the most extreme conditions.

5.7 PIER (RESULTS, WITH DEBRIS)

Different debris shapes were used to measure drag, lift and moment on the piers. The properties of these shapes are summarized in Table 11. Figure 87 shows an experiment in progress.

	Wet weight (g)	Volume (cm^3)	Frontal area (cm^2)
Debris shape XXL	382	545	100
Debris shape XL	292	417	83
Debris shape L	188	269	63
Debris shape M	108	154	52
Debris shape S	70	99	32

Table 11: debris properties (pier)

Figure 87: Experiment H1-P-LC-12,0-0,48-Y.XL

Figure 88 shows the drag force against the pier with the "XL" debris shape. The figure also shows singular data points for the "XXL" debris shape. The graphs for the other debris shapes are not shown here because not a lot of data was collected with these shapes. This was because it was clear early on during the experiments that the "S", "M" and "L" debris shapes would not lead to failure under any condition.

Figure 89 shows the overturning moment $S_{over,p,+}$ for the same shapes.

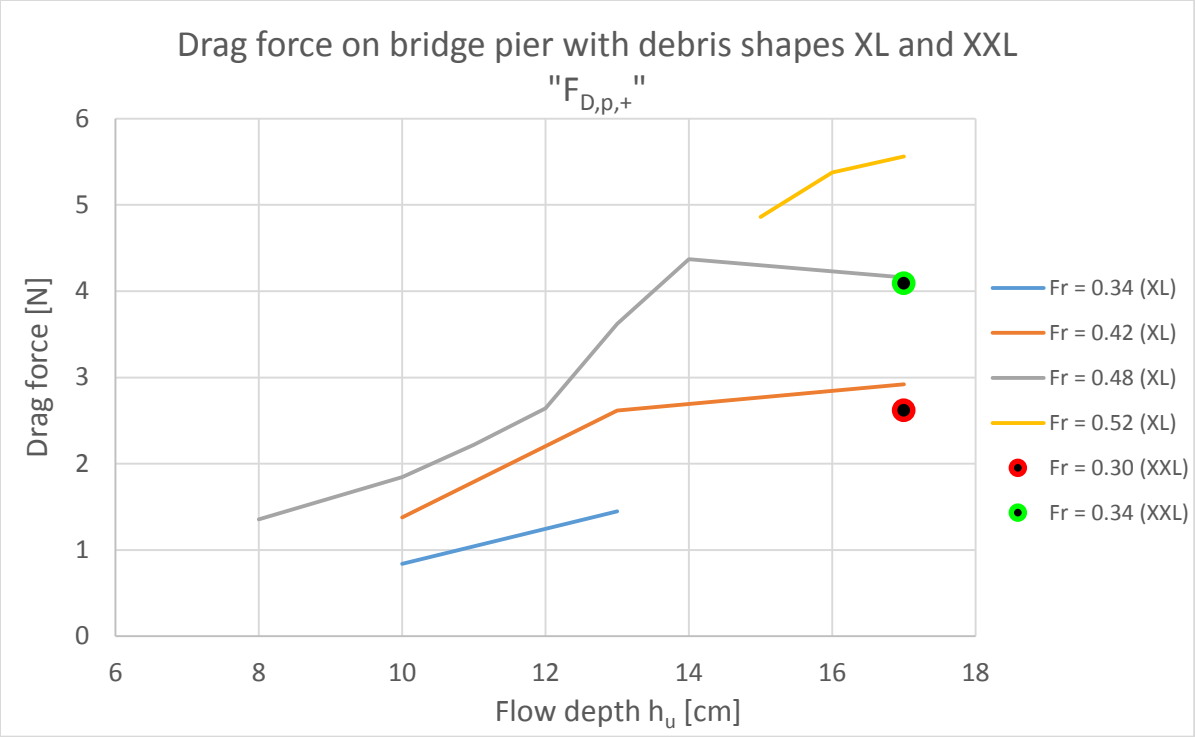

Figure 88: drag force on bridge pier with various debris shapes

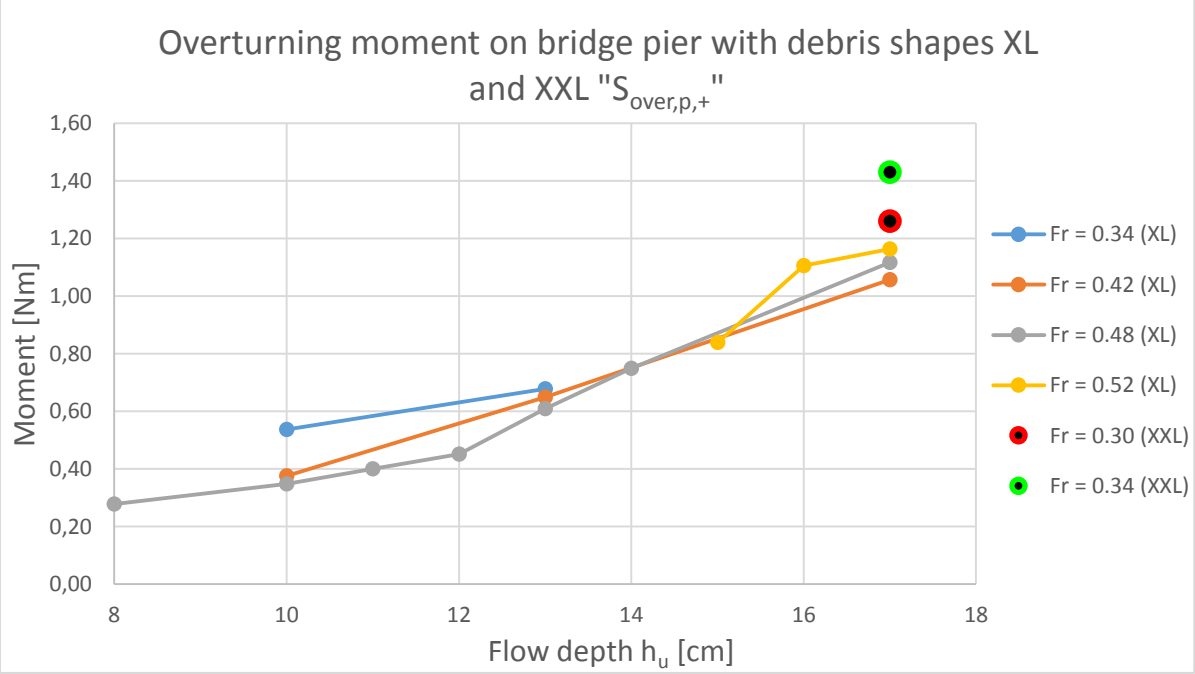

Figure 89: overturning moment on bridge pier with various debris shapes

Figure 90 shows the resistance against rotation $Z_{over,p,+}$ according to Equation 5-3. It shows that the pier with the "XL" debris shape at conditions Fr = 0.52 and h_u = 17.0 cm still had sufficient resistance to overturning, and this was confirmed by the free standing experiments. Only the "XXL"-shape at conditions Fr = 0.34 and h_u = 17.0 cm failed during the free standing experiments.

$$Z_{over,p,+} = R_{over,p,+} - S_{over,p,+} \text{ where } R_{over,p,+} = F_{Z,p,+}L_{cg,p}\,; S_{over,p,+} = F_{D,p,+}h_{cg,p} + F_{B\&L,p,+}L_{cg,p} - M_{cg,p,+}$$ Equation 5-3

where

$Z_{over,p,+}$	Resistance against rotation of the pier with debris	[Nm]
$R_{over,p,+}$	Restoring moment of the pier with debris	[Nm]
$S_{over,p,+}$	Overturning moment of the pier with debris	[Nm]
$F_{Z,p,+}$	Weight of the pier and additional debris	[N]
$L_{cg,p}$	Horizontal distance between the center of gravity of the pier and the point of rotation	[m]
$F_{D,p,+}$	Measured drag force on the pier (with debris)	[N]
$h_{cg,p}$	Vertical distance between the center of gravity of the pier and the point of rotation	[m]
$F_{B\&L,p,+}$	Measured combined lift and buoyancy force on the pier (including debris)	[N]
$M_{cg,p,+}$	Measured moment around the center of gravity of the pier (with debris)	[Nm]

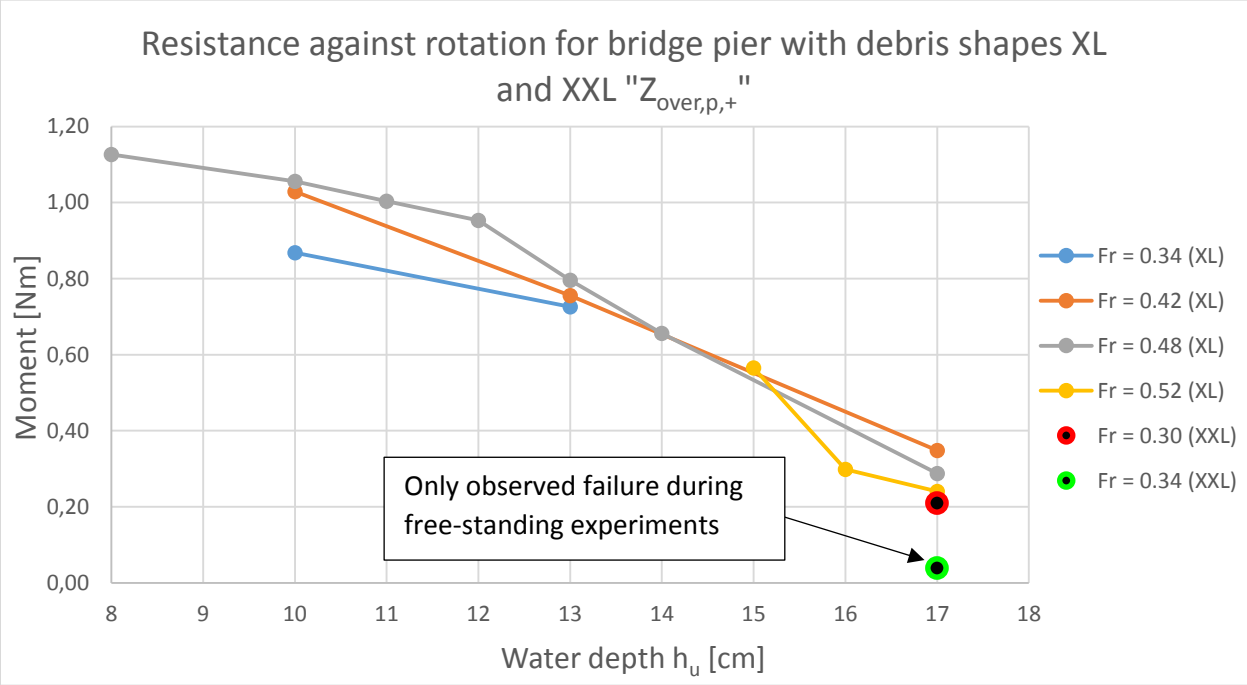

Figure 90: resistance against rotation for bridge pier with various debris shapes

5.8 UNSTEADY FLOW EXPERIMENTS

Apart from the majority of experiments performed under steady flow conditions, the forces on the deck were also recorded during a handful of non-steady flow experiments. An example is reduction of flow velocity (expressed by Froude number) while keeping the flow depth constant. A test was performed in which ***Fr*** was decreased from 0.32 to approximately 0.26 while keeping h_u constant at 18.0 cm. Figure 91 shows the resistance against horizontal (cyan), vertical (red) and rotational (green) movement, where the dotted blue line crosses 0, of this particular test. The load cell was attached to the middle deck segment and debris shape 1 was attached to the deck.

The spike readings visible in the graph are caused by sudden impacts on the load cell or the component attached to it. An adjacent deck segment failing and colliding with the segment fixed to the load cell can cause such a spike. These tests are thus fundamentally different from others as a load cell experiment is performed simultaneous with a free standing experiment, usually these were carried out at different times.

Careful examination of Figure 91 reveals that failure of the deck occurred when one of the resistances against movement became negative, in this case that of horizontal movement. Of course this is to be expected, failure happens when soliciting forces exceed the restoring forces. Figure 92 shows the mean value of resistances against horizontal movement and rotational movement for the duration of approximately 1 second before a failure. This has been done for the total of 8 unsteady flow experiments performed.

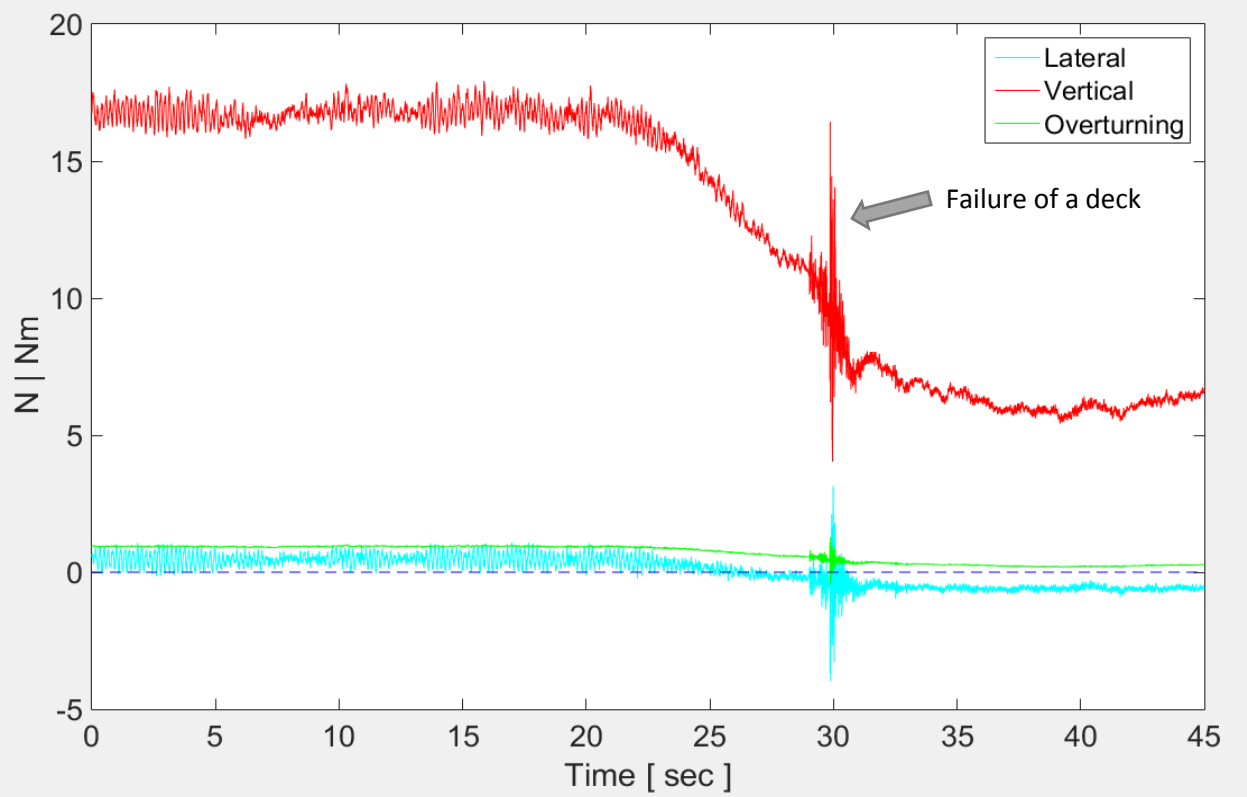

Figure 91: Resistances against horizontal, vertical and rotational movement of an experiment where the flow Froude number decreases from 0.32 to 0.26 for h_u = 18.0 cm

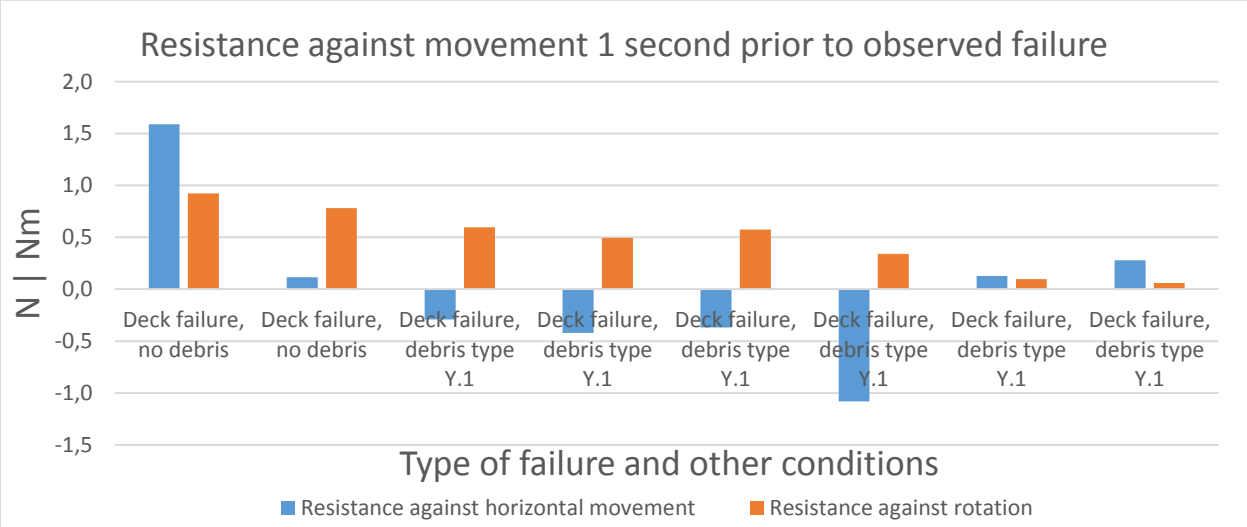

Figure 92: Resistance against lateral movement / resistance against overturning just prior to several recorded failures.

6 DISCUSSION OF EXPERIMENTAL RESULTS

This chapter aims to provide both superficial observations as well as some more in-depth analysis of the experimental results. The predictions of chapter 3 are compared to the results of chapter 5.

6.1 OBSERVATIONS FROM EXPERIMENTS

A bullet point-style summary of general observations from the experiments is listed here.

Deck without debris

- As Froude number increases, the overall magnitude of the drag forces and the negative lift forces increases as well. The net effect on the resistance against horizontal movement is positive, so the negative lift forces fully counteract the drag forces. Increasing Fr (at constant h^*) only will not cause the deck to fail.
- As inundation ratio h^* increases, the overall magnitude of the drag forces and the negative lift forces increases as well. The net effect on the resistance against horizontal movement becomes negative when $h^* > 1.5 – 1.75$, indicating that the influence of the drag forces starts dominating over the influence of the negative lift forces. Increasing h^* (at constant Fr) only will cause the deck to fail at some point.
- According to the load cell experiments, resistance against horizontal movement remained positive across all flow conditions that were tested. However, failure was visually observed under a few conditions. This inconsistency between the free-standing and load-cell experiments is addressed in section 6.3.
- It appears that the deck segments on the side have a slightly decreased resistance to horizontal movement compared to the deck segment in the middle. This is consistent with the visual observations; decks at the side typically started being displaced first, with the middle deck segment following quickly.
- Resistance against rotation remained sufficient across all tested flow conditions, and no failure by rotation (instead of sliding) was observed during the free-standing experiments
- Decks that have failed at high Fr conditions are washed away a large distance downstream by the flow. The simulated gravel bed did not provide sufficient friction to prevent the segment from washing away. Position (facing up or down) of the segments once they'd come to a rest seemed random.

Pier without debris

- The drag force $F_{D,p,-}$ is increasing as Fr increases (at constant h_u), which makes sense because the flow velocity U appears squared in the formula for drag force.
- The drag force $F_{D,p,-}$ is increasing as h_u increases (at constant Fr), only when the pier is exposed to the most violent flow conditons. For lower Froude numbers the total drag force actually seems to be decreasing for $h_u > 14.0$ cm. This can be explained by considering the hydrostatic pressures on the downstream side of the pier increasing and a small hydraulic jump appearing just downstream of the pier, see Figure 93.
- The overturning moment $S_{over,p,-}$ increased linearly with flow depth h_u, while the influence of Fr is hardly noticeable. Since the resistance against rotation is just a constant value minus the overturning moment, it also shows a linear downward trend in which the role of Fr is minimal.
- Resistance against rotation never dropped below 0, indicating a stable pier under all flow conditions without debris. This conclusion was indeed confirmed by the free-standing experiments. Collapse of the pier can thus only be explained by a debris accumulation.

Figure 93: (left) Experiment H1-P-LC-14,0-0,45-N; (right) H1-P-LC-16,0-0,45-N

Combined system without debris:

- The method of simply adding up forces from the deck and the pier used for predicting the forces on the deck-pier system adopted in chapter 3 could not be carried over to the experiments. Examination of the results shows that $S_{hor,d,-} + S_{hor,p,-} \neq S_{hor,t,-}$ for the deck-pier system without debris. This also holds for the vertical forces. Instead, the forces on the system were higher than on the sum of the individual components. Because of different flow patterns that emerge around the deck, pier and the system such a result is not surprising.
- Nevertheless, attempts to fail the system during the free-standing experiments by exposing it to (scaled) conditions way more intense than would be possible in the river were not successful.

Deck with debris:

- With a bit of imagination, a corner of a pyramid can be seen in Figure 79. This indicates that the drag force $F_{D,d,+}$ increases roughly linearly both with inundation ratio as well as the Froude number. A similar pattern was observed for the deck without debris.
- The magnitude of the drag forces of the with-debris case was almost always higher compared to the no-debris case, by anything between 10 to 100%.
- Figure 80 shows that at low to medium Froude numbers ($Fr < 0.40$) the buoyancy forces of the debris transferred to the bridge deck are dominant over the negative lift forces, independent on inundation ratio. Only at high values of Fr the negative lift forces take the upper hand in the expression for $S_{vert,d,+}$.
- Buoyancy forces of the debris are approximately 5 N when fully submerged, readily calculated by the volume of debris shape 1 (Table 10). This means that the negative lift force under conditions $h^* = 2.47$ and $Fr = 0.44$ (the tallest bar in Figure 80, value approximately -14.5 N) was approximately 20 N, which is double that of the without-debris case under the same hydraulic conditions. It may be concluded that a debris accumulation lodged against the bridge deck has a very significant effect on the lift coefficient.
- Resistance against horizontal movement was not found to be minimal at the highest range of Froude numbers, because negative lift forces push the deck down onto the bearing/pier causing increasing friction capacity. Instead, failure by sliding was observed at $0.17 < Fr < 0.32$ and $h_u > 2.1$. Failure by overturning was observed at $0.14 < Fr < 0.17$ and $h_u > 2.1$.

- According to the load cell experiments, resistance against horizontal movement would not have been sufficient under other flow conditions either. Free-standing experiments under those conditions however did not result in failure. This inconsistency is discussed in section 6.3.
- The difference between debris shapes 1 and 2 is negligible, so the cutouts in the front seemed to have no effect. The difference between shapes 1 and 3 is significant. Even though shape 3 has a smaller frontal area, drag forces are typically higher. Debris that extends further into the flow on the underside of the bridge generates higher drag forces, further proving that that flow velocities under the bridge are higher than over the bridge, as far as this was not yet evident by the negative lift forces.
- Deck segments with debris which failed consistently ended up with their top-side facing towards the bed, a distance approximately 2-8 times the width of the deck away from the test site. That distance depended on the flow velocity at failure and the corresponding failure mode (overturning or sliding).

Pier with debris

- The drag force on the pier with debris $F_{D,p,+}$ monotonically increases with increasing values of h_u, under the condition that the Froude number is the highest achievable. For Froude numbers less the maximum, drag force increases up to approximately h_u = 14.0 cm, then levels off or even decreases. This also occurred during the tests on the pier without debris, possibly due to a change of downstream conditions.
- The drag force is higher for higher values of Froude number, independent of h_u. This makes sense as the flow velocity U is squared in the expression for drag force.
- A larger frontal area of attack of the debris translate into higher drag forces on the pier. Again this is self-explanatory as the area of debris A_{deb} is linear in the expression for the drag force.
- Overturning moment exhibited an increase as flow depth increases, but showed little dependence on Froude number. This is similar to the case of the pier without debris.
- Resistance against rotation only approached critical values when the "XXL" debris shape was used. Indeed, under the same conditions failure by rotation was observed during the free standing experiments.
- Failure of the pier with debris occurs at $Fr > 0.34$ with a semi-cone debris shapes that has a frontal area of 100 cm^2, as long as $h_u > 17.0$ cm Accumulations having an even larger frontal area will cause the pier to fail at lower values of Fr.

Combined system with debris:

- The second hypothesis can be safely ruled out as a possible failure mechanism, as even the addition of exaggerated amounts of simulated debris into the experiment didn't produce any failure.

6.2 COMPARISON WITH PREDICTIONS

The most noteworthy difference between the predictions based on design standards presented in chapter 3 and the experimental results from chapter 5 must be the failure mechanism. Whereas failure according to the predictions should've happened according to the second hypothesis as the pier – even with debris – would never fail on its own, what was observed was the opposite; the resistance against overturning remained sufficient for the combined deck-pier system – even with a large amount of debris – while the model bridge pier did fail on its own, albeit only when a significant volume of debris was added.

Figure 35 and Figure 36 indicate that the resistance against rotation for the deck remained sufficient across all flow conditions. However, failure of a bridge deck with debris by overturning was actually observed during experimental work. This typically occurred at low Froude numbers (approximately 0.15) and inundation ratio of about 2.0. The reason for this mismatch is because throughout all of the predictions, the effect of debris-buoyancy (and debris weight) potentially being transferred to any of the components was disregarded. The debris-buoyancy (which dominates over the debris weight when the debris is submerged) constitutes a fairly large overturning moment on the bridge deck.

The reason that the model pier with debris did fail during the experiments lies in the projected area of debris and buoyancy of the debris being transferred to the pier. Section 3.2.2 states that a typical debris accumulation has a projected frontal area of 10.8 m^2 in the field. This amounts to 79 cm^2 ($10.5 \cdot 10^4$ cm^2 / 37^2 = 79 cm^2) when scaled down to fit the experiment, while the "XXL" simulated debris shape had a projected frontal area of 100 cm^2. This was done in order to find the amount of simulated debris necessary for rotation of the pier to occur.

Section 5.3 shows that the measured overturning moment around the point of rotation of the combined deck-pier system model without debris $S_{over,t,-}$ was 0.55 Nm at h^* = 0.80. Scaling up to field scale, this gives an overturning moment of 1.49 Nm × 37^4 = 1030789 Nm = 1031 kNm, which is much less than the predicted 3420 kNm at h^* = 1.92 in section 3.3.1. This can be explained by considering the blockage ratio, which is the frontal area occupied by the debris divided by the unrestricted cross-sectional area of the flow. As blockage ratio increases, the drag coefficient decreases, as can be seen from Figure 14 and Figure 15. This effect was not taken into account for the predicted value. The approach of simply adding up the forces from decks and piers to find to forces on the combined system does not produce adequate results.

The highest drag force measured on a deck segment was 7.1 N during experiment H1-D-LC-19,0-0,44-Y.1. Scaling up to field scale this corresponds to 7.1 N × 37^3 = 359636 N = 360 kN of drag force. Comparing to the failure modes of a bearing investigated in section 3.1.3, this is still much less than the capacity of the deformation failure mode of the bearing and the capacity of the concrete/steel failure modes. It can therefore be concluded that the prediction stating the friction failure mode as governing was correct.

It is also possible to compare the measured drag coefficients for the deck with the values given by Kerenyi et al. (6), this has been done in Figure 94. Although it needs to be stressed that these values strictly cannot be compared directly – as the values stated in (6) were derived for Fr = 0.32 only – the difference with the measured values is very large. For $h^* < 1.0$ the measured C_D-values are higher than those used for the predictions, while for $h^* > 1.0$ the measurement indicate lower C_D-values. However, Kerenyi et al. performed their experiments on an isolated bridge deck segment, while the measurements gathered for this research also include the effects of the nearby piers. Additionally, the geometry of the scale model used in this research was not an exact match to the geometry used by Kerenyi et al., this explains (part of) the discrepancy.

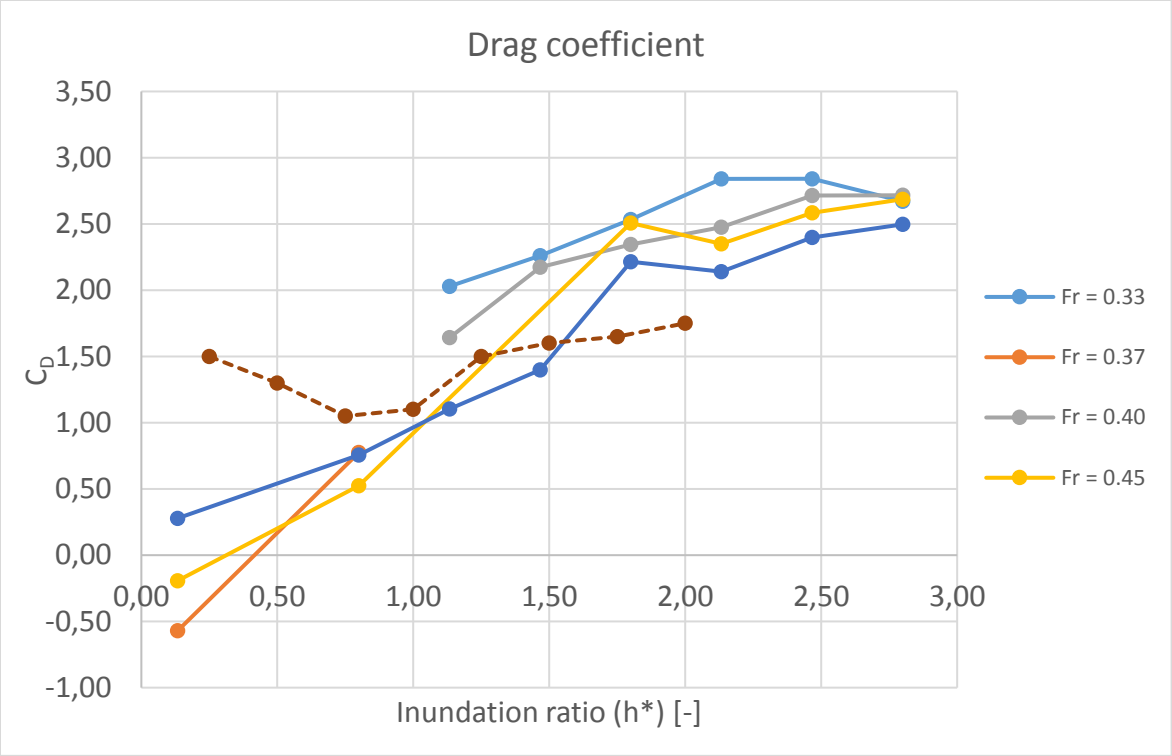

Figure 94: comparison of measured C_D-values and those reported by Kerenyi et al. (6)

A plot of the measured C_D-values of the pier is given in Figure 95. It can be seen that the values approach the predicted value of 0.7 as flow depth h_u keeps increasing. However the effect of boundary and free surface effects is clearly visible at low flow depths where the pier is not fully submerged.

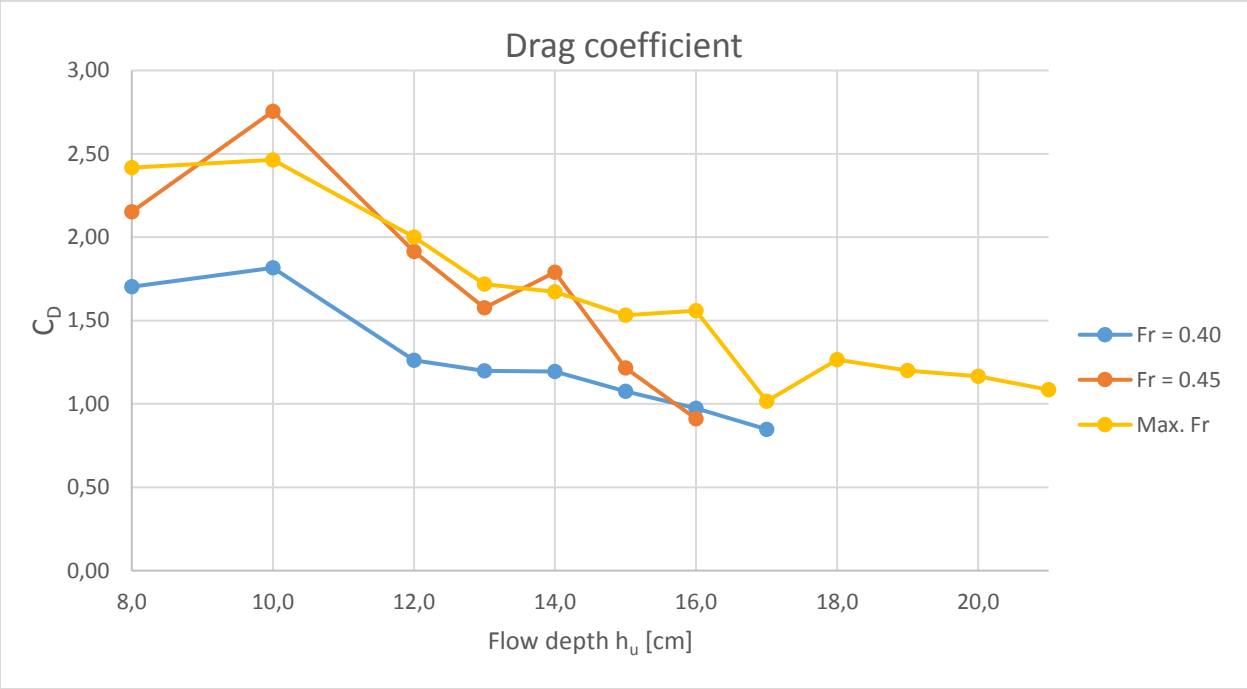

Figure 95: C_D-value (pier, without debris)

6.3 EVALUATION OF EXPERIMENTS

Inconsistency exists between the results of the free-standing experiments and the load-cell experiments. One would expect that if a failure of a component has been visually observed during the free-standing experiments, the resistance against movement of at least one of the three degrees of freedom (lateral, vertical, overturning) would be negative. Indeed, when the resistance against movement is calculated using the forces recorded by the load cell, that would be very near the critical value, in most cases. However, in other cases, the measurements from the load cell would indicate that the resistance would either still be sufficient or insufficient by a large margin.

An example of this is experiment H1-D-LC-17,0-0,32-Y.1. Figure 96 is a photo of the flow pattern around the bridge during this experiment. During the free-standing experiment, collapse was not observed. However, according to Figure 81, which plots the resistance against horizontal movement of this bridge deck, the soliciting forces were higher than the restoring forces under these conditions, indicating failure. There are several explanations for this disagreement between the results.

Figure 96: Experiment H1-D-LC-17,0-0,32-Y.1

For the case where no failure was observed in the free standing experiments, but it would be expected based on the results of the load cell experiment, the following causes can be considered:

a) The friction factor between the pier and the deck was determined when all of the experiments were performed. Also, the load cell experiments were performed after the free standing experiments. The surfaces of the scale models were coated with spray-on paint. It is not unthinkable that the continued exposure to water flow smoothened the contact surfaces between the girder and the pier to such an extent that the friction factor was significantly reduced. Abrasion of surfaces caused by sliding across the false bottom after collapse could have also contributed to lowering the friction factor over time.

b) Utmost care was taken to have the bridge component that was attached to the load cell not touch any of the other components, to ensure that no forces other than those caused by the flow were transferred to the load cell. To do so, models would be suspended in the water approximately 1 mm above other components and also have a clearance of approximately 1 mm on each side. Unfortunately, it is possible that there was some unnoticed contact between components. In that case, it is likely that an extra drag

force (due to unintended contact with adjacent bridge decks) or less downward force (due to unintended contact with a bridge pier) would have been recorded by the load cell under flow conditions.

c) For the experiments on bridge decks with debris specifically, the artificial debris may have become stuck against an abutment or pier once the deck had moved laterally for a small distance, preventing additional movement and failure.
d) Cumulative measurement errors leading to, for example, an indication of a higher drag force or lower downward force, can cause a disagreement between the results of this type. Section 6.4 elaborates further on this.
e) The connector that was used to connect the load cell to the bridge component causes the load cell to measure extra drag forces.

It is harder to explain cases where failure was observed, but the measurements from the load cell contradict this, claiming there would be sufficient resistance against movement remaining. Possibilities include:

a) Cumulative measurement errors leading to, for example, an indication of a lower drag force or higher downward force. Section 6.4 elaborates further on this.
b) Air entrapment in between the girders of the bridge deck model during free-standing experiments
c) Unintended contact between the deck and the bridge pier (causing the load cell to record less drag force).

6.4 MEASUREMENT ERROR

The accuracy of the comparison between the load-cell experiments and the free-standing experiments depends on the accuracy of the measurements. During the free-standing experiments, the flow depth h_u, the discharge Q, and the width of the flume B were measured. Additionally, during the load-cell experiments the forces and moments on the load cell were measured.

Load cell accuracy

The accuracy class of both the load cells used is stated as 0.1% by the manufacturer. This means that effects such as creep, non-linearity and hysteresis will cause the measured force to deviate from the actual force by a maximum of 0.1% of the full scale of the load cell. This corresponds to a maximum error of 0.5 N for each axis of the 3-axis load cell (full scale 500 N) and 0.05 Nm for the moment load cell (full scale 50 Nm). Such errors were however not observed during calibration of the load cells. This leads to believe that the stated inaccuracy of the load cell does not originate as a random error, but rather as a systematic error that can be corrected for with proper calibration and zeroing. The precision of the load cell turned out the be high, as vibrations of nearby machinery operating at a frequency of approximately 25 Hz causing forces as small as 0.15 N could easily be discerned, as can be seen from Figure 97.

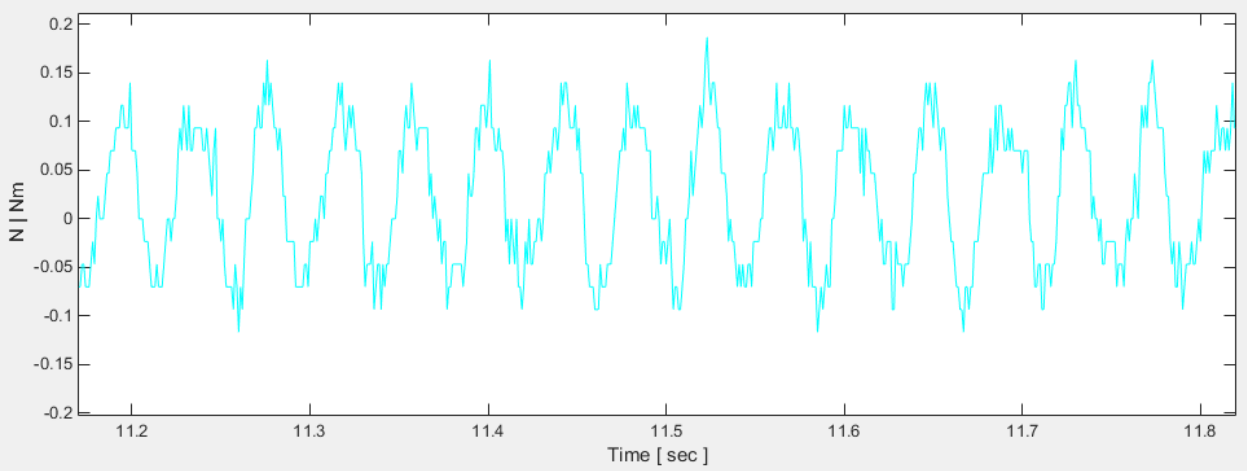

Figure 97: vibrations of nearby machinery causing very small loads could still easily be captured by the load cell.

Because a strong amplifier (1890x) for the electrical signal was used (this was necessary because typically forces were less than 5% of the full scale of the load cell), noise from the load cell was also amplified. Figure 98 shows the noise in the signal from the load cell/amplifier along the X-axis (direction of drag forces) expressed in N, as a static load was exerted. It can be seen that signal noise is responsible for approximately ± 0.05 N of error. The noise of the signal from the Y-axis (lift forces) is also approximately ± 0.05 N, while that of the signal from the torque-measuring load cell was approximately ± 0.01 Nm.

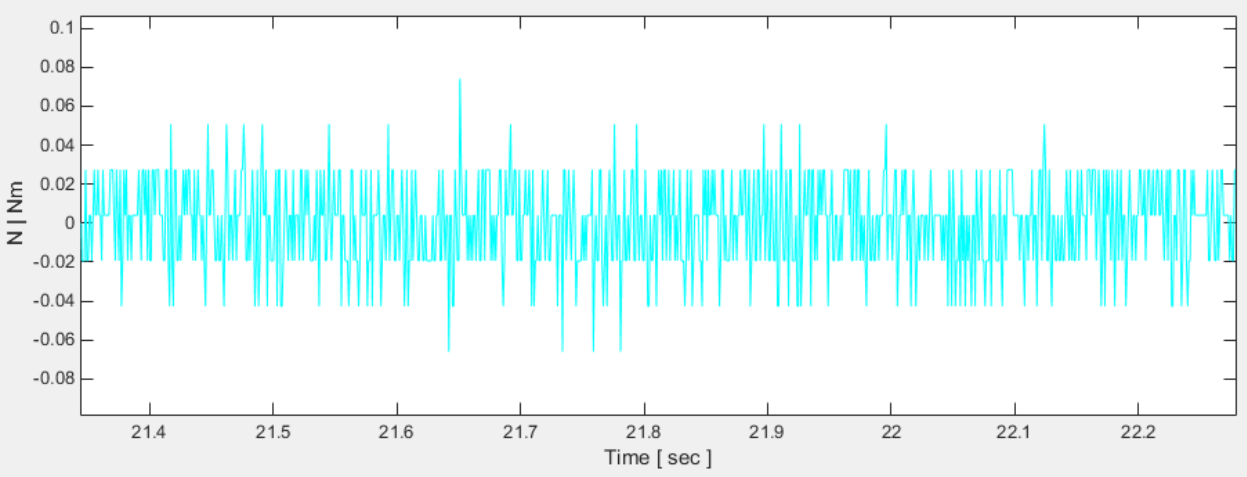

Figure 98: Noise in the signal of the load cell (drag)

Another issue that might cause the force readings from the load cell to differ from the actual forces, is that the X-axis of the load cell was not always parallel to the flume axis and therefore not to the direction of the drag force. Some misalignment possibly as large as 5° may have existed, causing errors up to 1 – cos(5°) = 0.4%.

Accuracy of h_u and *Fr*

The water depth was determined visually with a measuring tape attached to the transparent flume walls. The flow depths at another location such as the centerline might have been different. It is estimated that this error is of the order ± 0.5 cm.

Froude number is calculated according to Equation 6-1.

$$Fr = \frac{U}{\sqrt{g h_u}} = \frac{Q/_{B h_u}}{\sqrt{g h_u}}$$ Equation 6-1

where

Q	Total discharge	[m^3/s]
B	Width of the flume	[m]
h_u	Flow depth	[m]

The estimated error in ***Fr*** can be calculated according to Equation 6-2. The measurement error ***u(Q)*** of the device measuring the discharge ***Q*** was relatively large and determined to be approximately ± 3%. The width of the flume ***B*** was measured quite accurately, 770 mm ± 2 mm. g was assumed to exactly 9.81 m/s^2 without error.

$$u(Fr) = \sqrt{\left(\left|\frac{\partial Fr}{\partial Q}\right| u(Q)\right)^2 + \left(\left|\frac{\partial Fr}{\partial B}\right| u(B)\right)^2 + \left(\left|\frac{\partial Fr}{\partial h_u}\right| u(h_u)\right)^2}$$ Equation 6-2

where

u(<x>)	Expected error of quantity <x>	Variable
∂Fr/∂<x>	Partial derivative of the expression for Fr (Equation 6-1) to the variable <x>	Variable

	Measured value	Error
Q	83 L/s	± 2.49 L/s
B	770 mm	± 2 mm
h_u	18.0 cm	± 0.5 cm

Table 12

When the values of Table 12 are entered into Equation 6-1 and Equation 6-2, the following values for ***Fr*** and the error in ***Fr*** can be calculated.

$$Fr = 0.451$$
$$u(Fr) = 0.023$$

Other measured quantities were the weight of the component, weight of the debris and the friction coefficient, distances between the center of gravity and point of rotation of components. Each of these quantities also had their own measurement error that, combined with other errors, can (partially) explain the inconsistency between the free-standing and load-cell experiments.

Figure 99 and Figure 100 serve to further illustrate the order of precision of the experimental results. They show the variance in recorded drag forces – obviously while the same flow conditions were present – of different experimental runs performed on different days. The difference is about 10 to 20%.

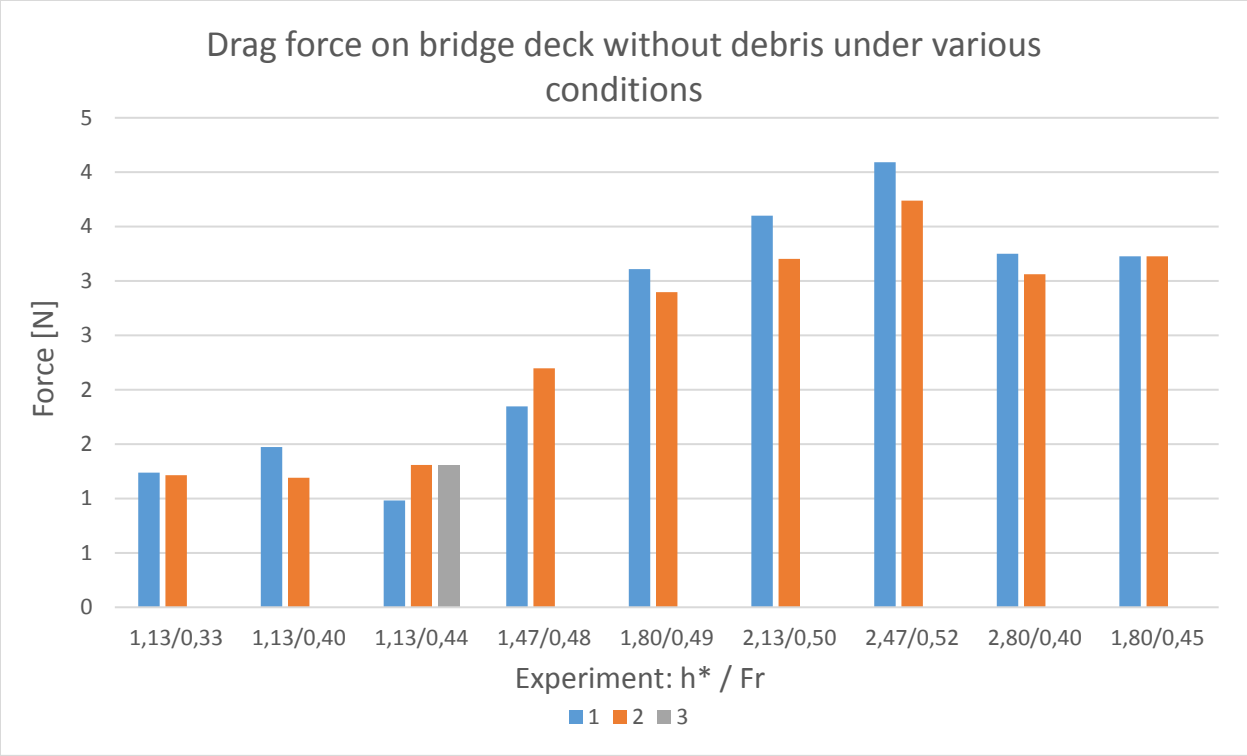

Figure 99: drag forces on a bridge deck without debris, from different experimental runs performed on different days

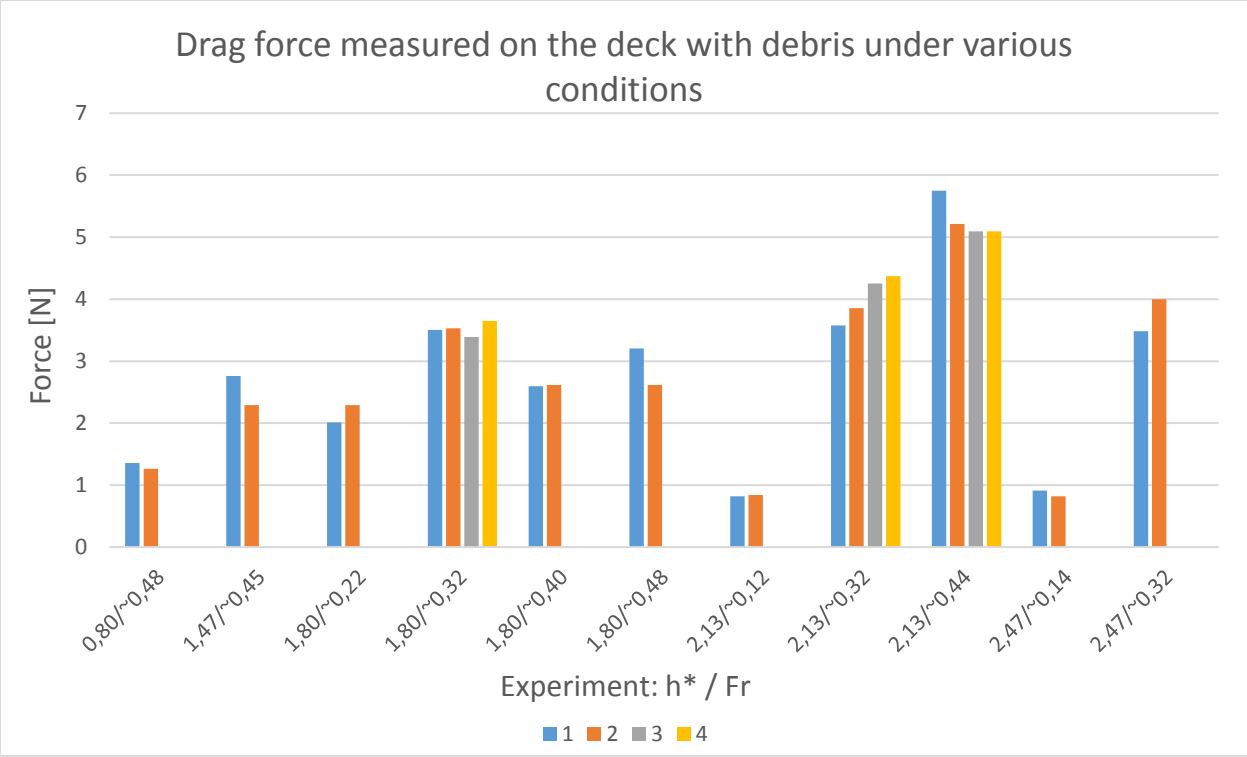

Figure 100: drag forces on a bridge deck with debris, from different experimental runs performed on different days

6.5 RECIPE FOR YABITSU BRIDGE FAILURE

The following chain of events can explain the collapse of the entire bridge:

1. As the water level in the river rises by extreme rainfall, the debris load by logs, twigs, leaves, other woody and man-made materials increases. Debris gets stuck under the bridge deck, gets wrapped around the piers and might even span the gap between two piers. Debris continues accumulating against the bridge deck and piers.
2. At some point the lateral load on a bridge deck segment due to the increased area of attack becomes larger than the frictional resistance the elastomeric bearings can provide. At that moment the inundation ratio h^* was larger than 2.1 ($h_u \geq 6.6$ m) and the Froude number anywhere between 0.14 and 0.32 (1.13 m/s $\leq U \leq$ 2.57 m/s for $h_u = 6.6$ m), in accordance with section 5.5 and Figure 81. This segment starts sliding/rotating off its piers and sinks to the riverbed. Due to the buoyancy forces of the debris lodged under the upstream side of the deck and the flow against the underside, an overturning moment develops. The deck flips over and ends up up-side down some distance downstream of the site. This process was observed during the experiments and is shown in Figure 101 and Figure 102. The altered flow pattern that is created causes downward lift forces on the remaining bridge decks to decrease, while drag forces are slightly increased, translating into even less resistance to horizontal movement/rotation. The other bridge decks subsequently also fail.

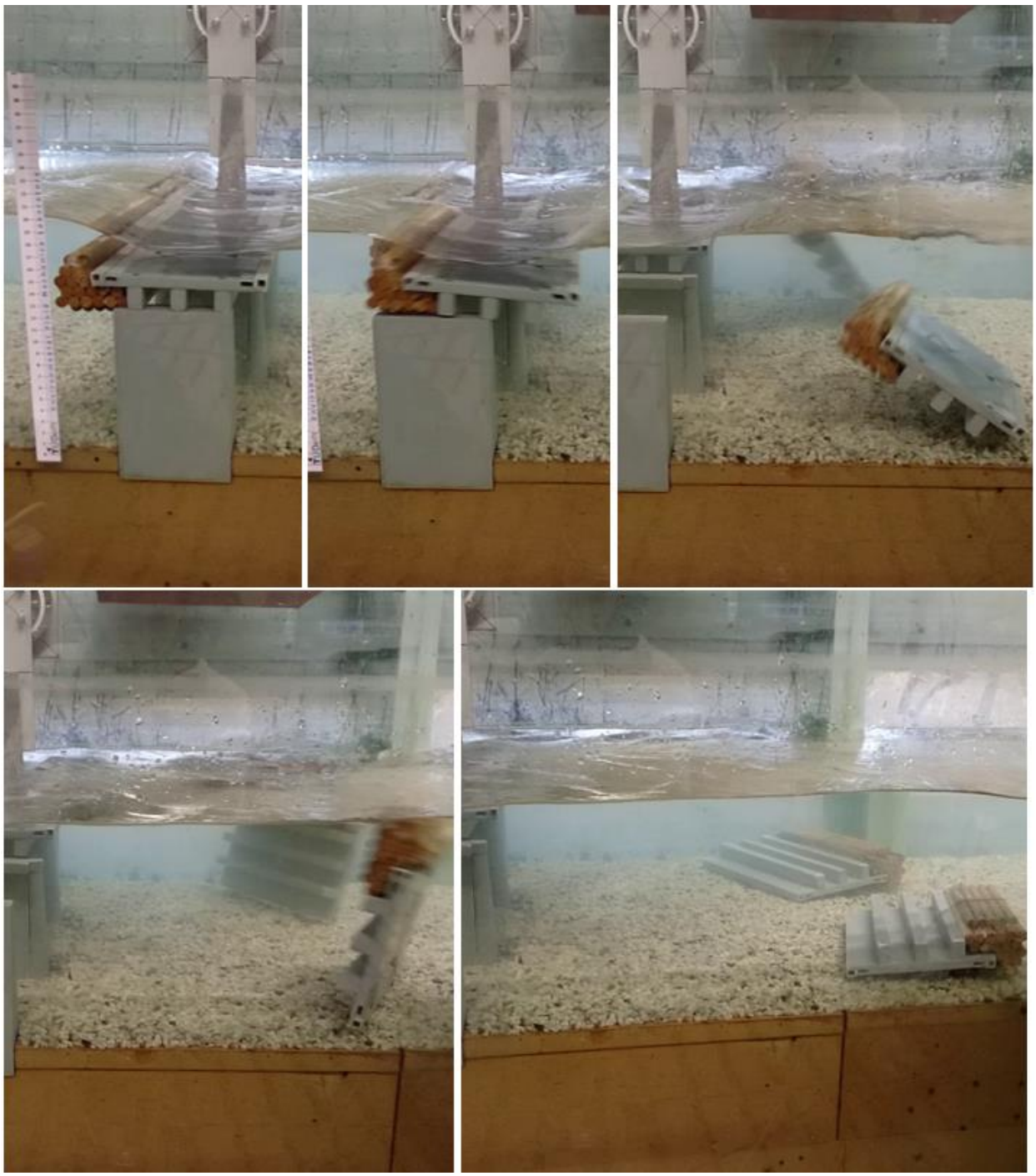

Figure 101: collapse of the bridge deck with debris by sliding at relatively high flow velocities

Figure 102: collapse of bridge deck with debris by overturning at relatively low flow velocities

3. Because the bridge decks now no longer act as a blockage in the river, the water level drops and the flow velocity increases, i.e. the Froude number becomes greater.
4. Debris wrapped around the piers nullifies the effects of their aerodynamically rounded ends and drastically increases the area of attack. Moreover there is less weight (from the decks) on the piers and possibly buoyancy forces of the debris are transferred to the pier. This creates conditions under which the piers can fail, namely $h_u \approx 6.3$ m ($h^* \approx 1.80$) and $Fr \geq 0.34$ ($U \geq 2.67$ m/s), according to section 5.7 and Figure 90. The piers rotate around their foundation and topple over, settling on the riverbed where the flow velocities are smaller. Figure 103 shows this process as observed during the experiments.

Figure 103: collapse of bridge pier

7 COUNTERMEASURES & PREVENTION

Countermeasures can be based on reduction of soliciting forces or increasing the restoring forces. Several straightforward solutions to bridge collapse by hydrodynamic forces can be thought of. These are based on preventing the application of large forces on a bridge deck or bridge pier altogether. By building the superstructure higher above the riverbed (increased h_b) the water may never reach the level of the deck during a flood. Designing the bridge with a single span eliminates the need to place bridge piers in the river. This is without a doubt the most effective solution: there is no blockage of the cross-section by piers, so there is no backwater, leading to overall lower water levels. There is no obstruction in the path of the river that debris might get stuck on. However, a high, single-span bridge might not come out of a cost-benefit analysis as the most favorable design.

A bridge deck may be designed to have a more streamlined cross-section. Drag coefficients for a streamlined deck are indeed much lower than for a deck similar in shape to the bridge over the Yabechi River (6). Such a shape has potential for rivers where the superstructure is submerged during a flood, but the debris load is low. Once debris starts accumulating against the deck, the advantage of the reduced drag coefficient is lost.

On the resistance side, the connection between the pier and the deck can be improved. The most effective measure will be a monolithic connection, however this is not a good solution for structures in seismically active areas such as Japan. Instead of a monolithic connection a fixed bearing with high resistance may be used. Alternatively, so-called "unseating prevention devices" (UPD's) can post-installed on bridges whose bearings don't implicitly restrict translational movement. A UPD is a concrete or steel structure mounted to the pier in between the girders of the deck. When the deck moves laterally, it collides with the UPD and further movement is restricted.

A brute force solution against pier failure is to make the embedded depth of the piers larger. This makes the pier heavier and harder to overturn. Increasing the length of the pier also improves the stability of the pier against overturning, as it adds weight and increases the lever arm between the center of gravity and point of rotation. Increasing the width of the pier will not have much effect, as total drag force increases proportionally with width as well. Alternatively, the pier might be anchored to the ground with tension anchors to increase the resistance against overturning.

Debris racks similar to those that are used in front of inlets for water pumping stations could be placed in strategic places along the river. Debris will accumulate against these structures which are purpose-built to resist the high drag forces caused by the debris. Such an implementation unfortunately severely hampers the navigability of the river.

8 CONCLUSIONS

Differences between predictions of forces in chapter 3 and the results of measurements in chapter 5 exist. Based on past research and current design codes, it was estimated that in case of bridge failure, that could've only happened if the pier and decks were connected and fail as a whole, as the pier would never fail on its own according to the estimates. However, the most important conclusion from the experiments is that this hypothesis (simultaneous failure of pier and decks) needs to be discarded. The scale model of the bridge that had the decks and pier connected did not collapse under any of the hydraulic conditions, including the most extreme case where a lot of debris was lodged against the bridge. Instead, the bridge deck must have failed first, subsequently followed by the bridge pier.

Contrary to what one might intuitively expect, the resistance to lateral movement of the bridge deck increases as Froude number (flow velocity) increases, despite of increased drag force. This can be attributed to the downward lift force also increasing as flow velocity increases, and leads to the unusual result that the bridge decks are more stable at high flow velocities than at lower flow velocities, provided that the submergence of the deck is not too high. Displacement of the scale model bridge deck – without simulated debris lodged against it – was indeed observed under a few high velocity and high submergence conditions. However, when simulated debris accumulations were lodged against the scale model bridge deck, the increased drag and buoyancy associated with debris moved the range of conditions at which deck failure would occur to a much milder regime. These conditions would be more likely to actually be present in the river and would have occurred earlier in time than the conditions at which a deck without debris would've been pushed of its piers.

The bridge pier is a structure that is supposed to receive its stability from its weight. The streamlined shape of the nose of the pier reduced hydrodynamic drag sufficiently to maintain stability across all flow conditions. Therefore it must be concluded that debris accumulation against the pier played a critical role in the collapse. During the experiments it was verified that a properly scaled down version of the pier indeed did not collapse under any of the experimental conditions when no debris was present. Introduction of large debris shapes trapped around and against the nose of the pier, transferring buoyancy forces and moments, was necessary to observe the pier toppling over. A large enough frontal area and sufficient submergence were found to be the most important failure criteria, while Froude number did not have a pronounced effect.

The research emphasizes that the increased forces and moments on bridges associated with debris accumulations shall not be underestimated. Especially bridges that are founded on spread footings or other shallow foundations are vulnerable. Retrofitting existing bridges with bearings that can resist large horizontal forces, preventing disconnection of the deck from the pier, will ensure than sufficient weight is counteracting the overturning moments by drag forces.

Assuming that results of the experiments can be carried over to field scale using the dimensionless numbers h^* and Fr and based on all other assumptions made in this thesis, total collapse of the bridge – including the piers – is only to be expected in a narrow region of flow conditions. Figure 104 shows what type of failure can be expected at specific flow conditions for the bridge geometry similar to that in this research.

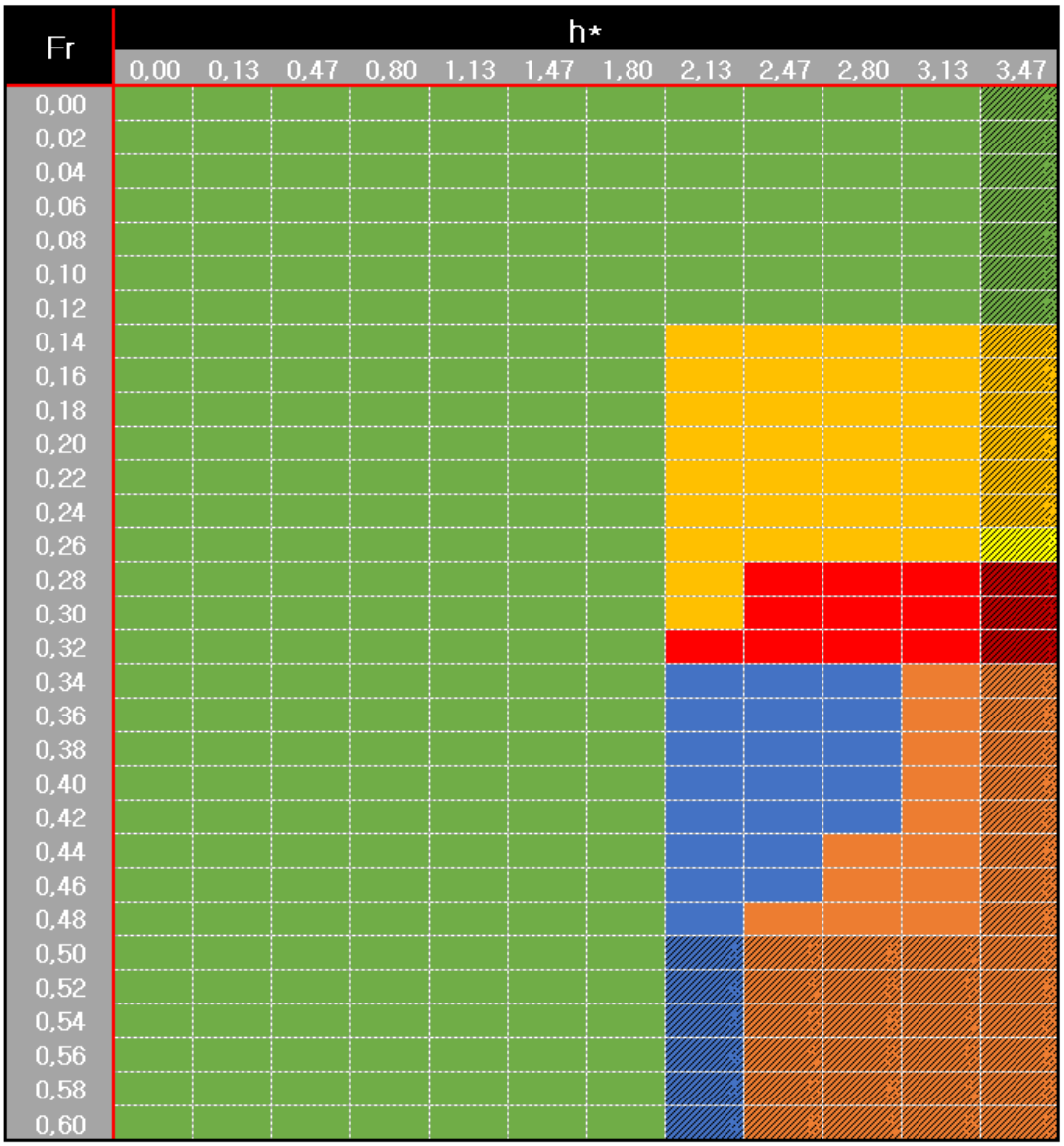

LEGEND

No failure of the bridge is expected.

If debris has accumulated, failure of the bridge deck is to be expected.

Failure of the bridge deck is to be expected, regardless of the presence of debris accumulations.

No failure of the bridge is to be expected. However, if debris has accumulated against a standalone pier, failure of the pier is to be expeced.

Failure of the bridge deck is to be expected, as long as no debris has accumulated. However, if debris has accumulated against a standalone pier, failure of the pier is to be expected.

If debris has accumulated, failure of the entire bridge is to be expected.

If debris has accumulated, failure of the entire bridge is to be expected. The bridge deck is expected to fail without debris accumulation as well.

//////// Expectation extrapolated from experiments.

Figure 104: Expectations about collapse of the bridge under varying flow conditions

9 RECOMMENDATIONS FOR FUTURE RESEARCH

During the experiments several issues surfaced that could've had a negative impact on the results. An improved experimental method would alleviate the inaccuracies and/or increase the reliability. A few suggestions are given:

- There is room for improvement of the technique used to attach and interchange simulated debris to the bridge components. In the current research, some improvised methods involving fishing wire were used, but this proved to be unreliable at times.
- Streamlining the scale model abutment will cause the backwater effect to be smaller and reproduce the flow pattern in the vicinity of the bridge more accurately.
- Automated flow depth measurement using for example a laser emitting/receiving device reflecting on a surface floating on the water will allow for more accurate and continuous flow depth measurement.
- Stiffening the rig used to hold the load cells as well as the connector between the load cell and the component will help to reduce vibrations due to vortex-shedding.

No distinction between lift and buoyancy forces was made in this research, as measuring the exact volume of a component that is partly submerged proved difficult. In case the distinction can be made, a better understanding of the behavior of the lift coefficient as a function of flow characteristics and object geometry can be obtained.

Although much is known about hydrodynamic forces on bridge piers and bridge decks separately, when these components are placed in close proximity to each other the situation changes. This research proved that one may not simply add up forces on two decks and one pier to make a statement about forces on the system. More research on this topic is suggested. Additionally, the influence of nearby boundaries such as riverbanks or structures such as abutment can be investigated further.

A type of debris accumulation that was not investigated but may very well occur depending on the length of the longest logs in the river, is an accumulation crossing the gap between the two piers. Such an accumulation may develop if a log with a length longer than the gap between the piers gets stuck on the front noses of both piers. Smaller logs can then build up from this initial blockage.

Numerical simulations are a great tool to predict the full-scale behavior of the bridge. A numerical CFD model validated by the experimental results can be used to upscale the results of the experiments to field scale.

Lastly, experiments were only conducted at a limited combination of flow conditions and bridge geometry, due to a limited amount of time available in the Fluid Mechanics laboratory. Simply performing more experiments, i.e. gathering more data points, will allow for an even better understanding of the forces on (partially) inundated bridge piers and superstructures.

REFERENCES

1. *Hydrodynamic Loading on River Bridges.* **Malavasi, Stefano and Guadagnini, Alberto.** 2003, Journal of Hydraulic Engineering, pp. 854-861.

2. **Jempson, Mark A.** *Flood and Debris Loads on Bridges.* University of Queensland. 2000.

3. *CFD Analysis of Bridge Deck Failure due to Tsunami.* **Bricker, Jeremy D., Kawashima, Kazuhiko and Nakayama, Akihiko.** 2012.

4. *Contribution of Trapped Air, Deck Superelevation, and Nearby Structures to Bridge Deck Failure during a Tsunami.* **Bricker, Jeremy D. and Nakayama, Akihiko.** 2014, Journal of Hydraulic Engineering.

5. *Damage Analysis of Bridges Affected by the Tsunami in the Great East Japan Earthquake.* **Kosa, Kenji.** 2014, Journal of JSCE, pp. 77-93.

6. **Kerenyi, K., Sofu, T. and Guo, J.** *Hydrodynamic Forces on Inundated Bridge Decks.* 2009. FHWA-HRT-09-028.

7. **Australian Standards.** *AS5100 - Bridge Design Part 1: Scope and General Principles.* 2004.

8. **Parola, Arthur C.** *Debris Forces on Highway Bridges.* National Cooperative Highway Research Program. Washington, D.C. : National Academy Press, 2000.

9. *A Flood Loading Methodology for Bridges.* **Wellwood, N. and Fenwick, J.** 1989. 15th ARRB Conference. pp. 315-341.

10. **Stanton, J. F. and Roeder, C. W.** *Elastomeric Bearings Design, Construction and Materials.* National Cooperative Highway Research Program. 1982.

11. **Roeder, C. W., Stanton, J. F. and Taylor, A. W.** *Performance of Elastomeric Bearings.* National Cooperative Highway Research Program. 1987.

12. **Kaczinski, Mark.** *Steel Bridge Design Handbook: Bearing Design.* Federal Highway Administration. 2012.

13. **State of Wisconsin Department of Transportation.** Bridge Design Manual. [Online] 2017. [Cited: May 14, 2018.] http://wisconsindot.gov/dtsdManuals/strct/manuals/bridge/ch27.pdf.

14. **Veen, van der, Cor.** *Bearings - PowerPoint Presentation.* April 25, 2018.

15. **Cosmec Inc.** Elastomeric Bearings. *Cosmec Structural Bearings for Bridges and Buildings.* [Online] [Cited: May 17, 2018.] http://www.cosmecinc.com/Elastomeric%20Bearings.

16. **Lee, D. J.** *Bridge Bearings and Expansion Joints.* 2nd. London : E & FN SPON, 1994.

17. **Trelleborg Engineered Products.** Elastomeric Bearing Pads & Strips. [Online] [Cited: May 18, 2018.] https://www.trelleborg.com/engineered-products/~/media/engineered--.

18. *Shear Strength of Stud Connectors in Lightweight and Normal-Weight Concrete.* **Ollgaard, J. G., Slutter, R. G. and Fisher, J. W.** April 1971, AISC Engineering Journal, Vol. 8, pp. 55-64.

19. **American Concrete Institute.** *Building Code Requirements for Structural Concrete.* 2014. ACI 318-14.

20. *Pryout capacity of Cast-In Headed Stud Anchors.* **Anderson, Neal S. and Meinheit, Donald F.** March-April 2005, PCI Journal, pp. 90-112.

21. *Concrete Capacity Design (CCD) Approach for Fastening to Concrete.* **Fuchs, W., Eligehausen, R. and Breen, J.** Jan-Feb 1995, ACI Structural Journal, pp. 73-93.

22. **MAURER SÖHNE.** Bridge Bearings. *MAURER UK.* [Online] [Cited: June 2, 2018.] http://www.maurer.co.uk/downloads/MAURER_Elastomeric_Bearings.pdf.

23. **American Association of State Highway and Transportation Officials.** *AASHTO LRFD Bridge Design Specifications.* Washington, D.C. : s.n., 2013.

24. **Hoerner, S. F.** *Fluid-Dynamic Drag.* s.l. : Hoerner, S.F., 1965.

25. **Battjes, J. A.** *CT2100 - Vloeistofmechanica Lecture Notes.* Delft : s.n., 2002.

26. **Delany, Noel K. and Sorenson, Norman E.** *Low-Speed Drag of Cylinders of Various Shapes.* National Advisory Committee for Aeronautics. 1953.

APPENDIX A

Dimensions of the scale model

Design drawings for the bridge were provided by Japanese authorities.

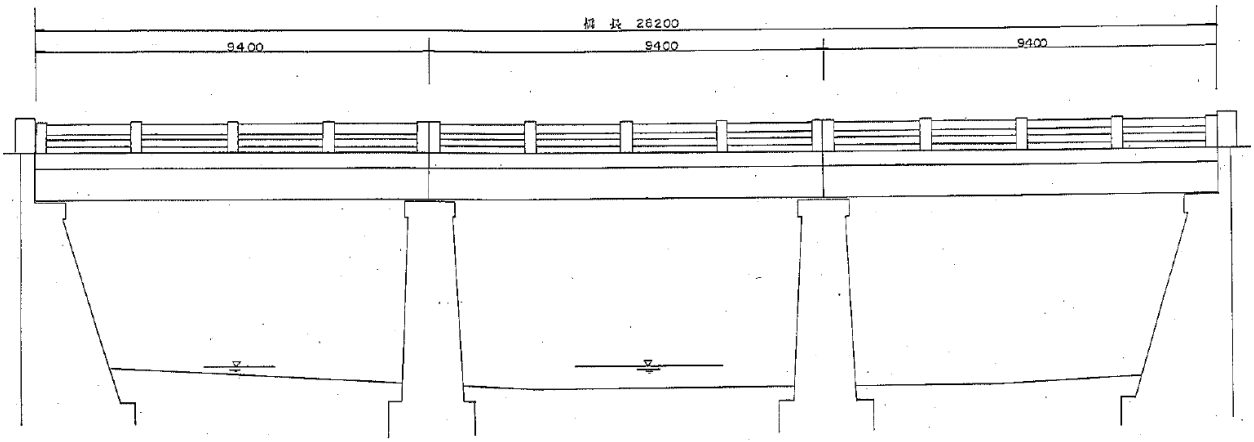

Figure 105: design drawing (side view) of the bridge under investigation.

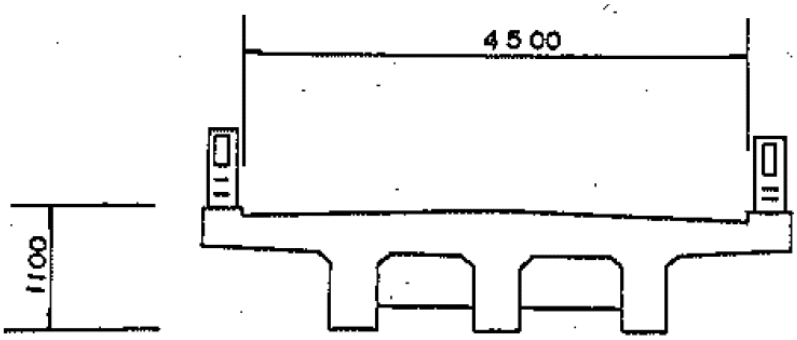

Figure 106: cross section of the bridge deck

Also, photos of the bridge before its collapse are available.

Figure 107: photo of the bridge before its collapse.

Figure 108: photo of the bridge before its collapse.

Based on Figure 105 and Figure 106, and also using the photos (Figure 107 and Figure 108), the following table of dimensions was constructed:

		Real bridge [mm]	**1:37 scale model [mm]**
Given dimensions			
Length of a single deck segment	L_{01}	9400	254
Width of the road	L_{02}	4500	122
Height of a deck segment (excl. railings)	L_{03}	1100	30
Estimated dimensions (deck)			
Width of the full deck	L_{04}	5273	143
Width of the deck sides	L_{05}	387	10
Height of a girder	L_{06}	695	19
Width of a girder	L_{07}	436	12

Distance between girders	L_{08}	843	23
Distance between girder and deck edge	L_{09}	1125	30
Height of the railing	L_{10}	700	19
Estimated dimensions (pier)			
Width of the foundation	L_{11}	2258	61
Height of the foundation	L_{12}	802	22
Minimum width of the base of the pier	L_{13}	1052	28
Maximum width of the base of the pier	L_{14}	1515	41
Height of the base of the pier	L_{15}	4362	118
Width of the top of the pier *(based on photos)*	L_{16}	1813	49
Height of the top of the pier	L_{17}	390	11
Average length of the pier	L_{18}	4500	122
Length of foundation *(based on photos)*	L_{19}	5440	147

APPENDIX B

Required weights of the scale model

The target weight for the scale bridge deck model was calculated using a 3D modelling application to be 1216 g.

The mass of the dry plastic scale model was measured at 384 g.
The total volume of voids in the model was measured to be 120 cm^3.
The density of lead is taken as 11,3 g/cm^3. The density of a type of wet sand used was measured as 1.95 g/cm^3.
In order to completely fill the voids with a mixture of lead and sand, 64 cm^3 of lead weighing 723 g and 56 cm^3 of wet sand weighing 109 g was used.
384 + 723 + 109 = 1216 g.

The target weight for the scale bridge pier model was calculated to be 1682 g by the 3D modelling application.

Mass of the dry plastic/wood scale model: 464 g.
Total volume of voids in the model: 219 cm^3.
To fill the voids, 84,5 cm^3 of lead weighing 955 g and 134,5 cm^3 of wet sand weighing 263 g were used.
955 + 464 + 263 = 1682 g.